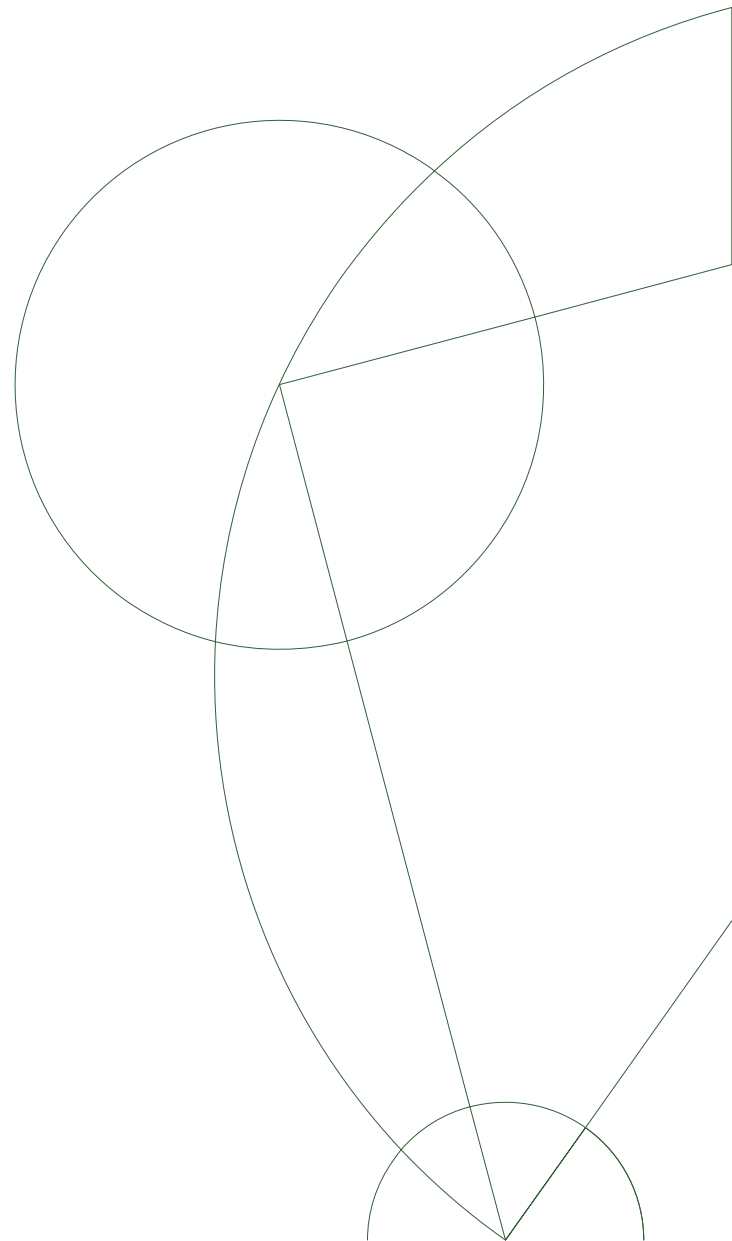




Master's Thesis

Emil Bols

Proton-Proton Central Exclusive Pion Production at $\sqrt{s} = 13$ TeV with the ALFA and ATLAS Detector



Supervisor: Peter Hansen

September 4, 2017

Abstract

The cross section for proton-proton central exclusive dipion production, $pp \rightarrow p + \pi^+ \pi^- + p$, has been measured at the center of mass energy $\sqrt{s} = 13\text{TeV}$, where double Pomeron exchange is expected to dominate. The LHC was used to create the central diffractive events, and all the final state particles were measured using the ATLAS and ALFA detector.

After correcting for detector inefficiencies and proton acceptance using the Donnachie-Landshoff model with $\alpha' = 0.126\text{GeV}^{-2}$ and $\epsilon = 0.085$, the cross section was found to be:

$$\sigma_{pp \rightarrow p + \pi^+ \pi^- + p} = 18.754 \pm 0.048(\text{stat.}) \pm 0.770(\text{syst.})\mu\text{b}, \quad |\eta_\pi| < 2.5, \quad p_{t,\pi} > 100\text{MeV} \quad (1)$$

The invariant mass spectrum of the pions has been analyzed in order to extract the widths and masses of the $f_0(500)$, $f_0(980)$, $f_2(1275)$ and $f_0(1500)$ mesons. A correlation between the two outgoing protons has been observed, which is not in agreement with Pomeron exchange models, where the exchange vertices are assumed to be uncorrelated. Different central diffractive models have been compared to data, and it appears that a Pomeron trajectory with low α' and ϵ is favored.

The cross section for proton-proton central exclusive four pion production, has also been measured at the energy $\sqrt{s} = 13\text{TeV}$.

$$\sigma_{pp \rightarrow p + \pi^+ \pi^- \pi^+ \pi^- + p} = 3.575 \pm 0.065(\text{stat.}) \pm 0.338(\text{syst.})\mu\text{b}, \quad |\eta_\pi| < 2.5, \quad p_{t,\pi} > 100\text{MeV} \quad (2)$$

The mesons $f_1(1285)$ and $f_0(1500)$ are observed in the four pion invariant mass spectrum.

Acknowledgements

Dr. Simon Stark previous work and expertise on ALFA, has saved me a lot of time and hard work. Our many discussion have been extremely valuable. The work of Alexander Lind was very useful for this analysis, and a big thanks to him for sharing his simulation framework.

Thanks to Dr. Benedetto Giacobbe for his help with determining the luminosity of the runs, and to Dr. Sune Jakobsen for the great data. Thanks to Dr. Alejandro Alonso for sharing the Inner Detector efficiency values.

Thanks to Jack Rolph for our many discussions about ALFA and black holes, and for sharing his amazing homebrewed beers. Thanks to the entire NBI HEP group for creating a great atmosphere.

A big thanks to my supervisor Professor Peter Hansen for enabling me to have a very fun project, and for always being willing to share his many great ideas, while discussing the analysis problems. Thanks to Dr. Jørgen Beck Hansen for his many insights about the analysis.

Finally, thanks to both Pernille and Jack for helping me proofread the thesis.

Contents

Abstract	2
Acknowledgements	3
Introduction	7
The Standard Model	9
The Elementary Particles	9
Quantum Chromodynamics	10
The Running Coupling Constant	10
Diffraction and Regge Theory	13
Regge Trajectory	13
Diffraction	16
The Scalar and Tensor Mesons below 2 GeV	17
Resonance Fitting	19
Large Hadron Collider	21
Overview	21
Beam Physics	21
Luminosity	22
Emittance and Beam Optics	23
The ATLAS Detector	24
Inner Detector	24
Pixel Detector	26
SCT detector	26
TRT detector	26
Trigger System	26
MBTS	26
The ALFA Detector	28
Overview	28
Main Detector	28
Track Reconstruction	28
Overlap Detectors	29
Roman Pots	29
Trigger System	31

Data Analysis	33
Run Information	33
Event Selection	33
Alignment	35
Event Reconstruction	37
Momentum Reconstructions	37
Momentum Resolution of the Full System	40
Background Analysis	42
Choice of Signal Region	47
Systematic Uncertainty from Background Subtraction	48
Mass Spectrum Background	49
Background from Wrong PID of Kaons	50
Back to Back Cut	51
Partial Wave Analysis	51
Reconstructing the Pomeron Kinematics	51
Extraction of Spin Density Matrix Elements	52
Four Pion Analysis	55
Background Analysis	55
Acceptance and Efficiencies	57
ALFA Acceptance	57
Beam Spot and Beam Divergence	58
Model Dependence	58
Mass Dependence	60
t-Spectrum	60
L1 Trigger Efficiencies	60
HLT Efficiency	63
Loss from L1 Veto	64
Loss from Pile-up	65
ALFA Track Reconstruction Efficiency	66
Probability Theory for Track Reconstruction Efficiency	66
Systematic Uncertainty on Track Efficiency	67
Ghost Tracks and Track Matching	68
Uncertainty from the ALFA Four Track Veto	69
ATLAS Inner Detector Efficiency	70
Uncertainty from the Inner Detector Track Efficiency - $\pi\pi$	71
Uncertainty from the Inner Detector Track Efficiency - $\pi\pi\pi\pi$	71
Inner Detector Vertex Reconstruction	72
Uncertainty from the Vertex Efficiency	73
Results	75
Central Exclusive $\pi\pi$ Production Cross Section	75
Central Exclusive $\pi\pi$ Production Mass Spectrum	76
Reggeon Mass and Widths	77
Outgoing Transverse Proton Momentum and the Mass Spectrum	78
t-Spectrum	78
Energy Spectrum	81
Extraction of α'	81
Central Exclusive $\pi\pi\pi\pi$ Production Cross Section	83
Central Exclusive $\pi\pi\pi\pi$ Production Mass Spectrum	83
Dalitz Plot	84

Discussion	85
Comparison with ISR	85
Comparison with WA91	85
Comparison with CMS and ALICE	88
Comparison with LEP Data	88
Outlook	89
Conclusion	90
Bibliography	91
List of Figures	94
List of Tables	98
Appendix	100

Introduction

The ambitious goal of Particle Physics is to figure out what the smallest constituents of Nature are, and how they interact. Today several known particles are believed to be elementary, and their dynamics are described through four fundamental forces of nature. These are the strong force, gravity, the weak force and the electromagnetic force. One of the core principles of particle physics has always been reductionism, which is the idea that physical phenomenon can be explained by decomposing the problem into smaller constituents. However it seems that the more you learn about the fundamental laws of particle physics, the further they seem from anything observed in the "real" world. When going to a new distance scale, all the well understood theories become completely different, and they have to be remodeled from scratch. The strong force is a perfect example of this.

The strong force is all around us. It keeps the protons together and govern the nucleon-nucleon interaction. It is extremely well understood at high energies, where it is modeled in terms of quarks and gluons, and the dynamics of the force can be predicted with great precision. However, when examining lower energies it becomes extremely difficult to predict anything, even when using the knowledge of the higher energy dynamics. Particle diffraction at high energies is a great area to study the border between these two scales. Here the strong force is modeled using Pomerons. In the high energy limit, the internal structure of the object can be understood as a two gluon system, but it appears to be much more complex at low energies.

At the LHC, protons are collided at an enormous center of mass energy. At first sight, it seems strange to examine the strong force at low energies by colliding protons at high energies. However it turns out that at high energies the protons have a chance of emitting a low energy Pomeron. If both protons emit a Pomeron these can then fuse in the process $\mathbb{P}\mathbb{P} \rightarrow X$, where X is some particle system. While the protons are extremely high energy, these Pomerons will generally only have an energy of around 0.5GeV. In essence a 13TeV proton collider can be used as a 1GeV Pomeron collider. This allows for a detailed study of the Pomeron.

Since the Pomeron is expected to be a pure gluon state, it should couple strongly to glueball states, which are bound state particles consisting only of valance gluons. These are predicted by QCD, but have never been experimentally confirmed. The channel $\mathbb{P}\mathbb{P} \rightarrow \pi\pi$ is particularly interesting to investigate, since several exotic mesons, which are expected to be produced by Pomeron Fusion, will decay to two pions. They are therefore visible as resonances in the invariant mass spectrum of pions produced by Double Pomeron Exchange.

The main goal of this thesis is to measure the cross section of the central exclusive process $pp \rightarrow p + \pi^+ \pi^- + p$ at $\sqrt{s} = 13\text{TeV}$. Here two protons "glance" each other and diffractively excites the vacuum to produce two pions, while both remaining intact. A precise measure-

ment of the cross section can be used to help determine the Pomeron-proton coupling along with the Pomeron-Pomeron coupling. It can also be used to determine, how the central diffractive cross section increases with the center of mass energy, which is deeply connected to the Pomeron properties. From the differential cross section as a function of the central system invariant mass, the coupling strength of the Pomeron to different exotic mesons states can be extracted. This can potentially be used to determine the internal structure of the mesons and the Pomeron.

Central exclusive pion production has a distinct experimental signature, consisting of two forward scattered protons along with centrally produced pions. There will be a large rapidity gap between the central product and the protons. This process can be measured at the LHC using the ATLAS detector to detect the central product, while using the forward detector ALFA to measure the scattered protons.

In the first chapter the theoretical concepts necessary to understand the content of the thesis are explained. The Standard Model of particle physics is briefly introduced, and the theory of particle diffraction is discussed. Following this the experimental apparatus consisting of the LHC, the ATLAS detector and the ALFA detector is described. The analysis procedure used to obtain the cross section is then explained in detail. The main focus of this section is the different techniques that have been developed to separate signal and background. The next chapter describes the determination of several different detector efficiencies, and the calculation of the geometrical acceptance. This chapter is tightly linked with the analysis section, since several of the methods used to calculate the detector efficiencies are data driven. Finally the obtained results are presented, and these are discussed and compared to previous measurements. Some ideas for future studies are shared.

The Standard Model

The Standard Model[6] summarizes all phenomenology known to this date concerning elementary particles. It describes the Strong Force, the Weak Force and the Electromagnetic Force. Gravity is not included at present. The main idea is to introduce a list of free parameters, which are fixed by experiment. In the Standard Model there are altogether 19 free parameters. The majority of these parameters are particle masses and couplings.

The Elementary Particles

The definition of an elementary particle is that it is not comprised of constituents. Which particles are fundamental is found purely from experiment. This is done by probing the particles at the smallest scales, which requires high energies. The particles that are considered fundamental today, are the ones that do not break apart at the energy frontier.

The elementary particles are classified into two separate categories based on, whether they have half-integer or integer spin, as this determines if they are fermions, which obey Fermi Statistics, or bosons, which obey Bose Statistics. The 17 known elementary particles can be seen on Figure 1. The first six are the leptons, which come in three pairs and are half integer spin. They consists of the electron and the electron neutrino (e^- , ν_e), the muon and the muon neutrino (μ^- , ν_μ), and the tau and the tau neutrino (τ^- , ν_τ). Next are the four vector bosons with spin 1. They consists of the three massive vector bosons, the W^+ , W^- and the Z^0 , and then the massless vector boson, the photon γ . There also exists a scalar boson, the Higgs Boson, which has spin 0. This particle is responsible for generating the masses of the Z - and W -bosons, as well as the charged fermions.

The final set of fundamental particles are the quarks and the gluon. These are however not seen freely in experiment, instead the composite particles, the hadrons, are observed. They have a finite size of around 1fm. They consist of two particle classes. The mesons which are integer spin, and the baryons which are half-integer spin.

Within the Standard Model the dynamics of the particles are described by three different forces. Each force is associated with the requirement of local gauge invariance under a certain symmetry group. The Standard Model dynamics is described via the requirement of local gauge invariance under the symmetry group:

$$SU(3)_C \otimes SU(2)_L \otimes U(1)_Y \tag{3}$$

Each of these different symmetry groups represents a fundamental force, which have associated gauge bosons that mediate the interaction.

The $SU(2)_L \otimes U(1)_Y$ group is the symmetry representing the electroweak interaction. It consists of the hyper charge group $U(1)_Y$ and the weak isospin group $SU(2)_L$, which only

acts on left-handed fermions. Beneath the electroweak scale of around 246GeV, the symmetry is spontaneously broken, leaving $U(1)_{\text{em}}$ behind. The gauge boson associated with this group, is the massless photon. This particle interacts with particles which have electric charge, and it couples to these particles with a coupling strength of $\alpha_{\text{em}} \approx \frac{1}{137}$. The three other gauge bosons, the W^+ , W^- and the Z^0 , acquire mass from this symmetry breaking.

The $SU(3)$ group represents the strong interaction, and the associated charge is called colour charge. The theory of the strong force is named Quantum Chromodynamics. The gauge boson, which mediates the interaction is the spin 1 gluon. It carries color charge itself. The coupling strength of the strong force is much higher than the other forces, and this means that the self interaction of the gluons become very important. The only other particles which have colour charge are the quarks.

Quantum Chromodynamics

There exists six different quarks, which comes in three flavor doublets. The up and down quark (u, d), the strange and charm quark (c, s), and the bottom and top quark (t, b). The u, c and t quarks have fractional charge of $+\frac{2}{3}$, whereas the d, s and b have fractional charge of $-\frac{1}{3}$. Like, the leptons, the quarks are spin 1/2. They also carry colour charge, which comes in three colors. The gauge boson, the gluon, is massless, and it carries a combination of colour and anti-colour charge. There exists 8 different color combinations, which then equates to 8 gluons. The gluons interact with themselves, unlike the QED mediator, the photon. By putting the quarks together in pairs of three Baryons are obtained, which then have integral charge and half-integer spin. The baryon must have net neutral color charge.

The meson states are then composed of a quark and an anti-quark, carrying color and the corresponding anti-color, thus giving a net neutral color charge. These are then integer spin. In general the only rules for hadrons is a net color charge of zero. There is nothing in the QCD framework that prevents hadrons like tetraquarks with two quarks and two anti-quarks, and pentaquarks with 4 quarks and 1 anti-quark. The gluons themselves carry color charge, and they should be able to create a bound state with neutral colour charge, called a glueball.

The Running Coupling Constant

The three forces have different interaction strengths, which are given by their coupling constants. The Standard Model is described in the framework of Quantum Field Theory, and the main method for doing calculations is by using perturbation theory, and do a series expansion in the coupling constant. Both the weak and electromagnetic force have a weak coupling strength ($\alpha \ll 1$), meaning that a series expansion converges. The electromagnetic coupling grows in strength as the momentum transfer increases, however even at extremely high energies the coupling is weak ($\alpha \ll 1$), as can be seen on Figure 2. This phenomenon occurs because the vacuum screens the charges. Surrounding an electric charge are virtual electrons and positrons. At low energies, where the distance scale of the interaction is large, the vacuum polarization will partially cancel the charge. As the energy increase and the distance scale becomes smaller, the screening becomes less efficient, and the charge increases.

The strong force, however, behaves differently. While virtual quarks also screen the color charge in the same manner as virtual electrons screen the QED charge, virtual gluons instead amplify the color charge, since they both carry color and anti-color. At low energies

Standard Model of Elementary Particles

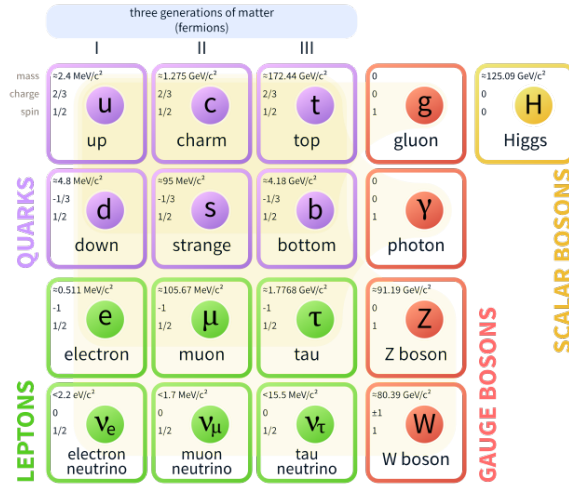


Figure 1: The seventeen elementary particles, which have been experimentally observed. It is expected that we have an eighteenth particle named the graviton which is the propagator of the gravitational force.

the strength of the coupling increase significantly making α_s of order unity. This means that perturbative calculations are impossible. The rapid growth in the coupling strength also means that color charges cannot be isolated. This is referred to as color confinement, and the rule, that net color charge is zero for hadrons, arises from this. The strength of the coupling then decreases as we increase energy. This makes it possible to do perturbative calculations at high energies.

In high energy pp collisions, where perturbative QCD is possible, the colliding hadrons still need to be modeled. It is not possible to calculate the distribution of quarks and gluons in the hadron with perturbation theory. The solution is to use what is called the factorization theorem. This says that the cross section of two hadrons colliding, can be factorized into a non-perturbative part and a perturbative part. The non-perturbative part is the Parton Distribution Function (PDF) of the hadron, which is found by fitting to experimental data. If the distribution is experimentally known at some momentum transfer scale, then the distribution at a higher scale can be extrapolated using perturbation theory. This PDF can then be used to model the hadron, and a perturbative calculation of the constituent parton interactions can be done at high energies.

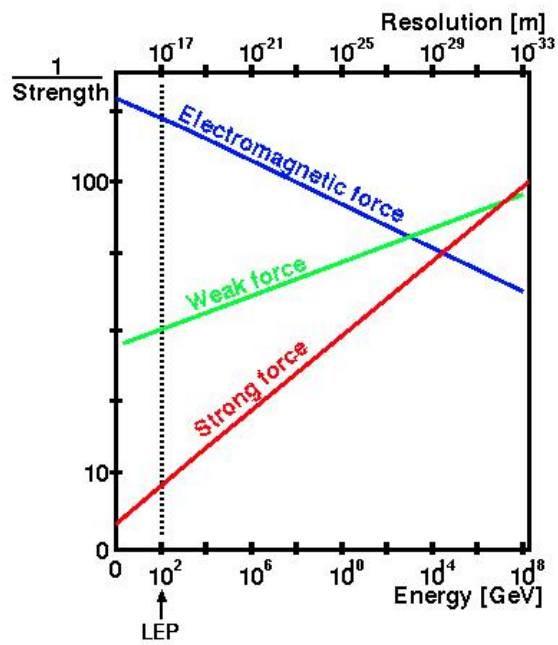


Figure 2: The strength of the coupling constant changes for the different forces as we change the energy.[44]

Diffraction and Regge Theory

In diffraction, the energy transfer is generally of the order of a GeV, making the interaction non-perturbative. Therefore a model other than pQCD needs to be used. The classical description of high energy diffraction is in terms of Regge theory. Regge theory has a long history and it even predates QCD. The theory does not care about the underlying dynamics of the interaction, and it uses the most basic assumptions about the scattering process in order to make predictions.

Regge Trajectory

A detailed and completely rigorous derivation can be found in reference [23]. Here the main concepts have been outlined, while sacrificing a bit of the rigor to simplify the expressions. The first step in Regge Theory is to describe the interaction with the S-matrix S_{ab} , where a is the initial state and b is the final state. The S-matrix is related to the scattering T_{ab} matrix by $S_{ab} = 1 + iT_{ab}$. The T-matrix can be written as a function of the Mandelstam variables s, t and u . In a interaction with two initial state particles and two final state particles, $a + b \rightarrow c + d$, they would be:

$$s = (p_a + p_b)^2, \quad t = (p_a - p_c)^2 \quad u = (p_a - p_d)^2 \quad (4)$$

The first assumption of Regge theory is that the S-matrix is unitary:

$$SS^\dagger = (1 + iT)(1 + iT)^\dagger = 1 \Rightarrow T^\dagger T = (T - T^\dagger)/i = 2\text{Im}(T) \quad (5)$$

The second assumption is that the T-matrix is an analytical function in terms of the Mandelstam variables and the angular momentum. The T-matrix can be expanded in terms of its partial waves:

$$T(s, t) = \sum_{l=0}^{\infty} (2l + 1) a_l(s) P_l(\cos(\theta)) = \sum_{l=0}^{\infty} (2l + 1) a_l(s) P_l(z_s) \quad (6)$$

Here $a_l(s)$ are the amplitudes of the partial waves and $z_s = 1 + \frac{2t}{s-4m^2}$. From the condition of analyticity of the T-matrix, follows crossing symmetry, which means that the s-channel amplitude $T(a + b \rightarrow c + d)$ is equivalent to the t-channel amplitude $T(a + \bar{c} \rightarrow \bar{b} + d)$. Using this, the amplitude can be extended to the t-channel:

$$T(s, t) = \sum_{l=0}^{\infty} (2l + 1) a_l(t) P_l(z_t) \quad (7)$$

The next step is to do an analytical continuation in terms of the angular momentum l , allowing it to take complex continuous values rather than the usual discrete ones. Instead

of summing over the angular momentum, it is rewritten in terms of a contour integral using the Sommerfeld-Watson transformation. The expression then becomes:

$$T(s, t) = i \oint dl(2l + 1)a(l, t) \frac{P(l, z_t)}{\sin(\pi l)} \quad (8)$$

Here the $\frac{1}{\sin(\pi l)}$ term introduces poles at the real integer values of l , which means that a contour chosen around the real axis, will recover the summed expression after carrying out the integral, since the residue of these poles, gives the terms in the sum. The next step is to deform the contour to run parallel with the imaginary axis. Any new poles in the complex plane that are picked up when doing this, are added to the expression. This gives:

$$T(s, t) = - \sum_n \frac{(2\alpha_n(t) + 1)\beta_n(t)}{\sin(\pi\alpha_n(t))} P(\alpha_n(t), z_t) + i \int_{-\frac{1}{2}-i\infty}^{-\frac{1}{2}+i\infty} dl(2l + 1)a(l, t) \frac{P(l, z_t)}{\sin(\pi l)} \quad (9)$$

α_n is the location of pole n and β_n refers to the residue. In the high energy diffraction limit, where $s \gg |t|$ and $s \rightarrow \infty$, the Legendre polynomials reduce to:

$$P(\alpha(t), z_t) \propto s^{\alpha(t)} \quad (10)$$

This means that the contribution from the complex integral vanishes, since the real part of the contour was chosen to lie on $-\frac{1}{2}$. It also means that the only pole which makes a significant contribution is the one with the largest real part. The amplitude expression then becomes:

$$T(s, t) \propto (1 + e^{-i\pi\alpha(t)})\beta(t)s^{\alpha(t)} \quad (11)$$

This means that the diffractive interaction can be described as an exchange of an object with angular momentum $\alpha(t)$. This object does not have half or full integer angular momentum, but it is rather a sum over all of the possibilities. This exchange object is referred to as a reggeon.

It turns out that different trajectories describing $\alpha(t)$ exists. These are found from experiment. When $\alpha(t)$ is a real integer value, it corresponds to a pole, which is a physical resonance, for instance a meson. On Figure 3 a plot of the squared mass against the angular momentum J of different mesons are shown. It is seen that they lie on a straight trajectory, which means that $\alpha(t) = \alpha' \cdot t + \alpha(0)$. Different families of mesons exists, and they are each connected to a trajectory. Regge theory now states that this family of mesons can be used as exchange objects in the diffractive interaction, and their contribution to the cross section will be given by their trajectory:

$$\frac{d\sigma}{dt} = \frac{|T(s, t)|^2}{s^2} \propto s^{2\alpha't + 2\alpha(0) - 2} \quad (12)$$

The Pomeron

With the Optical Theorem[30], the contribution to the total cross section of different reggeons can be calculated:

$$\sigma_{\text{tot}} = \frac{\text{Im}(T(s, t=0))}{\sqrt{\lambda(s, m_1^2, m_2^2)}} \xrightarrow{m_1^2, m_2^2 \ll s} \frac{\text{Im}(T(s, t=0))}{s} \propto s^{\alpha(0)-1} \quad (13)$$

The Regge trajectories are fitted to resonances, and the one with the largest slope have $\alpha(0) = 0.5$ [35]. This leads to $\sigma_{\text{tot}} \propto s^{-0.5}$, and it is therefore predicted that the total cross section will fall as the center of mass energy is increased. Experimental measurements show

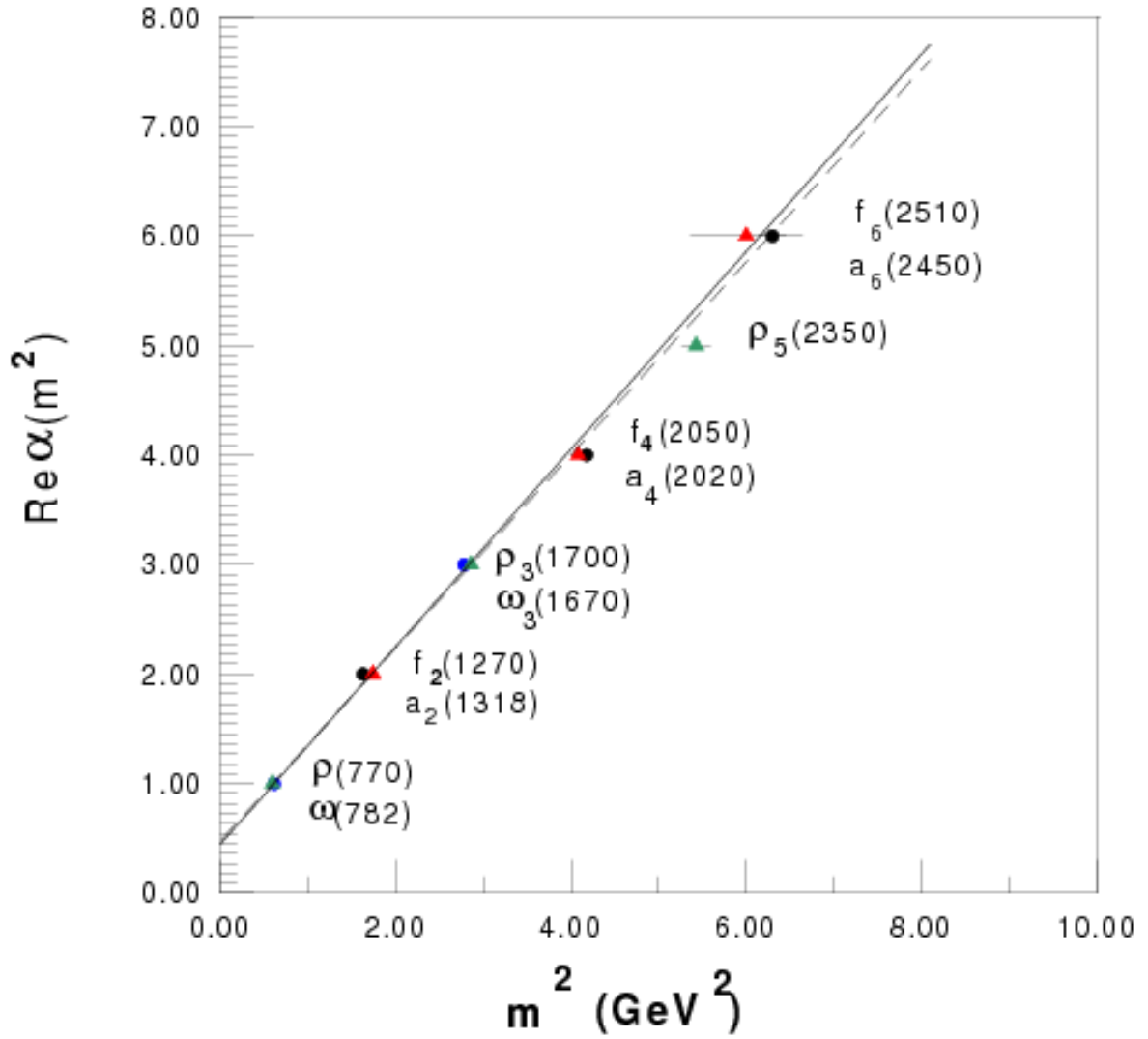


Figure 3: Here the mass squared of the mesons are plotted against their angular momentum, i.e. the real part of $\alpha(t)$. The mass squared is equivalent to the s-channel, and we can then extend the trajectory into the t-channel. [42]

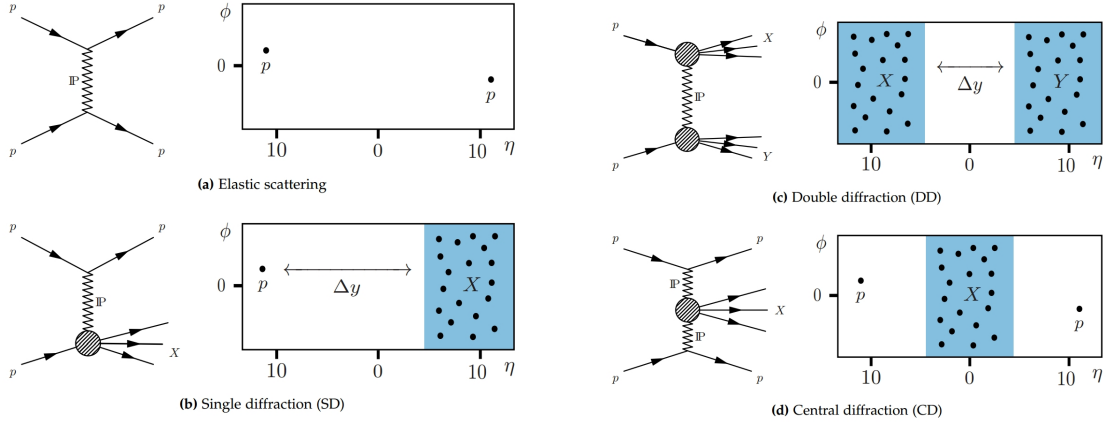


Figure 4: [37] The figure shows the elastic and the different diffractive topologies in rapidity space and ϕ space. The cross sections are $\sigma_{el} > \sigma_{sd} > \sigma_{dd} > \sigma_{cd}$.

that the total cross section is actually constant, or rather slowly rising. A new trajectory was needed with intercept $\alpha(0) \geq 1$. The Pomeronchuk Theorem[35] tells us that an exchange object that contributes at large s (i.e. $\alpha(0) \geq 1$), must have quantum numbers of vacuum. This object is referred to as the Pomeron. No resonances are known to lie on the trajectory of this object. The Pomeron intercept is usually written in terms of ϵ , where $\alpha(0) = 1 + \epsilon$.

At very high center of mass energy, it is then expected that the diffractive interaction is completely dominated by Pomeron exchanges, and that the contributions from other Reggeons are negligible.

Diffractive

The information in this section is from reference [18]. The diffractive interaction is characterized by no exchange of quantum numbers and a large gap in rapidity space between the different systems of final state particles. The first type of diffraction is called single diffraction, $pp \rightarrow p + X$, where X indicates a system of particles with the same overall quantum numbers as the proton. In essence, this process can be thought of as the diffractive excitation of a proton. As can be seen on Figure 4, there will be a large gap in rapidity space between the final state products. The second process is double diffraction. This is $pp \rightarrow X + X$, where again the X represent a system of particles with the same quantum numbers as the initial proton it dissociated from, and there is a large rapidity gap between these dissociated protons. Finally there is Central diffraction, which is represented as $pp \rightarrow p + X + p$. There exists central inclusive processes where the protons dissociate, and exclusive, where they remain intact. Again there is the characteristic large rapidity gap between the protons and the central product. In general it can be thought of as diffractive excitation of the vacuum from two protons glancing each other. Because the main exchange of all these processes is in the t-channel, the non-excited protons will often be slightly scattered in an angle in ϕ .

Double Pomeron Exchange

Double Pomeron Exchange [2] is a specific case of central exclusive production $pp \rightarrow p + X + p$, where the central product is produced in the channel $\mathbb{P}\mathbb{P} \rightarrow X$. The only Regge trajectory that contributes significantly at high center of mass energy is the Pomeron. This means that a very large fraction of central diffraction interactions at high s are via Double Pomeron

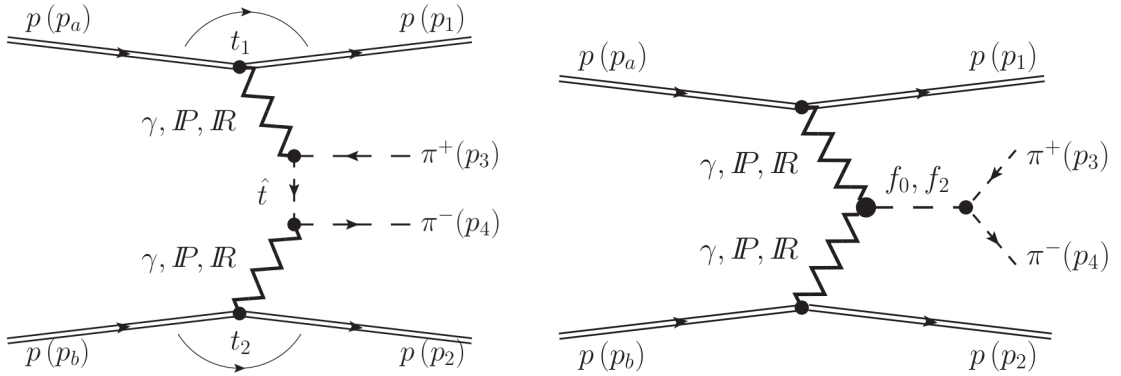


Figure 5: Central exclusive production of two pions [26]. One is produced via continuum, another via a meson resonance. The possible exchange objects are Pomerons, Reggeons and Photons. Pomerons dominate at high \sqrt{s} .

Exchange, since the contribution from other reggeons are suppressed. Double Pomeron Exchange puts very tight constraints on the centrally produced system. It must have total charge $Q = 0$, J even, no overall flavor and $CP = ++$. In Figure 5, two Born level diagrams of central exclusive dipion production can be seen. On the right hand diagram an intermediate meson state is produced, which then decays to the dipion final state. This state is subject to the DPE conservation laws. The pion spectrum is generally dominated by the ρ meson, but since it is $J = 1$, it cannot be produced via DPE. The same goes for K and \bar{K} states, since they have $CP = -+$. The dipion invariant mass spectrum is therefore significantly different, when the pions are produced in DPE.

PYTHIA approach for Central Diffraction

In PYTHIA [39] central diffraction is modeled using a phenomenological function called the Pomeron flux, $f_{\mathbb{P}/p}$. It is essentially a PDF that describes the distribution of pomerons around a proton. Different models for describing the flux exists.

One of these is the Donnachie-Landshoff model [1]. The model was originally made for single diffraction, but in PYTHIA8 central diffraction has been included. Another parametrization is the Minimum Bias Rockefeller Parameterization[43], which includes single, double and central diffraction. While the Pomeron flux is parametrized differently in the two models, they both share the overall form of:

$$f_{\mathbb{P}/p} \propto e^{\Delta y(2\alpha(t)-1)} \quad (14)$$

Central diffraction is then described by removing a Pomeron from each of the protons:

$$f_{DPE} \propto \prod_i e^{\Delta y_i(2\alpha(t_i)-1)} \quad (15)$$

The Scalar and Tensor Mesons below 2 GeV

This section is based on [20],[41] and [40], if not otherwise mentioned.

Since pQCD cannot be used to calculate properties of low energy bound states, the current understanding of the low mass scalar mesons are poor. It is, however, quite likely

that these scalar mesons are important in QCD, since they are supposed to play a key role in the nucleon-nucleon interaction, and the spontaneous breaking of the chiral symmetry, which in turn generates the mass of the proton. All these mesons have a long history and have been detected in several experiments over the last 60 years. They are very difficult to measure and distinguish, since they are heavily overlapping, and there are strong interference effects, which are difficult to model properly. The mesons mentioned in this section are particularly important for $\pi\pi$ production at high \sqrt{s} . This is due to DPE only producing states with J even and $CP = ++$, which these mesons all have. They also all have isospin $I^G = 0^+$. In Table 1, the current PDG values for the mass and widths of the mesons can be seen[25].

Meson	Mass [MeV]	Width [MeV]
$f_0(500)$	400 - 550	400 - 700
$f_0(980)$	990 ± 20	40 - 100
$f_0(1275)$	1275.5 ± 0.8	$186.7^{+2.2}_{-2.5}$
$f_0(1370)$	1200 - 1500	200 - 500
$f_0(1500)$	1504 ± 6	109 ± 7

Table 1: The current world average for the scalar meson parameters. Taken from the Particle Data Group[25].

$f_0(500)$ meson

The $f_0(500)$ [41] is one of the most controversial yet also most important scalar mesons. Due to its extremely large width, it is heavily overlapping with several of the other scalar mesons. This makes measurements of its mass and width model dependent. The large uncertainties on the width and mass, seen in Table 1, are not due to lack of measurements, but rather because the results across experiments, are highly inconsistent at present.

The $f_0(500)$ meson plays an important role in QCD via the linear sigma model. The QCD invariance under $U(2)_L \times U(2)_R$ transformations are known as the chiral symmetry. In essence, the theory is invariant, when rotating the right- and left-handed components independently. This symmetry is spontaneously broken at low energies by non-perturbative QCD effects. This generates the mass of the nucleons, where the mass of the sum of the constituents are much lower than the overall mass. The linear sigma model now predicts the existence of a scalar meson around 500MeV. This happens in analogy to the prediction of the Higgs boson in the spontaneous symmetry breaking of the Higgs field[20].

While the $f_0(500)$ meson is not expected to be a pure gluon state (the mass is too low), it is definitely not an ordinary $q\bar{q}$ state. Instead, it could quite likely be some kind of mixed gluon-quark state.

$f_0(980)$ meson

This meson is generally considered a multi-quark state. It appears as a resonance in the pion spectrum of $J/\psi \rightarrow \phi\pi^+\pi^-$ decay, yet it is nearly absent in $J/\psi \rightarrow \omega\pi^+\pi^-$. This indicates that it has strange quark content[22]. It is also considered a glueball candidate, since using the framework of QCD sum rules to carry out non-perturbative QCD calculations, a mass of a scalar glueball is found to be around 0.9 – 1.1 GeV[40], which matches very well with the $f_0(980)$ meson. Using QCD sum rules, it can however also be found that the mass matches with a tetraquark state ($q\bar{q}q\bar{q}$)[47].

$f_2(1275)$ meson

This meson is the lightest tensor meson, and it is generally believed to be an excited $q\bar{q}$ -state. In principle it is possible for a glueball to be $J = 2$ in its ground state, however analysis of the decay branching ratios of the $f_2(1275)$ into $\pi\pi$, $\eta\eta$ and $K\bar{K}$, indicates that it matches a $q\bar{q}$ -state very well[3]. It is also believed from lattice QCD that the lightest tensor glueball has a mass above 2 GeV[40].

$f_0(1370)$ meson

The $f_0(1370)$ is a glueball candidate, however it is not visible in central diffractive pion production due to it overlapping with the $f_2(1275)$ meson. This can however make it appear that the apparent width of the $f_2(1275)$ meson is larger in $\pi\pi$ production, than observed in other decay channels. Even when using different channels $f_0(1370)$ -mesons exact width and mass is hard to determine, and its existence is still disputed to this day.

$f_0(1500)$ meson

This meson is a glueball candidate. Lattice QCD calculations predict the lowest glueball mass as somewhere from 1.5 – 1.7 GeV [40], which is in good agreement with the $f_0(1500)$ meson. Furthermore in the Belle experiment it was seen that the $f_0(1500)$ meson did not appear as a resonance in the process of $\gamma\gamma \rightarrow K\bar{K}$ or $\gamma\gamma \rightarrow \pi\pi$. A very weak to non-existent coupling to $\gamma\gamma$ is expected of a glueball state. The $f_0(1500)$ couples weakly to the $\pi\pi$ channel. If it were a $q\bar{q}$ state, then it would most likely have $s\bar{s}$ content. However its branching ratio to $K\bar{K}$ is reported to be very low, which would then contradict strange quark content. These properties seem to be in good agreement with a glueball state.

$f_0(1710)$ meson

Along with the $f_0(1500)$ this is a strong glueball candidate. Its mass matches slightly better with the lattice QCD calculations, than the $f_0(1500)$. Where the $f_0(1500)$ mainly decays into $\pi\pi$, the $f_0(1700)$ mainly decays into $K\bar{K}$. In the Belle experiment the $f_0(1710)$ resonance was seen in the $\gamma\gamma \rightarrow K\bar{K}$ channel, indicating a γ coupling, which implies quark content.

Resonance Fitting

It is important to include interference effects, when fitting the $\pi\pi$ mass spectrum due to the several overlapping resonances. The most precise way to extract the properties of these resonance is by finding the pole position in the complex plane using Roys dispersion relations. This is a complex theoretical procedure and an example of the extraction of the $f_0(500)$ meson parameters, can be found in [41]. A simpler alternative is to model the resonances as Breit-Wigners. To account for the interference effects, the spectrum can be modeled as the complex square of a series of complex Breit-Wigners. Each of the complex Breit-Wigners are modeled as [21]:

$$A_{\text{bw}}(m) = e^{i\phi} \frac{k\sqrt{M \cdot m \cdot \Gamma(m)}}{m^2 - M^2 + i\Gamma(m)m} \quad (16)$$

In this formula, M describes the Breit-Wigner mass, ϕ is the relative phase of the resonance, k refers to the amplitude and m refers to invariant mass of the pion system. Here, the width

is described as:

$$\Gamma(m) = \Gamma \cdot \left(\frac{\sqrt{\frac{m^2}{4} - m_\pi^2}}{\sqrt{\frac{M^2}{4} - m_\pi^2}} \right)^{2L+1} \quad (17)$$

Besides the resonances a continuum is fitted. No clear best model exists for the continuum. A simple model is used in this analysis:

$$\sigma_{\text{cont}} = A \cdot e^{-m/B} (m - 2m_\pi)^2 \quad (18)$$

The full fit formula for the differential cross section is then:

$$\frac{d\sigma}{dm} = \sigma_{\text{cont}} + \left| \sum_{n=\text{Resonances}} A_{\text{bw},n} \right|^2 \quad (19)$$

While this model is an approximation it fits data well.

The Large Hadron Collider

To investigate the smallest scales of physics, interactions at high energies are needed. The approach used at the Large Hadron Collider is to take two protons and collide them near the speed of light. In this section the technical aspects of the collider are described, and a short review of some basic accelerator concepts are presented. Unless otherwise mentioned, the information is from reference [8] and [19].

Overview

The LHC is a circular collider with a circumference of 27 km. It consists of two beam pipes, which each are around 4 cm in diameter. The beams move in opposite directions around the LHC. Since it is a circular collider the proton trajectories need to be bent, which is achieved using superconducting dipole magnets. There are four collision points, and at each of these the beam pipes merge. The four LHC experiments, ALICE, ATLAS, CMS and LHC-B, are located at these collisions points. It is necessary to have almost perfect vacuum in the beam pipes since the protons can collide with air molecules.

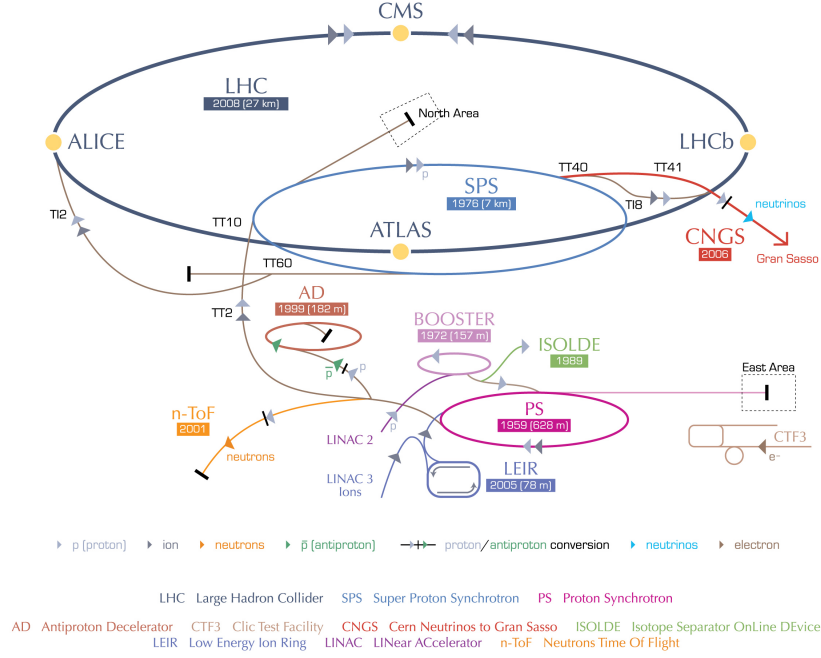
At the LHC pure proton samples are needed for the collision. To produce these, an electric field is applied to a gas of hydrogen to remove the electrons. The next step is to accelerate the protons. The accelerator complex can be seen on Figure 6. Here the protons start at the linear accelerator, LINAC2, where they are accelerated to an energy of 50 MeV. Next the three circular colliders, BOOSTER, PS and SPS, accelerate the protons to 450 GeV. The LHC is then filled with these high energy protons, and they are then accelerated to 7.5 TeV. The acceleration is achieved using RF-cavities, which accelerate the protons using an electric field. The phase of the cavity is adjusted such that low energy protons in a specific bunch are given a larger boost, whereas the protons with high energy are given a smaller boost. The protons in the collider are separated into several bunches, and the cavity phase helps preserve this structure.

During running a collection of particles, which are not following the designed beam trajectory, accumulates around the beam. This is called the beam halo. To avoid background and damage to the LHC, these need to be removed. This is achieved using a series of collimators, which can be moved in and out to scrape the beam. When the halo particles hit the collimators they form showers of particles, which then hit the secondary collimators and potentially form further showers, which then can hit the tertiary collimators.

Beam Physics

Since the beam conditions are important for the reconstruction of outgoing proton scattering angles, a short review is presented here.

CERN's accelerator complex



European Organization for Nuclear Research | Organisation européenne pour la recherche nucléaire

© CERN 2008

Figure 6: The CERN accelerator complex. Picture from [7]

Luminosity

The Luminosity is defined as the quantity that relates the number of events over a certain period of time to the cross section for the process:

$$\mathcal{L} \cdot \sigma = \frac{dN}{dt} \quad (20)$$

Here \mathcal{L} is the instantaneous luminosity. In a collider like the LHC, where particle bunches are colliding at some frequency the formula becomes:

$$\mathcal{L} = f \cdot n_B \frac{n_1 n_2}{4\pi\sigma_x \sigma_y} \quad (21)$$

Here f is the frequency, n_B is the number of beam bunches, n_1 and n_2 is the number of protons in the respective bunches and σ_x, σ_y describe the beam size in the transverse plane. When integrating over the time for a specific data run we then have the integrated luminosity:

$$\sigma \cdot L = N \quad (22)$$

Another important quantity is the pile-up. It is the average amount of inelastic interactions per crossing (so elastic scattering is not included). The quantity is simply found as:

$$\mu = \frac{\mathcal{L} \cdot \sigma_{in}}{f} \quad (23)$$

Here f is the frequency of crossings, and σ_{in} is the inelastic cross section.

Emittance and Beam Optics

The equations of motion for particles moving through a series of quadrupoles, dipoles and free drift space can be described using Hill's equations. It can be derived from these that the phase space (u, u') of a beam particle is at any given point, s , in the magnetic field within the ellipse given by the boundaries [30]:

$$u_{\max} = \sqrt{\epsilon\beta(s)}, \quad u'_{\max} = \epsilon \frac{1 - \frac{1}{4}\left(\frac{d\beta(s)}{ds}\right)^2}{\beta(s)} \quad (24)$$

Here u is either of the two transverse coordinates, and $u' = \frac{du}{ds}$. While the shape of the ellipse changes a function of s , the overall area of the ellipse is always $\pi\epsilon$. Here $\beta(s)$ refers to the β function, which encapsulates the information about the orbit. The value of the beta function at the interaction point is called $\beta(s_{\text{int}}) = \beta^*$. As can be seen from equation (24), a small β^* gives a small u_{\max} , which then gives a high luminosity. This is ideal for the standard LHC beam. However a small β^* gives a large u'_{\max} , which corresponds to beam divergence. This means that the incident angles of the colliding beams are unknown, which then gives an uncertainty on any reconstructed scattering angle of an outgoing proton. Therefore a high β^* is preferred for forward physics.

A particle with design beam momentum can be transported from the starting phase space position of (x_0, x'_0) to (x, x') using the transport matrix.

$$\begin{bmatrix} x \\ x' \end{bmatrix} = \begin{bmatrix} M_{11} & M_{21} \\ M_{12} & M_{22} \end{bmatrix} \begin{bmatrix} x_0 \\ x'_0 \end{bmatrix} \quad (25)$$

Here the four coefficients of M are given by the magnet configurations between the two points x and x_0 . The existence of beam energy divergence of the proton gives an extra degree of freedom, $\Delta p/p$, and the transport matrix then has to be extended to a 3×3 matrix.

The ATLAS Detector

The information in this chapter is from reference [24] unless otherwise mentioned. The ATLAS detector is located at collision point 1 of the LHC ring as seen on Figure 6. In this analysis the ATLAS detector is used to measure the central system of particles produced in central exclusive production. Only specific parts of the detector are used for this analysis, and these will be discussed in detail.

As can be seen on Figure 7 and 8 the ATLAS detector is a layered detector, where the layers has different purposes. The innermost layers are mainly used to track charged particles, and a large magnetic field is applied over these layers, causing charged particles to bend. This allows for the momentum to be reconstructed based on the trajectory. This specific analysis is mainly concerned with these inner layers, since the particles of interest, low p_t charged pions, will not reach the outer layers.

The outer layers of ATLAS are calorimeters. The inner calorimeter is an electromagnetic calorimeter, which is mainly used to measure the energy of photons and electrons. It is a sampling type EM calorimeter with a passive lead layer and an active Liquid Argon layer. An electromagnetic calorimeter, which would be able to detect low energy photons, would be very useful for diffractive studies, since they would allow identification of π^0 decaying to $\gamma\gamma$. However the efficiency of the LAr calorimeter for low p_t photons is extremely low.

Beyond the electromagnetic calorimeter is the hadron calorimeter. The goal of this is mainly to measure high energy pions, which often pass through the EM calorimeter. Here the passive layer is made from steel and the active layer is plastic tile scintillators.

The outermost layer is the muon chamber, made to detect muons which otherwise pass through the other layers. A magnetic field produced by large toroid magnets surround the muon system in order to measure the momentum of the muons. Drift tubes with an argon gas mixture are used for detecting the muons.

Inner Detector

The momentum reconstruction of the detected particles is crucial to any physics analysis. At ATLAS this is done by measuring tracks of particles moving through a magnetic field using the ATLAS Inner Detector. It is surrounded by a solenoid superconducting magnet, which creates a 2 T magnetic field, parallel to the ATLAS z-axis (the beam axis). The ATLAS Inner Detector spans the region of $|\eta| < 2.5$, and it consists of three different layers all used for tracking charged particles. The two innermost are silicon based and the outer is a straw-tube detector. The overall efficiency of the detector will be discussed later in this thesis. An image of the ATLAS Inner Detector can be seen on Figure 9.

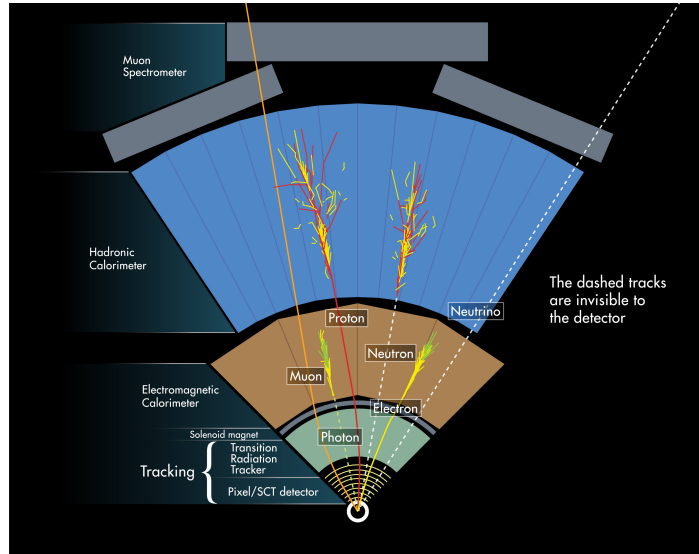


Figure 7: Cross section of the ATLAS detector[5], and the different detector signatures of different particles. Here a pion would look the most like the proton and electron tracks, however pions produced in central diffraction will not reach outside the Inner Detector, because the track curls too much due to the low p_t .

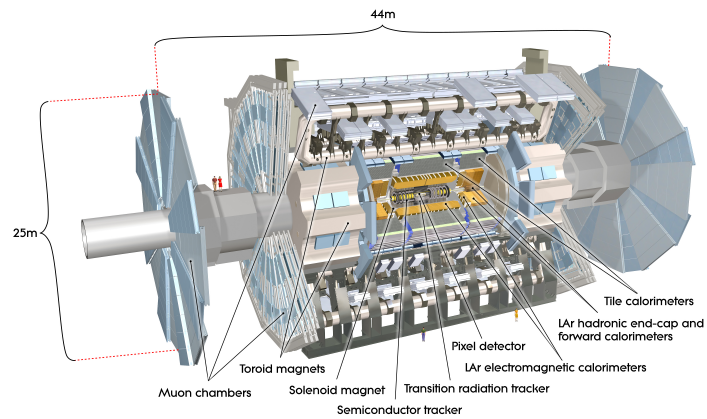


Figure 8: The ATLAS detector. [4]

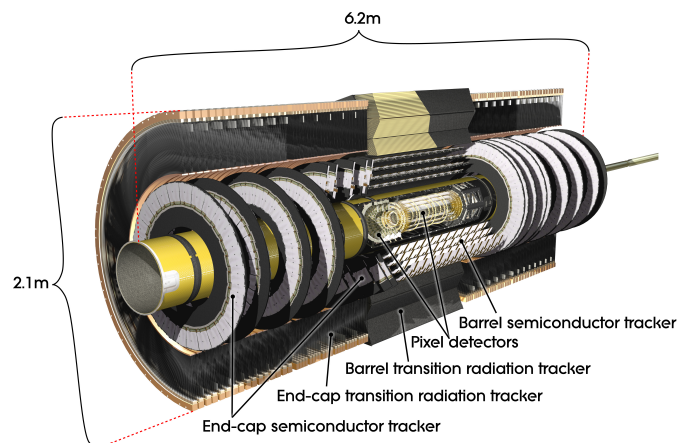


Figure 9: The ATLAS Inner Detector. [32]

Pixel Detector

The innermost detector right outside the LHC beampipe is the pixel detector. It consists of three barrel layers and three disks in each end cap. The detector consists of 1744 modules, which each has 47232 pixels. These pixels each has a thickness of $250\mu\text{m}$ and a size of $50 \times 400\mu\text{m}^2$. The pixels are made from silicon, which is doped such that a depletion zone is created. By applying a voltage over the cell, this is further amplified. When a charged particle passes through the pixel, it creates electron-hole pairs in the detector. These move to the electrode, creating a current, which gives a signal. Because of the large amount of very small pixels, which each can detect particles, the detector has an extremely fine resolution of $10 \times 115\mu\text{m}^2$ in $R - \phi \times z$. An additional innermost layer called the IBL was installed in 2014 with 12 million pixels of dimension $50 \times 250\mu\text{m}^2$

SCT detector

The Semiconductor Tracker is also silicon based, and the same principle for detection is used as in the pixel detector. It is however not pixel based, but instead it uses strips. This provides inferior resolution to the Pixel Detector. There are 4,088 sensors, which has 768 readout strips on both sides. The silicon strips are spaced out with $80\mu\text{m}$ between each. The sensors have a size of $6.36 \times 6.40\text{cm}^2$. These are distributed into four different cylindrical barrel layers, and 18 planar end cap disks. The resolution of the detector in the transverse direction is $17\mu\text{m}$ and $580\mu\text{m}$ in the longitudinal direction.

TRT detector

The outermost layer is the Transition Radiation Detector, which is made from drift tubes layered between material, which can cause electrons to emit transition radiation. The straws are around 144 mm long and have a diameter of 4 mm. They are filled with a xenon based gas mixture, and they have an anode wire in the center. When a charged particle passes through a straw, electrons are freed, and they drift to the anode. The drift time can then be used to find the track coordinates. Generally particles with $p_t < 0.5\text{GeV}$ will not reach the TRT.

Trigger System

In order to observe rare events, the LHC needs a large collision rate. This rate is much higher than the rate at which you can process and save events. Since most of the produced events from these collisions are not of interest, a trigger system is needed to select, process and save the events deemed important.

The ATLAS trigger system[29] has three levels. The first is a level 1 trigger, which is a hardware trigger implemented in the electronics. When the level 1 trigger fires, it can then activate the next level, which is the High Level Trigger (HLT). This is software based and running on a computer farm. It consists of two levels. The first is the level 2 trigger, which can access the full detector. It can execute reconstruction algorithms, and advanced event selection criteria can therefore be implemented. The second part of the HLT is the event filter, which does the final processing and saving of the data.

MBTS

The Minimum Bias Trigger Scintillator consists of doped polystyrene scintillators. They are arranged in two disks on each side of the interaction point, and are labeled A and

C respectively. These disks are split into 8 wedges. They have an inner and an outer component. The outer covers the $2.76 < |\eta| < 3.86$ and the inner covers $2.08 < |\eta| < 2.76$. When light is emitted from the scintillator it is collected by wavelength shifting fibers, which are then connected to PMTs.

The ALFA Detector

The Absolute Luminosity For ATLAS Detector [33] is a forward sub-detector of the ATLAS system. It is originally designed to measure elastic scattering at small angles, since this can be used to determine the ATLAS Luminosity. The ALFA detector can, however, also be used to tag forward protons in order to measure diffraction.

Overview

The ALFA detector is made to detect proton hits in the plane perpendicular to the beam axis, which is the (x, y) -plane in the beam coordinate system. The ALFA detector consists of four detector stations, two on each side of the interaction point. Each station consists of a detector above the beam, and a detector below the beam. The inner station is 237 meters from the interaction point, and the outer station is 245 meters away. Each detector can be lowered down into the beampipe, as close as one millimeter from the beam. Each of the detectors are equipped with a main detector, and an overlap detector that can be used to align the different stations.

Main Detector

The main detectors use scintillating fibers to detect the protons, and the detector shape in the (x, y) -plane can be seen as outlined by proton hits on Figure 11. There are 20 layers, which each consists of 64 square fibers. The dimensions of these fibers are $500 \times 500 \mu\text{m}^2$. The layers are glued to aluminum plates. There are ten plates and each have a fiber layer glued to the front and to the back. These two fiber layers are perpendicular to each other, and they are called the U- and V-layers. They overlap in the tracking region, where there is also no aluminum in order to avoid multiple scattering inside the detector. Each of the layers are staggered by $50\mu\text{m}$ with respect to the previous layer, since this improves the detector resolution. The layer efficiency is around 90%. The fibers in a single layer are connected to a 64 channel Multi Anode Photomultiplier Tube. The fibers are connected to the MAPMT such that neighboring channels do not correspond to neighboring fibers.

Track Reconstruction

The proton tracks that pass through ALFA can be considered perpendicular to the detector, since the scattering angles are so small. First a U- and V-coordinate are extracted independently. When a proton passes through the detector it hits fibers in many of the U-layers and V-layers. The tracking algorithm[34] checks if the fibers that are hit in each of the layers overlap. The overlapping region is then used to find the position. The most probable coordinate is the one with the most overlapping fibers. By then cross-referencing the U- and V-layers a hit position in the ALFA coordinate system is found. The staggering of fibers gives a better resolution, since each fiber has a smaller overlapping area. The minimum

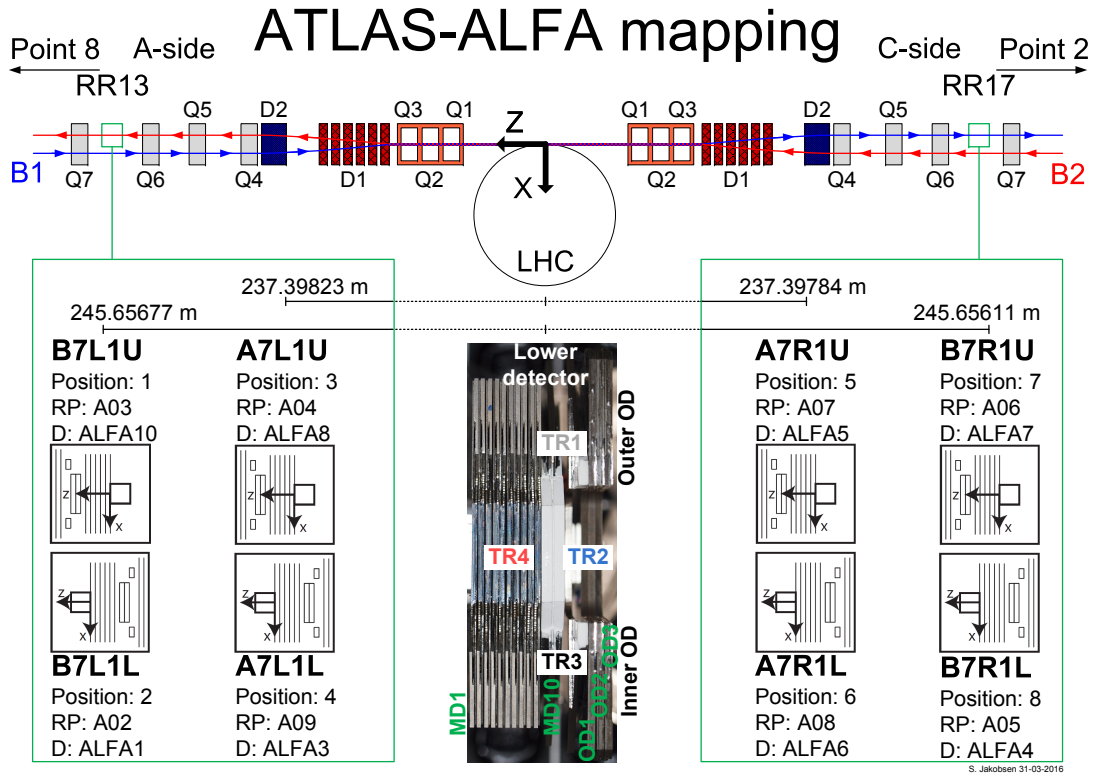


Figure 10: The ALFA detector setup in relation to the ATLAS interaction point.

track criteria are 3 overlapping fibers in the U-layer and in the V-layer. Furthermore, a noise suppression cut is implemented, which requires a maximum of 3 fiber hits in at least 3 of the U- or V-layers. This cut is necessary, since it prevents tracks generated by a noisy PMT, which would give many hits in a single layer. The resolution is about $30\mu\text{m}$ in the inner stations, and around $40\mu\text{m}$ in the outer stations due to multiple scattering.

Because the U- and V-layers measure coordinates independently, there is a significant probability of getting ghost tracks, which are created from detector noise. Furthermore two protons going through the detector generates four tracks, two real proton tracks and two combinatoric ghost tracks as can be seen on Figure 13. This will be discussed in more detail in a later section.

Overlap Detectors

The overlap detectors are used to measure the distance between the upper and lower ALFA detectors in a station. This can be used to align the detectors in the y-direction. The ODs consists of 3 horizontal fiber layers with 30 fibers in each. A single ALFA station has two overlap detectors, one connected to the upper MD and one to the lower. These are designed to overlap inside the beam halo. A halo proton can then be measured in both ODs and the relative distance between the MDs can be found.

Roman Pots

The detectors have to be lowered inside the beam pipe, but they need to be protected from the beam pipe vacuum. They are therefore placed inside Roman Pots. One of these can be

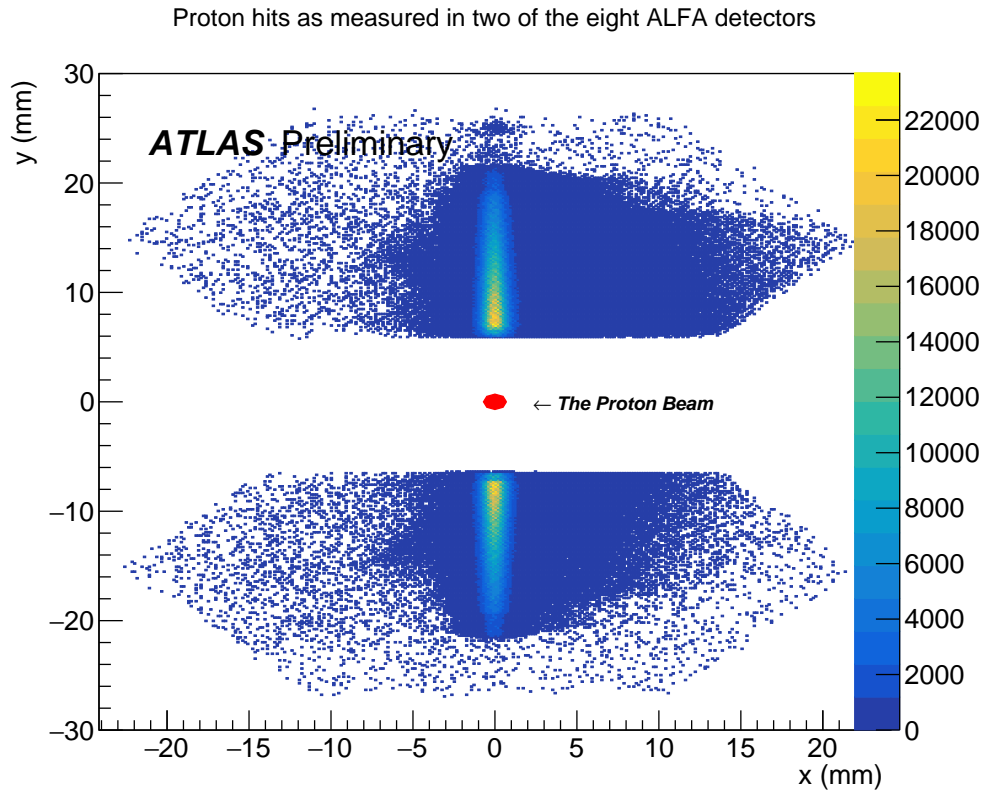


Figure 11: Proton hits in one of the ALFA stations is shown here. The shape of the detector is outlined by proton hits taken from data. The detectors are around 6mm away from the beam, but they can be moved closer.

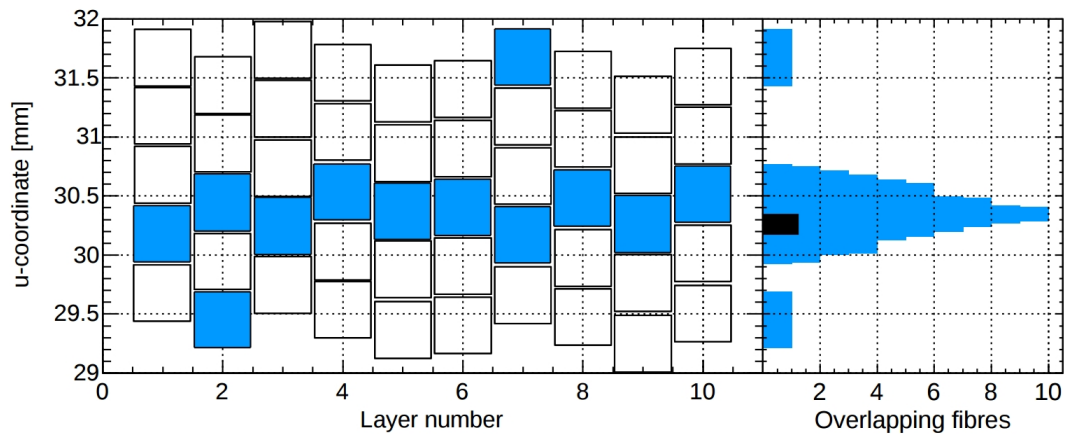


Figure 12: Track reconstruction in the ALFA detector. A track is reconstructed independently in the U-layer and V-layer by checking overlapping fibers. The proton is concluded to be in the area where all the fibers overlap.[10]

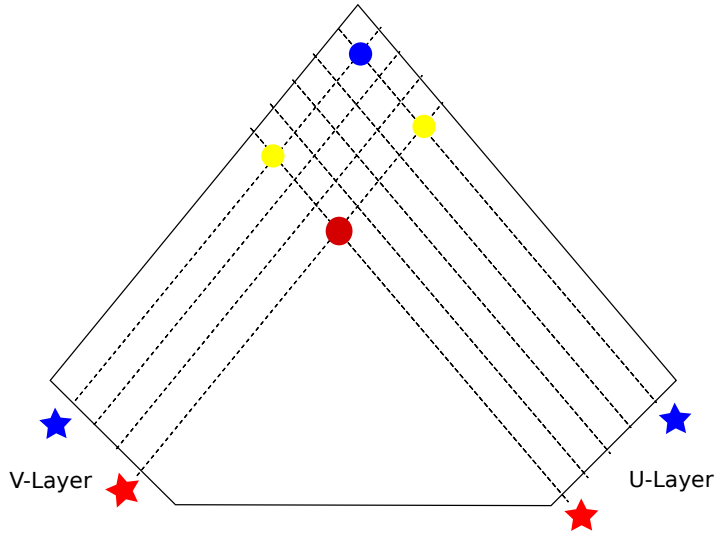


Figure 13: A diagram of a two proton event, which generates ghost tracks with completely different coordinates. The first proton hit is indicated as the red dot. It generates fiber activity in a specific V-layer fiber and U-layer fiber, marked with the red star. The second proton is the blue dot, which activates two fibers as well. Since four fibers are showing signal, two ghost tracks marked as yellow dots are constructed from the combinatorics.

seen on Figure 14. A pot with an interior, which is under normal pressure, cannot be lowered into the LHC vacuum, since the pressure difference would cause the pot to break, or, at the very least, bend outward down into the beam. To circumvent this, the Roman Pots have an empty buffer layer with slightly lower vacuum, than inside the detector volume, while having slightly higher pressure than the LHC vacuum. This minimizes any outward bend. The distance between the outer edge of the Roman Pot to the detector edge is $450\mu\text{m}$. The Roman Pot wall in front of the detector is about $500\mu\text{m}$. It is important to make this thin, since it decreases the chance of a signal proton interacting with the pot material.

Trigger System

The ALFA detector has its own L1 trigger system. In front of the main detectors tracking region are two plastic scintillator tiles. They are separated by a distance of 3mm. These two are connected in coincidence to minimize trigger noise. These 8 pairs of scintillator tiles are used in different logic combinations to form the L1 trigger items. The most important ones for this analysis is shown below. What detector a trigger item refers to can be seen on Figure 10.

$$\text{L1_ELAST15} = (\text{B7L1U}|\text{A7L1U})\&\&(\text{A7R1L}|\text{B7R1L})$$

$$\text{L1_ELAST18} = (\text{B7L1L}|\text{A7L1L})\&\&(\text{A7R1U}|\text{B7R1U})$$

$$\text{L1_SYST17} = (\text{B7L1U}|\text{A7L1U})\&\&(\text{A7R1U}|\text{B7R1U})$$

$$\text{L1_SYST18} = (\text{B7L1L}|\text{A7L1L})\&\&(\text{A7R1L}|\text{B7R1L})$$

$$\text{L1_ALFA_ANY} = \text{B7L1U}|\text{A7L1U}|\text{B7L1L}|\text{A7L1L}|\text{B7R1L}|\text{A7R1L}|\text{B7R1U}|\text{A7R1U}$$

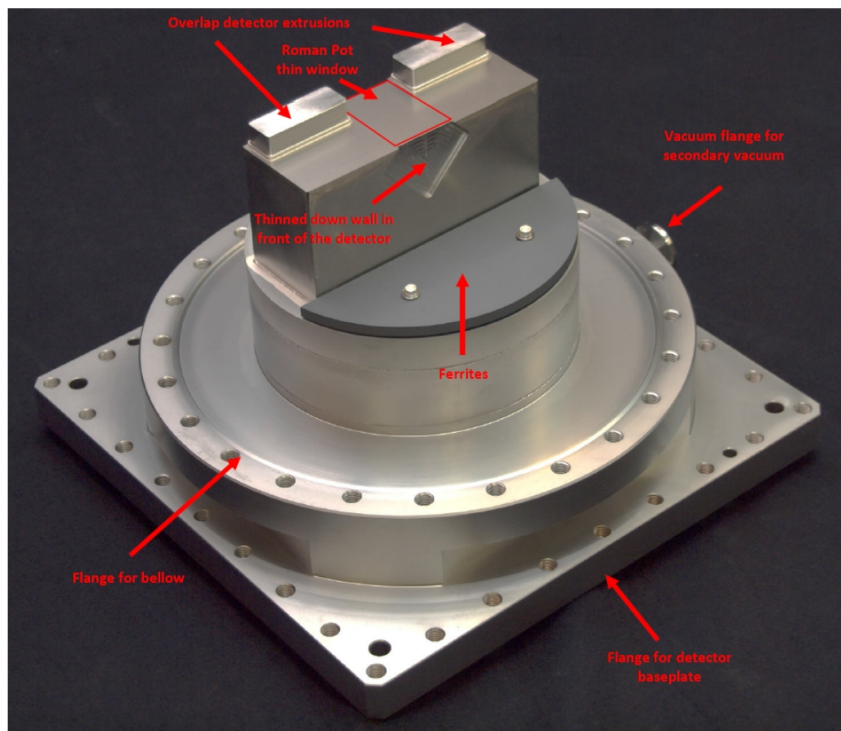


Figure 14: A picture of an ALFA Roman Pot.

Data Analysis

An analysis procedure has been developed to measure the cross section for the central exclusive dipion production process, $pp \rightarrow p + \pi^+\pi^- + p$ using the ALFA and ATLAS detectors. This procedure has also been extended such that it can be used to determine the cross section for the central exclusive four pion process, $pp \rightarrow p + \pi^+\pi^-\pi^+\pi^- + p$. In this chapter the analysis procedure is described in detail.

In the following chapter, the acceptances and detector efficiencies are determined. It was structured in this manner, since the determination of the efficiencies rely on the analysis techniques. Some of the efficiencies are, however, already applied on the data shown in this section, but this is not important to the actual analysis procedure.

Run Information

The data is taken from the ATLAS Runs 282026, 282420 and 282455, which were taken during the period of the 15th October 2015 to the 18th October 2015. The total integrated luminosity corresponds to 367.7nb^{-1} . There is a 3% uncertainty on the luminosity. The optics for the run was $\beta^* = 90\text{m}$ and the center of mass energy was $\sqrt{s} = 13\text{TeV}$. There were 671 colliding bunches and a pile-up of about $\mu = 0.1$. The crossing angle was $\theta_c = 2 \times 50\mu\text{rad}$.

Event Selection

On Figure 15 a typical signal event is illustrated. Since the process of interest is $pp \rightarrow p + \pi^+\pi^- + p$, all of the final state particles can be measured, which is the main selection criteria. At least one track is required in both ALFA detectors in a detector pair, and on both sides of the interaction point. At the same time two (or four) reconstructed tracks are required in the ATLAS Inner Detector with zero total charge. The events are classified into four different categories named after the corresponding ALFA trigger items i.e. ELAST15 (up/down), ELAST18 (down/up), SYST17 (up/up) and SYST18 (down/down).

A cut flow of the event selection without applying any weights can be seen on Figure 16. Many of these cuts are explained in more detail in the efficiency section. The first step is to apply the good run list. This is a check as to whether all detectors were working, and if the beam was stable during the examined event. It is then checked, if the HLT fired. It requires at least one track in Inner Detector, no activity in the MBTS and it requires that one of the L1 ALFA triggers fired.

If more than one of the four ALFA L1 triggers fired, the event is vetoed. Two tracks are required in the Inner Detector for the $\pi\pi$ analysis, and four tracks in the $\pi\pi\pi\pi$ analysis. The Inner Detector track requirements are exactly as in reference [12]. Every track need at least one pixel hit. An innermost pixel layer hit is also required, if the extrapolated track crosses

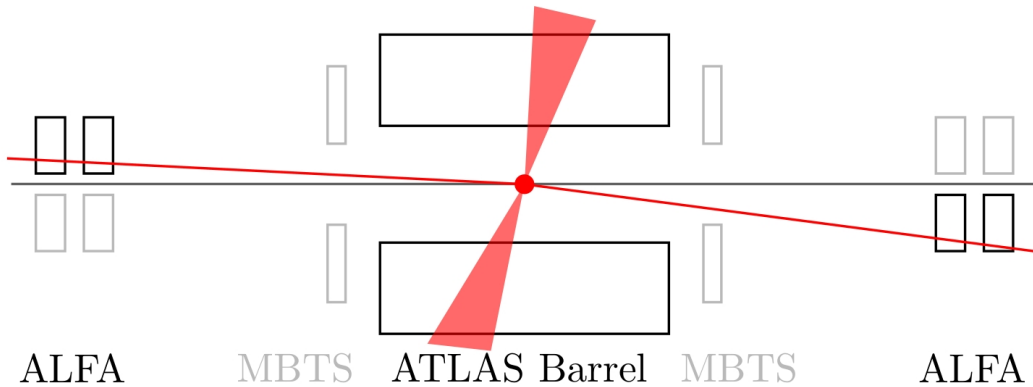


Figure 15: The experimental signature of a signal event with the ALFA trigger ELAST15. The black line represent the incoming protons, the red lines represent the two outgoing protons, and finally the red cones represent the central system. Figure from [38]

an active region of the pixel module. Since the track lengths depend on p_t , less SCT hits are expected for low p_t particles. Two SCT hits are therefore required for $p_t < 300\text{MeV}$, four SCT hits for $300\text{MeV} < p_t < 400\text{MeV}$, and six SCT hits for particles with $p_t > 400\text{MeV}$. The transverse impact parameter is required to be $|d_0| < 1.5\text{mm}$. This cut may be too strict for this analysis since the beam spot is quite wide due to the high β^* . Finally a cut is performed on $|z_0 \times \sin(\theta)| < 1.5\text{mm}$. No requirements are made of the TRT, because the tracks have low p_t , and quite often do not reach the TRT. The tracks all have $p_t > 100\text{MeV}$ and $-2.5 < \eta < 2.5$.

Then it is checked if there are proton tracks in the ALFA detectors. It is required that there is at least one track that has been reconstructed with more than 5 U-layer and 5 V-layer fibers in each of the signal pots. A noise suppression cut requires that any track should be reconstructed using 3 U-layers and 3 V-layers, where at most 3 fibers were hit. This is done to avoid tracks reconstructed purely from cross talk, since layers activated due to PMT channel cross talk have more than 3 active fibers. An edge cut is implemented that removes events reconstructed closer than 90 microns from the edge, in order to avoid edge effects. It is allowed that more than one track is reconstructed in a pot, since a single proton can create multiple tracks. Events that has specifically four tracks, where more than one meet the track requirements of more than 5 U- and V-layers, are vetoed, since these indicate two protons hitting the detector. Finally a reconstructed primary vertex is required in the Inner Detector.

In Table 2 a cut flow for two pion events can be seen, and in Table 3 it can be seen for four pion events. The momentum cut will be explained in the background section.

Cut Flow for Run 282455

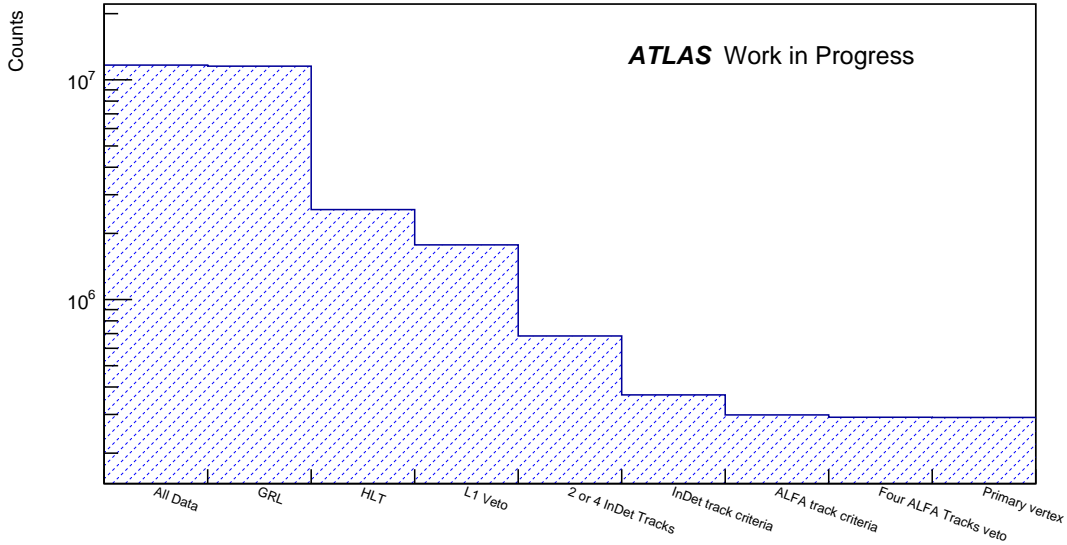


Figure 16: A cutflow of run 282455. The cut on the primary vertex barely does anything. Since the tracking criteria includes cuts on both $|d_0|$ and $|z_0 \times \sin(\theta)|$, then almost all tracks that pass these criteria will have a vertex.

$\pi\pi$ - events	OS ($\sum q = 0$)	SS ($\sum q \neq 0$)	SS/OS
HLT	2851485	473726	0.1661
L1 veto	2051353	333736	0.1626
InDet Tracking Criteria	1314908	126307	0.0961
ALFA Tracking Criteria	1073289	101156	0.0943
Four Track Veto	1049021	98374	0.0938
Reconstructed Vertex	1046541	98038	0.0937
5σ cut on $\sum \vec{p} = 0$	526223	10337	0.0196

Table 2: Cut flow for two pion events with the same sign charge (SS) and opposite sign charge (OS).

$\pi\pi\pi\pi$ - events	OS ($\sum q = 0$)	SS ($\sum q \neq 0$)	SS/OS
HLT	969471	411891	0.4249
L1 veto	683739	287835	0.4209
InDet Tracking Criteria	325747	80150	0.2461
ALFA Tracking Criteria	263151	64034	0.2433
Four Track Veto	256638	62289	0.2427
Reconstructed Vertex	256555	62266	0.2427
5σ cut on $\sum \vec{p} = 0$	61990	4951	0.0798

Table 3: Cut flow for four pion events with non zero total charge (SS) and zero total charge (OS).

Alignment

The detectors need to be aligned for each of the runs, and this is done using a data driven method. The detectors are transformed into the beam coordinate system, where the proton beam has the coordinates $(x, y) = (0, 0)$. The full alignment values are given in appendix

Detector 1 and 2 - Rotational alignment

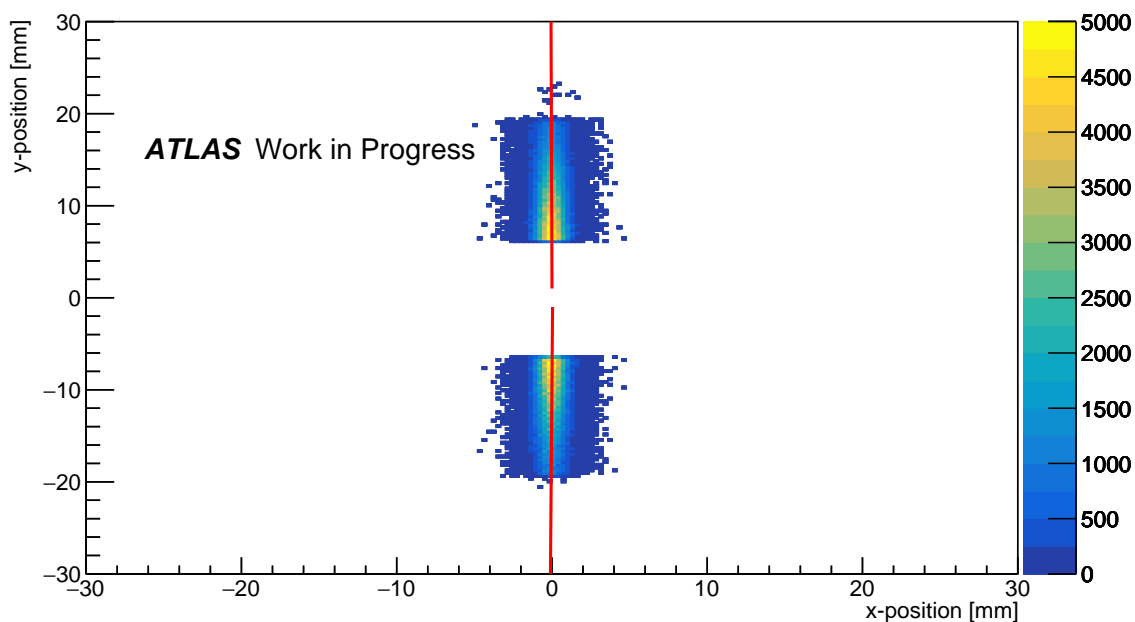


Figure 17: A first degree polynomial is fitted to each detector. The detector is then rotated until the slope is zero.

along with the coordinate transformation necessary to apply them to raw data. There are different values for the different runs, since the detectors are moved slightly in between these. This is a preliminary alignment, and only has limited precision. An official alignment should be made in the future by the ALFA group.

Distance Measurement

Using the overlap detectors a distance measurement between the detectors have been made by Prof. Adamczyk Lezcek [36]. This was done for one specific run, so some additional correction to y-alignment are needed to correct for the different runs. The detectors are symmetrical around the beam, so the detector edges are placed in the coordinates $(0, \frac{d}{2})$ and $(0, -\frac{d}{2})$, where d is the distance between the detectors. With this method the y-position for both the inner and the outer detector are obtained. The uncertainty on the position of the outer detector is however much larger.

Rotation

Elastic events are used to align the detector. The detectors can be rotated in the x-y plane relative to the beam. This rotation is measured by fitting a straight line to the hit map, and rotating the detector until the slope of the fit is zero as seen on Figure 17.

Relative x-alignment

Next the detectors are aligned in x by fitting a Gaussian distribution to the number of proton hits in the x-coordinates, and then shifting the entire detector by μ_x so the mean proton hit is in $x = 0$. This can be seen on Figure 18.

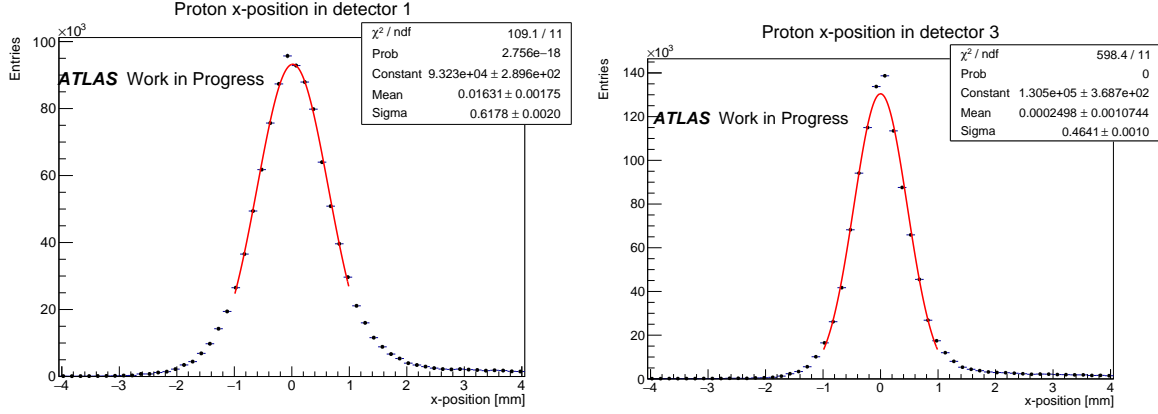


Figure 18: The x-coordinate of the proton hits are recorded. Since elastic events are symmetrical in the azimuthal angle, the elastic events will be Gaussian distributed around the beam center in x. The detectors are then aligned so the beam is centered in $x = 0$.

Relative y-alignment

A relative alignment in the y-coordinate between each detector pair is also made. The inner detectors are held fixed since the uncertainty on their position from the distance measurement is smaller than the outer detectors. The quantity $y_{\text{diff}} = y_{\text{outer}} - y_{\text{inner}}$ is plotted as a function of y_{inner} . This means:

$$y_{\text{diff}} = y_{\text{outer}} - y_{\text{inner}} = A \frac{p_y}{P} - B \frac{p_y}{P} = (A - B) \frac{p_y}{P}$$

The intercept should therefore be zero, if a straight line is fitted, so the detectors are shifted such that this is the case. This can be seen on Figure 19.

Event Reconstruction

The events are weighted based on the different efficiencies, which are determined in the following section. The Inner Detector efficiencies are applied on an event by event basis. The same is the case for the trigger prescales, since they are changing over the duration of the run. The HLT, and the SYST17 and SYST18 triggers, was rarely prescaled throughout the run. ELAST15 and ELAST18 were however prescaled. For every event the weight is determined as:

$$w = \frac{P_{\text{LI}} P_{\text{HLT}}}{A \cdot \epsilon_{\text{ALFAtrack}} \cdot \epsilon_{\text{IDtrack}} \cdot \epsilon_{\text{vertex}} \cdot \epsilon_{\text{L1}} \cdot \epsilon_{\text{L1VETO}} \cdot \epsilon_{\text{HLT}} \cdot \epsilon_{\text{pile-up}} \cdot \epsilon_{\text{4TrackVETO}}}$$

Here P is the prescale, and A refers to the geometric acceptance. The other efficiencies are described in the later sections. They are not important to the actual procedure of the analysis.

Momentum Reconstructions

The momentum of the protons can be reconstructed with the hits in the ALFA stations and the vertex in ATLAS using the knowledge of the beam optics. The predicted hit positions are:

The difference in y between detector 2 and 4 vs. the detector 4 y-coordinate

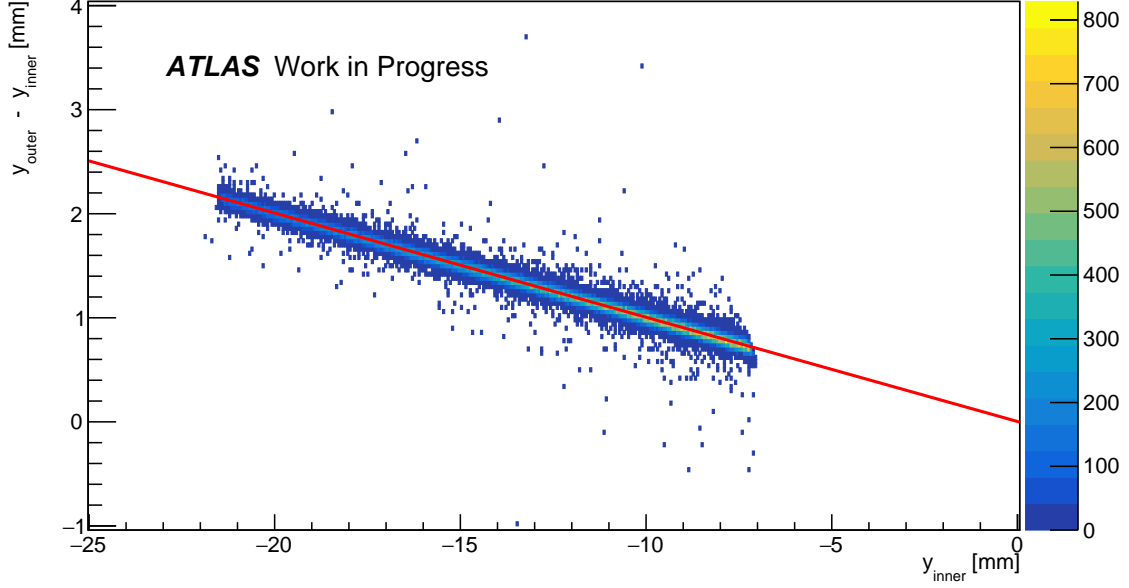


Figure 19: The relative y-alignment is made by finding the intercept of the plot of the inner detector y-coordinate as a function of the difference between the inner and outer detector y-coordinate.

$$x_{\text{theory},237,A} = A_{237,x,A}x^* + B_{237,x,A}\frac{p_{x,A}}{p_A} \quad (26)$$

$$x_{\text{theory},245,A} = A_{245,x,A}x^* + B_{245,x,A}\frac{p_{x,A}}{p} \quad (27)$$

$$y_{\text{theory},237,A} = B_{237,y,A}\frac{p_{y,A}}{p} \quad (28)$$

$$y_{\text{theory},245,A} = B_{245,y,A}\frac{p_{y,A}}{p} \quad (29)$$

These four equations exist for both the A-side and the C-side. The y-coordinate is independent of the vertex position since there is parallel to point optics in y. A χ^2 function is constructed.

$$\chi^2 = \sum_{S,z} \left(\frac{y_{\text{meas},S,z} - y_{\text{theory},S,z}}{\sigma_{y,z}} \right)^2 + \left(\frac{x_{\text{meas},S,z} - x_{\text{theory},S,z}}{\sigma_{x,z}} \right)^2 + \left(\frac{x_{\text{meas}}^* - x_{\text{theory}}^*}{\sigma_{x^*}} \right)^2 \quad (30)$$

Here S runs over A and C, and z runs over 237m and 245m. The uncertainty on the vertex is obtained from the ATLAS Inner Detector fit. The ALFA hits have an uncertainty of $\sigma_{237} = 0.03\text{mm}$ and $\sigma_{245} = 0.04\text{mm}$. The uncertainty is larger on the outer detector due to multiple scattering. Here p_x , p_y and x_{theory}^* are free parameters, and everything else is kept fixed. The MINUIT algorithm is then used to minimize the function. Fitted values for p_x and p_y for both protons are then used in the analysis. The reconstructed momentum can be seen on Figure 20. The y-momentum is originally centered around -325MeV , but the momentum has been shifted here due to technical reasons.

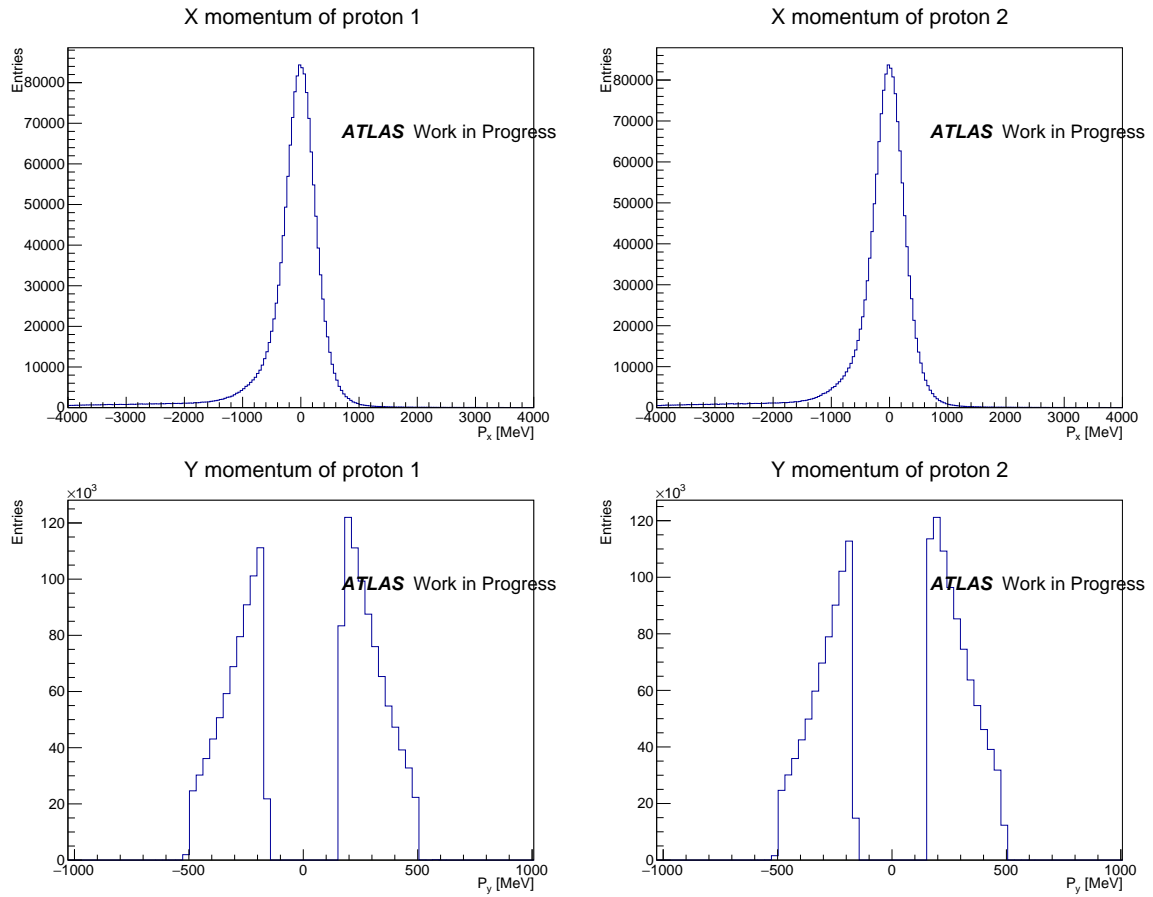


Figure 20: The reconstructed proton kinematics. The gap in the center of the p_y distribution is due to the detector acceptance. The y-momentum is not symmetric around zero due to the crossing angle. The tail in the p_x distribution are from particles with energy loss.

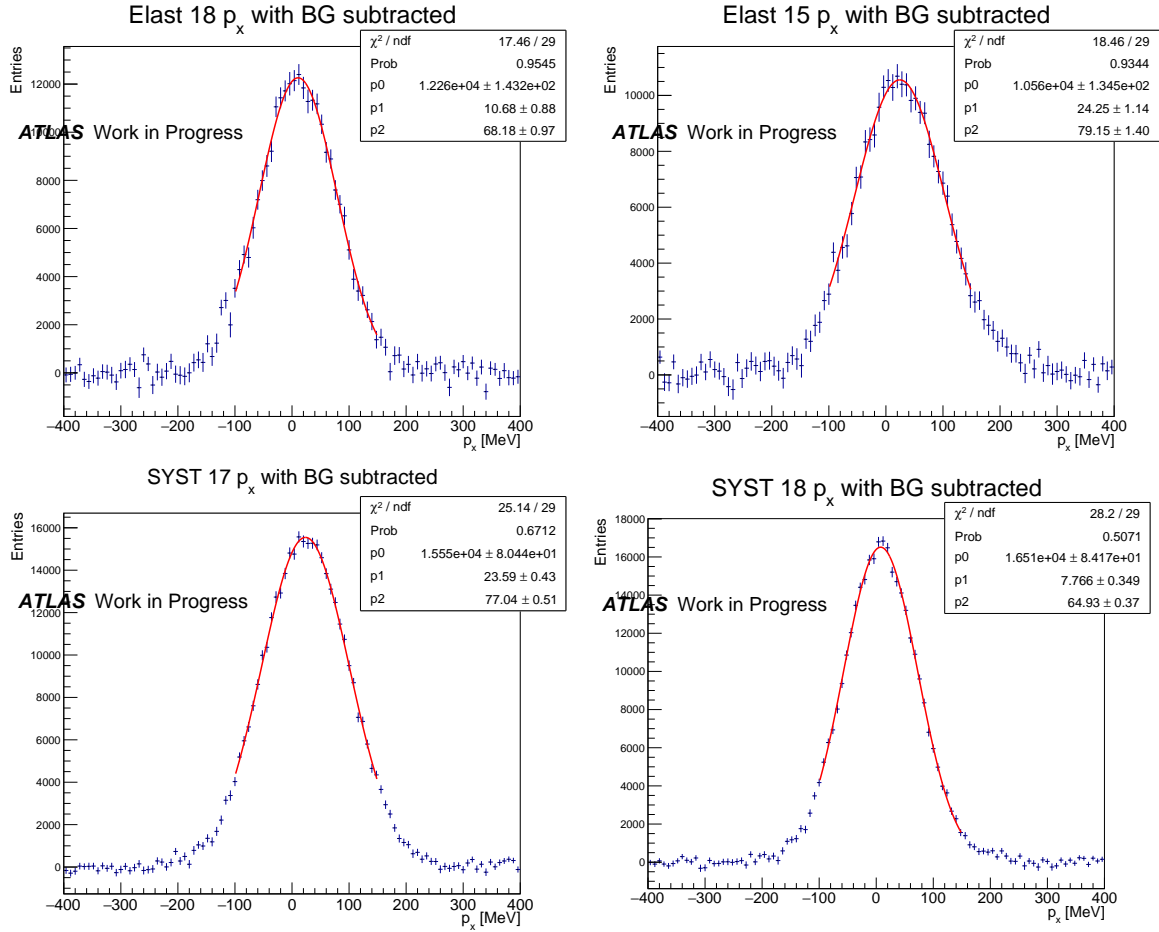


Figure 21: The total x -momentum of the four different arms.

Momentum Resolution of the Full System

When adding together all the final state particles, it would be expected for signal that there is $\sum p_x = 0$ and $\sum p_y = 0$. Therefore when plotting the $\sum p_x$ and $\sum p_y$ distributions with background subtracted, a Gaussian centered around 0 with a standard deviation corresponding to the total momentum resolution of the four particle system is expected. The method used for background subtraction is discussed in the next section. The different distributions are slightly shifted in p_x and p_y due to the alignment and optics not being completely perfect. The p_x distributions fitted with a Gaussian can be seen on Figure 21 and the p_y distributions can be seen on Figure 22. The different values for the resolution and mean values can be seen in Table 4.

Arm	σ_{p_x} [MeV]	x_c [MeV]	σ_{p_y} [MeV]	y_c [MeV]
ELAST15	79.3 ± 1.4	24.9 ± 1.2	24.7 ± 0.2	0.2 ± 0.2
ELAST18	67.4 ± 1.0	10.7 ± 0.9	24.6 ± 0.3	-4.2 ± 0.2
SYST17	76.9 ± 0.5	23.8 ± 0.4	25.0 ± 0.1	-8.1 ± 0.1
SYST18	64.8 ± 0.4	7.9 ± 0.3	25.2 ± 0.1	4.2 ± 0.1

Table 4: The momentum resolution of the full $p + \pi\pi + p$ -system.

As can be seen in Table 4 the momentum resolution in y is much better than in x . This is because of the parallel to point optics, which makes the reconstruction of the proton

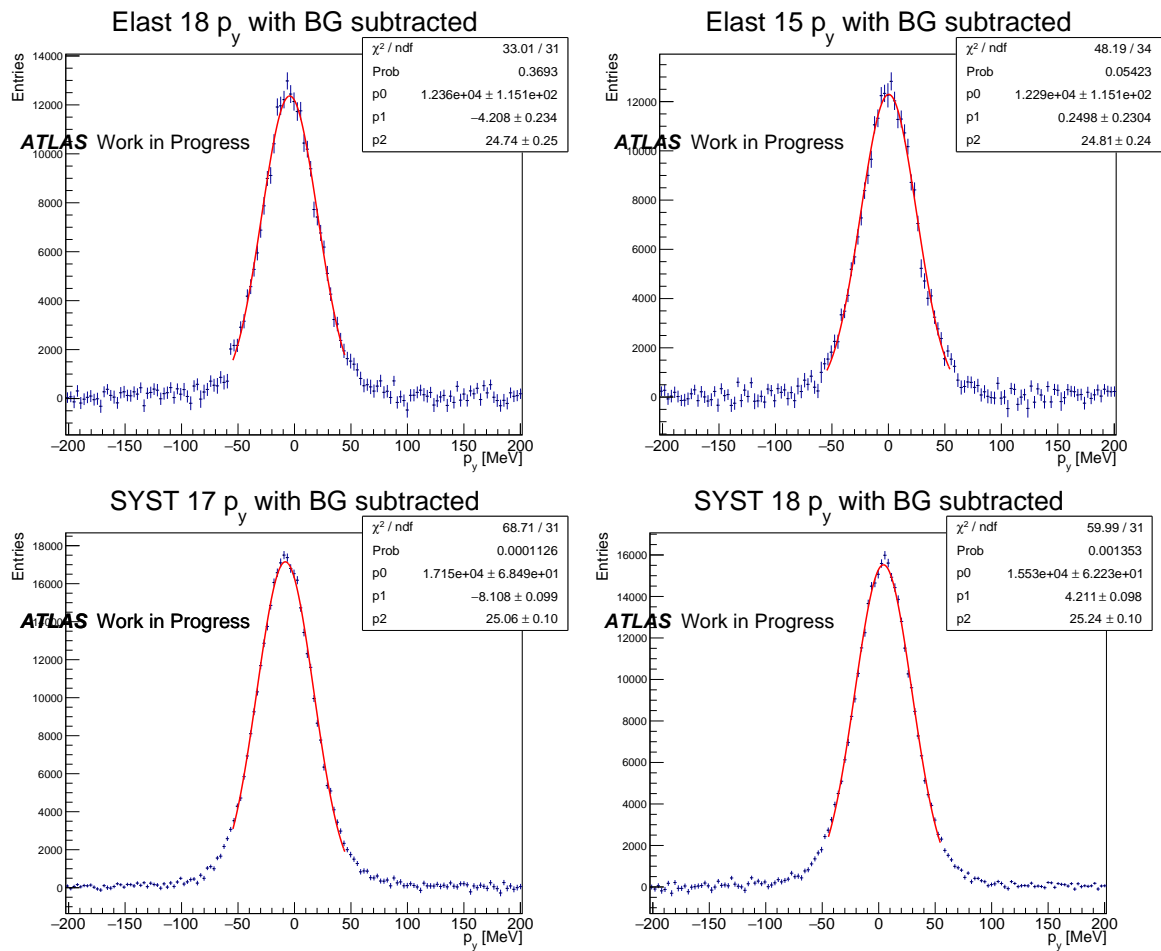


Figure 22: The total y -momentum of the four different arms.

y -momentum precise. The uncertainty is around 0.5MeV. Therefore the Inner Detector uncertainty is dominating in the p_y channel, and it is of magnitude $\sigma_{p_y} \approx 25\text{MeV}$. Since it can safely be assumed that the uncertainty from Inner Detector is the same in x and y regardless of which arm the protons hit, it can be seen that the uncertainty on the proton momentum is dominating in x . The difference in the x -momentum across the arms is not well understood at the moment. It is most likely some problem with the optics. Since this is not completely understood the uncertainty on the total system x -momentum that will be used throughout the thesis is $\sigma_{p_x} = 80\text{MeV}$ and $\sigma_{p_y} = 25\text{MeV}$

Background Analysis

The used cut criteria are very strict, and hence the background is relatively low. The main background sources are from other central diffractive processes. For instance it is quite likely that only two pions are observed in central exclusive four pion production, and this process would meet the cut criteria. Most inelastic processes are removed by the MBTS vetoes and the requirement of only two tracks in the central region. Furthermore they require some random coincidence with an elastic event or random beam halo particles on both the A-side and the C-side at once to get included in the signal sample.

The background is found using the basic concepts of charge conservation and momentum conservation. Firstly a background template is constructed by looking at events that match all the cut criteria, but where the two particles seen in Inner Detector have the same charge. This cannot be signal, and its shape is assumed to be representative of the background. Using momentum conservation, the background template can be normalized to the data. A signal region in (p_x, p_y) space centered around $(0, 0)$ is defined as can be seen on Figure 24. Everything outside of this region is regarded as background. The background template is then scaled such that it matches the events with missing momentum that otherwise pass all cut criteria. On Figure 23 the p_x and p_y distribution of the total particle system has been plotted separately with the background template scaled to the sidebands.

Different methods can be used to scale the template. They yield slightly different results, which reveals imperfections in the template fit. There are several reasons for this. There are statistical limitations on the same sign charge template, which has to be scaled up by around a factor of 5 to match data. There are also background processes, which are not included in a same sign template, in particular $pp \rightarrow p + \pi^+ \pi^- \pi^0 + p$. Since the neutral pion goes undetected, only two pions with opposite charge are measured. In this specific process, there will only be one missing particle. The same sign template is dominated by processes that have two or more missing particles. Therefore, it may not accurately describe the kinematical properties of the $\pi^+ \pi^- \pi^0$ final state.

Scaling Method 1.

The background template is normalized to the data using a histogram to histogram χ^2 fit. Due to imperfect alignment, the momentum distributions for each arm are slightly shifted, and since there are also different rates of background in each of the four arms, the templates are fitted to each arm independently. In this scaling method only the sidebands are compared, which corresponds to the events that are 5σ away from balanced momentum. The p_x and p_y distributions are scaled simultaneously.

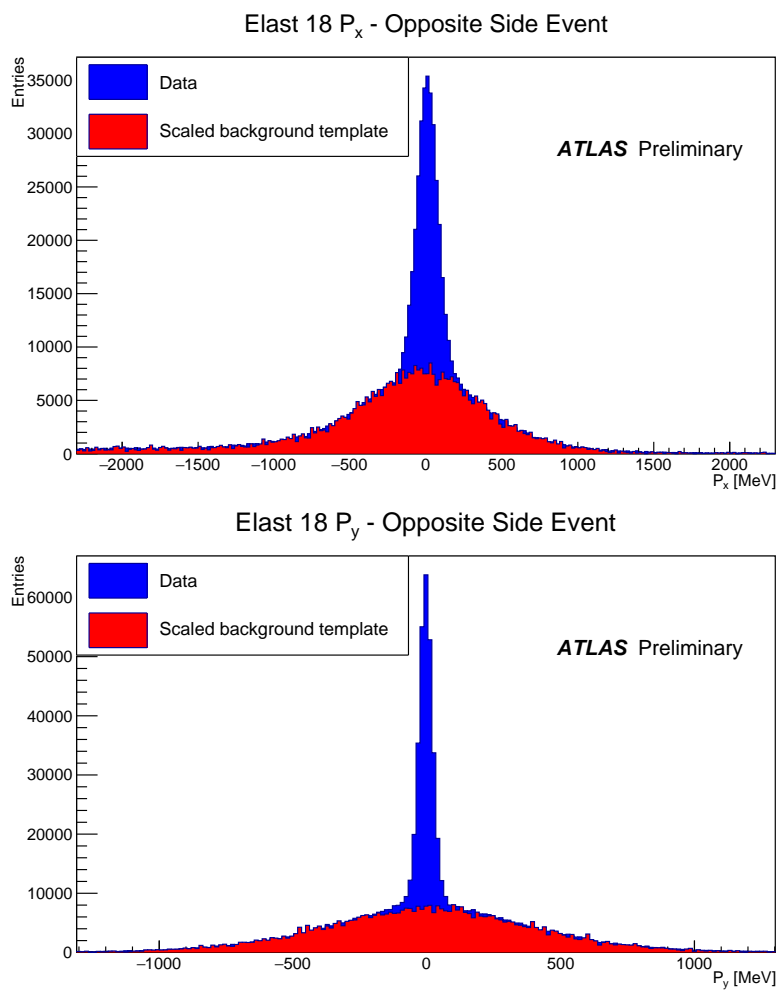


Figure 23: The background template is scaled using a χ^2 fit of the template in both the p_x and p_y projection simultaneously.

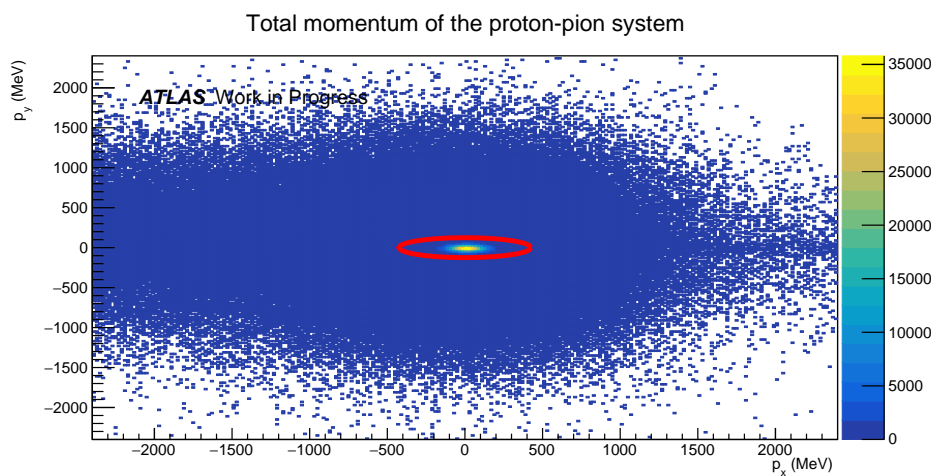


Figure 24: The signal region is depicted with the red ellipsis. The events outside the red ellipsis are used to scale the background templates.

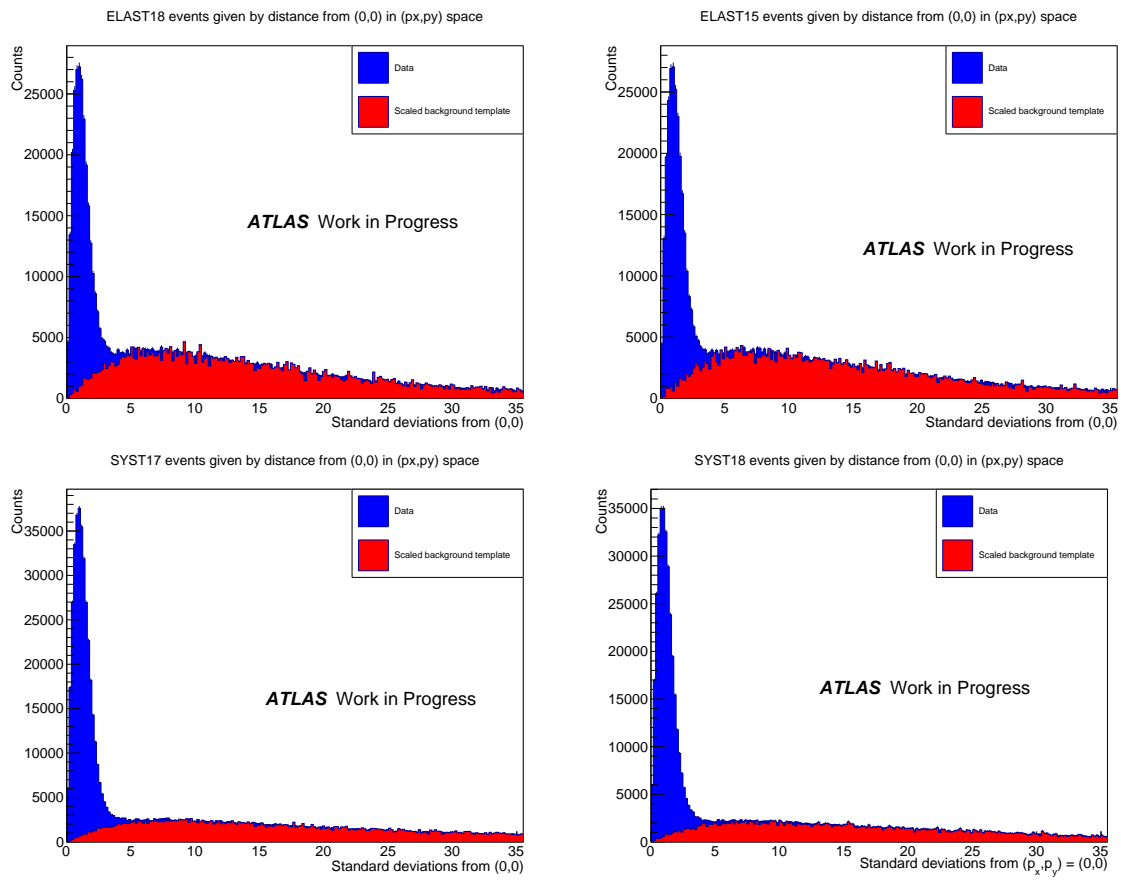


Figure 25: The background as represented in terms of standard deviations from $(p_x, p_y) = (0,0)$.

Arm	Scaling Factor (5σ)	Error	χ^2/ndf
ELAST18	5.64	± 0.05	1.17
ELAST15	5.61	± 0.05	1.16
SYST17	5.41	± 0.02	2.68
SYST18	5.31	± 0.02	2.20

Table 5: The scaling factors for the background template, when fitting the template to the data with missing momentum beyond 5σ

Here the uncertainties represents the fit uncertainties. To test the background template, the sidebands can be define as every event beyond 7.5σ . The scaling factors are here seen to change slightly.

Arm	Scaling Factor (7.5σ)	Error	χ^2/ndf
ELAST18	5.57	± 0.05	1.14
ELAST15	5.59	± 0.05	1.14
SYST17	5.36	± 0.02	2.64
SYST18	5.23	± 0.04	2.12

Table 6: Scaling factors for the background template, when fitting the template to the data with missing momentum beyond 7.5σ

Finally when scaling to the events which are beyond 10σ , different scaling factors are obtained.

Arm	Scaling Factor (10σ)	Error	χ^2/ndf
ELAST18	5.52	± 0.06	1.17
ELAST15	5.54	± 0.06	1.15
SYST17	5.34	± 0.03	2.74
SYST18	5.18	± 0.04	2.15

Table 7: Scaling factors for the background template, when fitting the template to data with missing momentum beyond 10σ

Clearly the scaling factor should be the same regardless of whether you scale from 5, 7.5 or 10σ as long as no more signal is present. This either means that there is signal beyond a 5σ cut, or that the background template does not fit data perfectly.

Scaling Method 2.

The same procedure is used as in Method 1, but rather than only scaling to sidebands, the full momentum range is fitted, and signal is represented with a Gaussian distribution. So the p_x and the p_y distribution are fitted simultaneously with both a Gaussian and background template. Another term is added to the χ^2 function, where it is required that the amount of signal events in a given arm in the y -distribution should be approximately the same as in the x -distribution.

Arm	Scaling Factor	Error	χ^2/ndf
ELAST18	5.71	± 0.04	1.19
ELAST15	5.70	± 0.04	1.17
SYST17	5.58	± 0.03	2.28
SYST18	5.50	± 0.03	1.96

Table 8: Scaling factors for the background template, when fitting the background template and a Gaussian distribution simultaneously to the full data sample in momentum space.

It is not known if signal is perfectly described by a Gaussian, but it is very likely. Background is definitely not described by a Gaussian in the p_x distribution, since protons with energy loss appear to have negative p_x , creating an asymmetry.

Scaling Method 3.

The total amount of events outside the signal region in the background template, is normalized to match the total amount of events outside the signal region in data. The outer most regions of the momentum distributions have very limited statistics in the same signal background. The bins where there are less than 10 background events, are therefore excluded. This scaling method should essentially be the same as Method 1, except here the template shape is not considered.

Arm	Scaling Factor (5σ)	Error
ELAST18	5.60	± 0.02
ELAST15	5.63	± 0.02
SYST17	5.54	± 0.02
SYST18	5.45	± 0.02

Table 9: Scaling factors for the background template, when normalizing the template to data with missing momentum beyond 5σ

Here the results are slightly different to Method 1. The template is scaled again with an increased signal region.

Arm	Scaling Factor (7.5σ)	Error
ELAST18	5.55	± 0.03
ELAST15	5.58	± 0.03
SYST17	5.50	± 0.03
SYST18	5.40	± 0.03

Table 10: Scaling factors for the background template, when normalizing the template to data with missing momentum beyond 7.5σ

Similarly to Scaling Method 1, the scaling factor decrease when increasing the signal region. Finally with the 10σ region, the obtained scaling become:

Arm	Scaling Factor (10σ)	Error
ELAST18	5.44	± 0.03
ELAST15	5.53	± 0.03
SYST17	5.46	± 0.03
SYST18	5.29	± 0.03

Table 11: Scaling factors for the background template, when normalizing the template to data with missing momentum beyond 10σ

While Scaling Method 3 yields very similar results to Scaling Method 1, it shows that the scaling factor is affected by the choice of signal region.

Choice of Signal Region

When choosing to scale the background template using the events that are more than 5σ away from balanced momentum, then the basic assumption is, that there are no more signal events outside the 5σ region. A cut at 5σ can then be implemented safely when determining the cross section. However if a cut at 7.5σ is made, then the template should be scaled using events that are further away than 7.5σ from balanced momentum. Scaling Method 2 does however give the same scaling factors for all signal region choices. It does however rest on the assumption that signal can be described as a Gaussian.

The cross section, when using the different scaling methods and signal regions can be seen in Table 12.

Scaling Method	Cross Section (5σ) [μb]	Cross Section (7.5σ) [μb]	Cross Section (10σ) [μb]
1	18.81	19.15	19.39
2	18.75	18.98	19.08
3	18.79	19.09	19.35

Table 12: The cross section using different background subtraction schemes. The method for calculating the cross section is found in a later section.

When defining a 5σ signal region, the different scaling methods are close to equivalent. This is because the signal to background ratio in the 5σ region is high. Here there is around 15% background. The scaling methods are also quite similar. When extending the signal region the overall cross section increases, and the different methods yield different results. Assuming the background template is perfect, this would imply that there is still signal 10σ from balanced momentum. Further studies of these effect are difficult with Scaling Method 1 and 3, since the statistical uncertainty on the background scaling becomes worse as the signal region is increased. However Scaling Method 2 can be used for any signal region defined.

On Figure 26 the cross section found using the signal region defined by n has been plotted, where $n = \sqrt{\frac{p_x^2}{\sigma_x^2} + \frac{p_y^2}{\sigma_y^2}}$. As can be seen the cross section increases up to $n = 12$, where after it drops for larger n . This seems to indicate that there is either an excess of background in the far tail, or that there is an excess of background in the $5 < n < 15$ region.

Using Scaling Method 2, the fraction of expected background events can be calculated for different momentum regions. So in a given region what is $\frac{B}{N}$, where B is the number of background events, and N is the total measured events.

Region	0σ to 1σ	1σ to 2σ	2σ to 3σ	3σ to 4σ	4σ to 5σ	5σ to 10σ	10σ to 15σ	15σ to 30σ
$\frac{B}{N}$	2%	5%	26%	61%	89%	92%	100%	105%

Table 13: The background to signal ratio in different regions of momentum space.

As can be seen from Table 13, there is more expected background than measured events in the outer regions.

Since the process $pp \rightarrow p + \pi^+ \pi^- \pi^0 + p$ is not accounted for in the background template, it could be responsible for this effect. As argued earlier it is very likely that this process would have less missing momentum on average than background from four pion production

Cross section calculated for different signal regions using BG scaling method 2

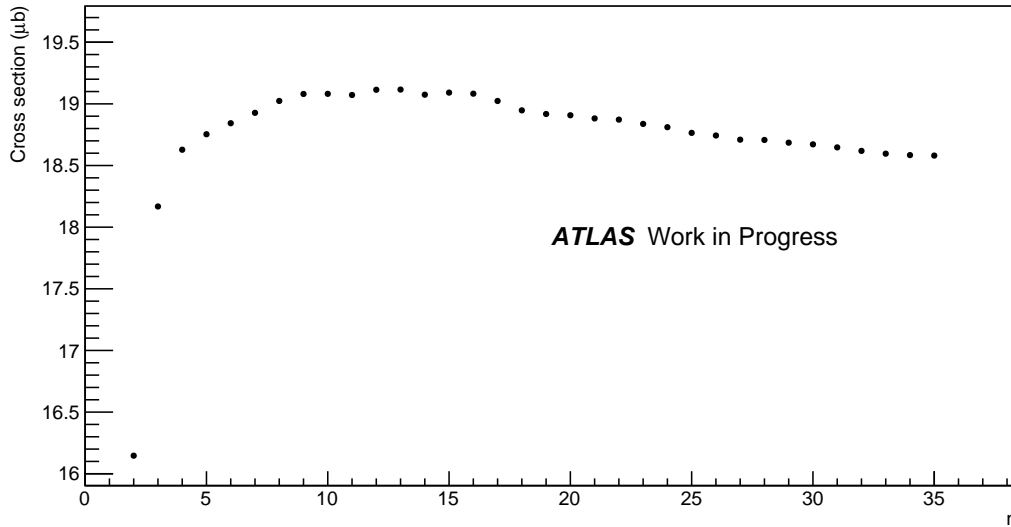


Figure 26: The cross section calculated with different choices of signal region. For the value

$$n = 30, \text{ a signal region of } n = \sqrt{\frac{p_x^2}{\sigma_x^2} + \frac{p_y^2}{\sigma_y^2}} < 30 \text{ has been chosen.}$$

or six pion production. Therefore it may contribute predominantly in the $n < 10$ region. This would make the background template have a too low event count in the low n region. When the background template is then scaled to the data, it will overshoot at high n , and undershoot at low n . This also explains why the scaling factors get lower, when increasing the signal region.

This process can potentially be accounted for by creating a template using full detector Monte Carlo of $p + \pi^+\pi^-\pi^0 + p$, and then fitting this extra template on top of the same charge template. The overall effect is still quite small, since $\pi^+\pi^-\pi^0$ is mainly produced via the $\omega(782)$ and the $a_1(1260)$ resonances. These are both forbidden in DPE due to CP conservation.

Systematic Uncertainty from Background Subtraction

The background template is not perfect, and a systematic uncertainty to account for this needs to be assigned. Different choices of signal regions and scaling methods yield different results. The best choice for signal region is not clear here. A cut at 3σ would definitely be too strict. The increase in cross section up to the $n = 10$ mark is due to imperfections in the background. The signal region is defined as within 5σ . A more strict momentum cut could be made, but it has a high chance of cutting signal and contribute a systematic uncertainty in the efficiencies.

Certainly the most ambitious choice for the background subtraction uncertainty would be to take the standard deviation of the cross sections calculate using the different scaling methods with a 5σ signal region. However it is probably better to be more conservative. The most stable method for the background subtraction appears to be Scaling Method 2. Here the highest cross section is obtained at a 12σ signal region with a cross section of $19.11\mu\text{b}$. The lowest is gained from 35σ with $18.58\mu\text{b}$. Assuming this corresponds to $2\sigma_{\text{BG}}$, this gives an uncertainty of:

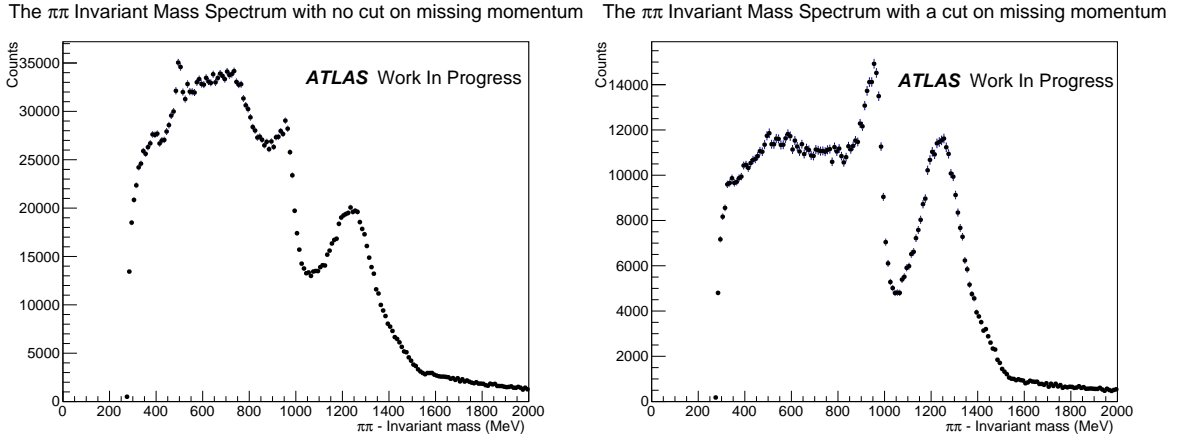


Figure 27: The dipion mass spectrum with and without a momentum cut. As can be seen the ρ - and K/\bar{K} -resonance is largely removed.

$$\sigma_{BG} = 0.265\mu\text{b}$$

Mass Spectrum Background

To improve signal to noise ratio on the physics distributions a cut on missing momentum of 2σ has been implemented. The physics distributions can then be scaled to match the full cross section. When doing a 2σ momentum cut, the expected signal ratio is $\frac{S}{S+B} = 0.96$. This can be seen quite clearly on Figure 27, where the ρ^0 meson is almost entirely removed, when the momentum cut is performed

The background inside the signal region needs to be removed. There are background resonance in the mass spectrum from the ρ^0 and K_s^0 . A background template constructed from same sign events cannot be used, since there are no resonances in the same charge spectrum. The total amount of background events in the signal region can however be determined using the same sign background template.

Two different methods, which can construct a background template have been developed. They both yield very similar results. The first is to use the mass spectrum of events, where there was missing traverse momentum. This mass spectrum is then scaled to match the total amount of expected background events in the signal region. This spectrum can be seen on Figure 28.

As can be seen in this spectrum the ρ^0 meson is very dominant, which is expected. Furthermore there is a clear K_s^0 resonance. Both of these resonances must be background, since the examined interaction is dominated by Double Pomeron exchange, which can only produce J even and $CP = ++$ states. There is also a shoulder in the low mass region. This may be the ϕ -meson decaying to a K^+K^- state. Since any track in the ATLAS Inner Detector is assumed to be a pion, the kaons get incorrectly tagged, and their energy is hugely underestimated, causing a shift in the invariant mass. The momentum of the kaons are correct, but since the ϕ -meson is $J = 1$, there were other particles produced and not detected, which results in missing momentum.

The second method is to guess that four pion central diffraction is the largest source

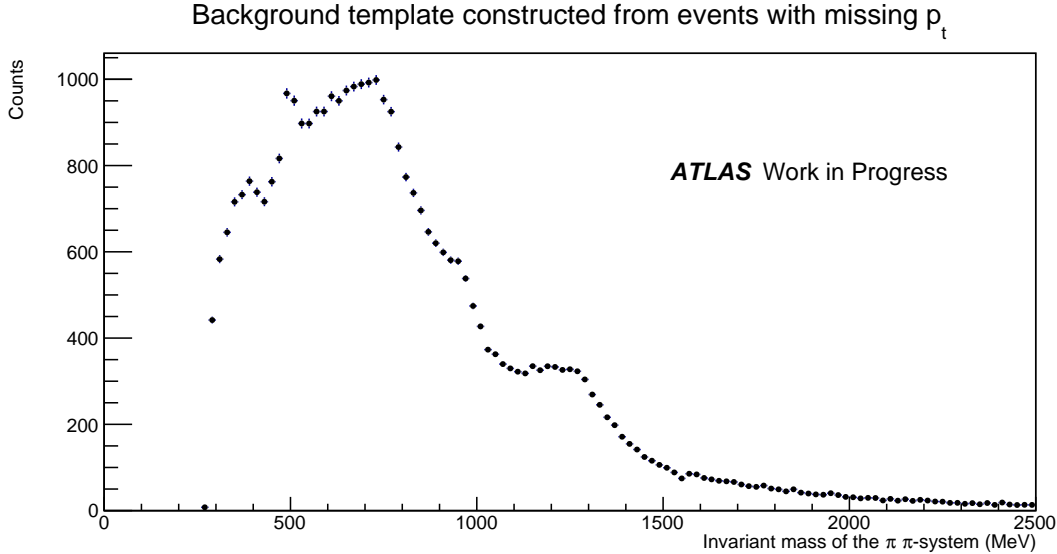


Figure 28: The mass spectrum of events with missing momentum. The overall background template has been scaled to match the amount of background events extrapolated using the same sign background template.

of background for dipion central diffraction. The template constructed with this method is plotted in Figure 29. This template has a more sharp ρ resonance, however there is no shoulder from the ϕ -meson. The $K\bar{K}$ resonance is not seen either due to the z_0 and d_0 tracking cuts. Its interesting that the missing momentum template has K/\bar{K} despite this cut.

The template constructed from events with missing transverse momentum are used for the main physics results, and the four pion template is used to estimate a systematic uncertainty on the mass spectrum shape. This is done by subtracting the two templates, and using the bin values in the subtracted histogram as the uncertainties.

Background from Wrong PID of Kaons

Background from central exclusive kaon production, $pp \rightarrow p + K^+K^- + p$ cannot be distinguished from dipion production using the method of momentum conservation, since all final state particles are detected in central exclusive kaon production, and because the momentum of the kaons are measured correctly. The energy of the kaon is hugely underestimated since it is by default tagged as a pion. This causes a huge shift in the invariant mass of the event. For further studies it could be interesting to use the pixel detector to study $\frac{dE}{dx}$ of tracks. This would potentially enable tagging of kaons.

An estimate of the $pp \rightarrow p + K^+K^- + p$ cross section is taken from previous measurements and added as an uncertainty. Due to lack of measurements, it is necessary to compare with results that have completely different kinematics than this data. The Omega experiment made measurements of both pions and kaons. While they never reported a cross section, the rate of events can be compared. Comparing different channels in the results from the WA102 experiment [13][14], it looks like the branching ratio between kaons and pions are of the order $\frac{\sigma(K^+K^-)}{\sigma(K^+K^-)+\sigma(\pi^+\pi^-)} = 0.01$. No attempt at subtracting kaons have been made.

Background template constructed from events with four pions

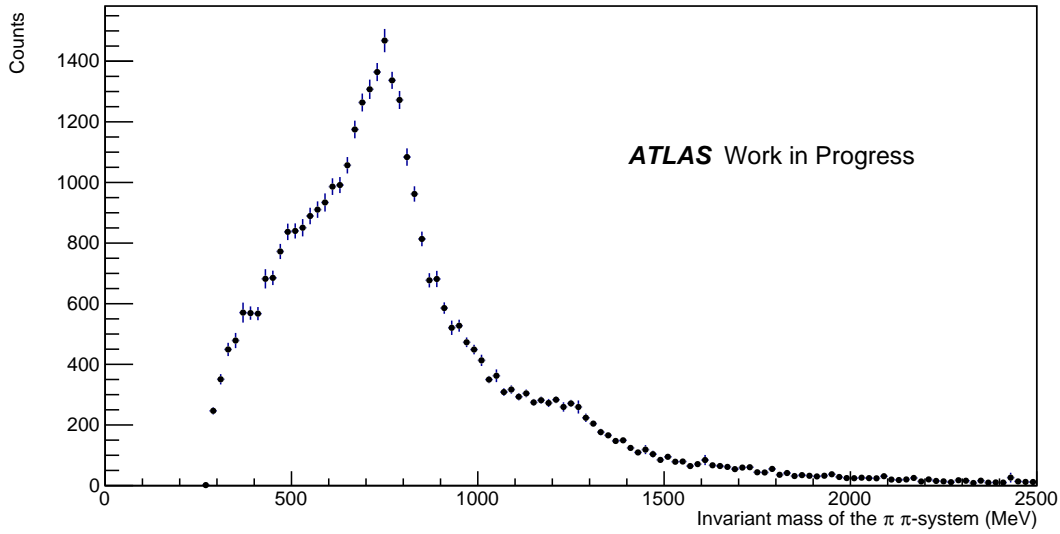


Figure 29: The mass spectrum from two pions in a four pion event. The overall background template has been scaled to match the amount of background events extrapolated using the same sign background template.

Back to Back Cut

When calculating some of the detector efficiencies in the next chapter, there are missing tracks in ALFA, which means that a cut on missing momentum cannot be performed. This is for instance the case, when finding the ALFA track reconstruction efficiency. Another cut to discriminate between background and signal is needed. The local angle in x between the inner and outer detector $\theta_x = \frac{x_{245} - x_{237}}{8.0m}$ can be plotted against x_{237} . As can be seen on Figure 30, these variables are quite sensitive to background. On the left hand side events are plotted, which include both central diffraction and background. On the right hand side a plot with a much cleaner central diffractive sample is shown. This has been obtained by doing a strict 2σ momentum cut. An ellipsis is fitted to this sample, and it is now possible to cut events, which are outside of this ellipsis, when it is not possible to reconstruct the full system momentum.

Partial Wave Analysis

A partial wave analysis has been performed in order to extract the spin matrices of the resonances. The Gottfried-Jackson reference frame is used. A Lorentz boost from the ATLAS frame to the center of mass frame of the two pion system is performed. This is also the rest frame of the resonance. The z -axis is then defined as the direction of the incoming Pomeron in this reference frame. The angle θ_{GJ} is then taken to be the angle between the incoming Pomeron and the positive pion.

Reconstructing the Pomeron Kinematics

The Pomeron kinematics are only partially known. The outgoing protons transverse momentum is measured, which gives the Pomerons transverse momentum, but the z -components are unknown. If the Pomerons are assumed to be on-shell, then using conservation of energy

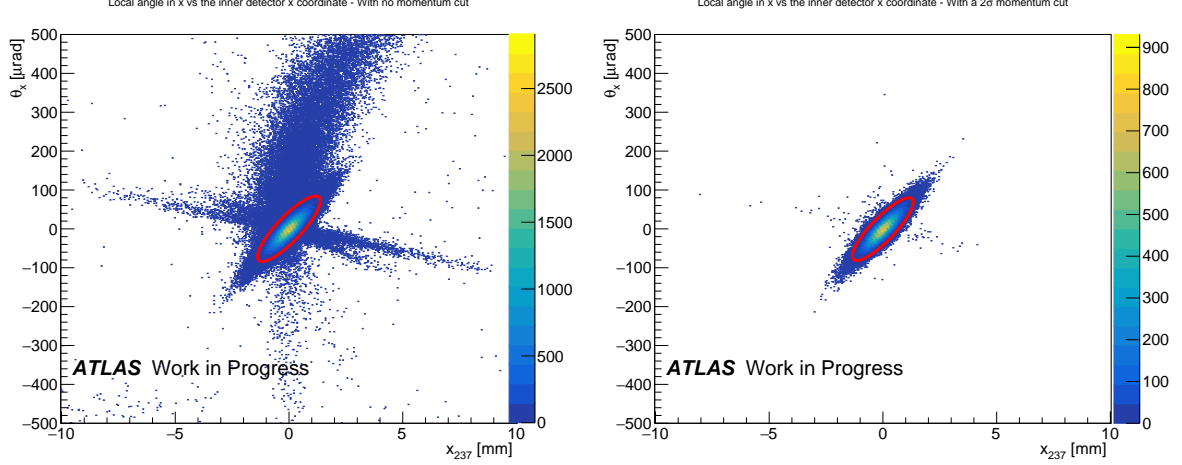


Figure 30: The local angle in x plotted versus the inner detector coordinate in x . On the left hand side there is background, and the right hand side is predominantly signal. An ellipsis is fitted to signal, and a 3σ contour is drawn in.

this relation is obtained:

$$\sqrt{p_{x,1}^2 + p_{y,1}^2 + p_{z,1}^2} + \sqrt{p_{x,2}^2 + p_{y,2}^2 + p_{z,2}^2} = E_{\pi\pi} \quad (31)$$

Here 1 and 2 indicate the two Pomerons. A second constraint on the z -momentum exists:

$$p_{z,1} + p_{z,2} = p_{z,\pi\pi}, \quad p_{z,1} > 0, \quad p_{z,2} < 0 \quad (32)$$

With this the momentum z -component can be reconstructed. This is done by minimizing the function (33) with MINUIT.

$$\chi^2 = \left(\frac{p_{z,\mathbb{P}\mathbb{P}} - p_{z,\pi\pi}}{\sigma_z} \right)^2 + \left(\frac{E_{\mathbb{P}\mathbb{P}} - E_{\pi\pi}}{\sigma_E} \right)^2 + \sum_{n=\text{protons}} \left(\frac{p_{x,\mathbb{P},n} - p_{x,n}}{\sigma_x} \right)^2 + \left(\frac{p_{y,\mathbb{P},n} - p_{y,n}}{\sigma_y} \right)^2 \quad (33)$$

The free parameters are the Pomerons p_x , p_y and p_z which also dictates the Pomeron energy. The x and y components are free parameters to account for the fact that proton kinematics are approximated. $\sigma_x = 80\text{MeV}$ and $\sigma_y = 1\text{MeV}$ are the uncertainties used for the proton momentum. The uncertainties used for the pions are $\sigma_z = 25\text{MeV}$ and $\sigma_E = 200\text{MeV}$. Some events reconstruct poorly and therefore a cut requiring $\chi^2 < 1000$ was implemented.

Extraction of Spin Density Matrix Elements

With the Pomeron kinematics a z -axis is well defined, which can be used to measure the angular distribution as a function of the invariant mass.

The idea is then to fit the formula $A(\cos\theta)$ to each of the mass bins. The bins have a width of 40 MeV.

$$A(\cos\theta) = \frac{N}{2} \cdot [\rho^{\text{SS}} + 2\sqrt{4\pi}\rho^{\text{SD}}Y_0^2(\cos\theta) + 4\pi\rho^{\text{DD}}[Y_0^2(\cos\theta)]^2] \quad (34)$$

There are further constraints on the density matrix elements.

$$0 \leq \rho^{\text{SS}} \leq 1, \quad \rho^{\text{SS}} + \rho^{\text{DD}} = 1, \quad |\rho^{\text{SD}}|^2 \leq |\rho^{\text{SS}}||\rho^{\text{DD}}| \quad (35)$$

This is done in analogy to an earlier study at the ISR[17]. The different spin matrices can be seen on Figure 32, 33 and 34. These distributions have not been acceptance corrected, and it is not known what effects that will have.

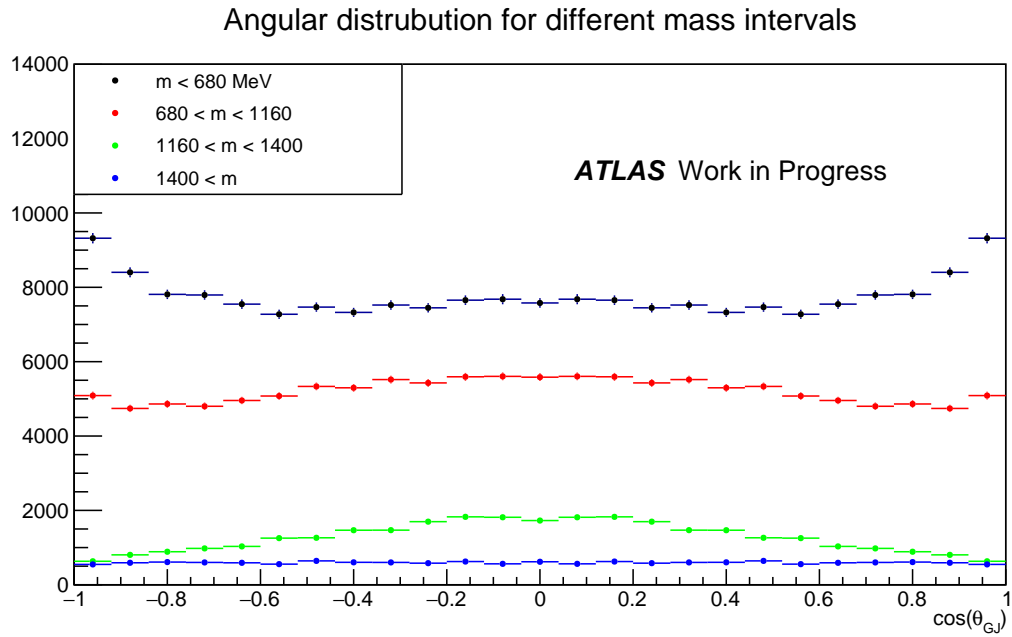


Figure 31: Here the angular distribution of the pions are shown for different invariant masses.

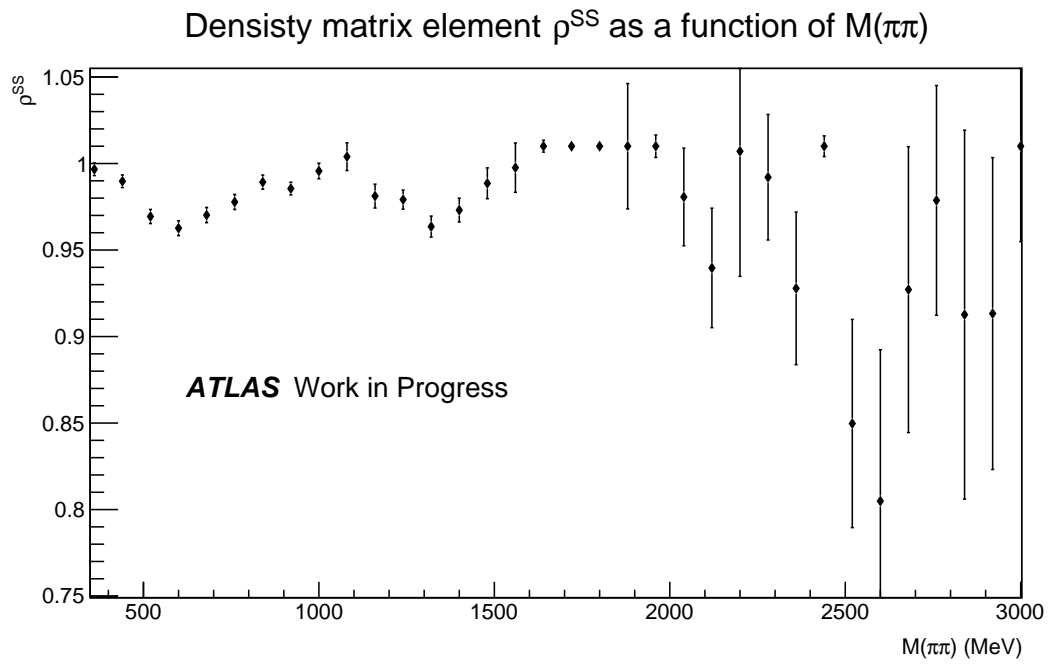


Figure 32: The S-wave density matrix element as a function of the invariant mass.

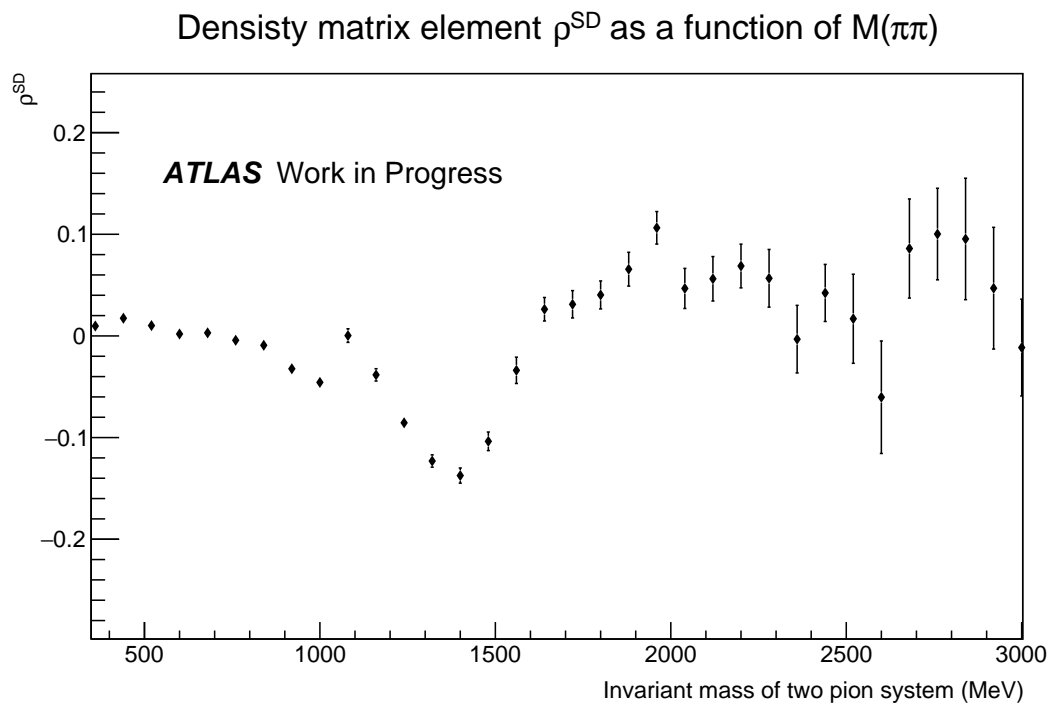


Figure 33: The SD density matrix element as a function of the invariant mass.

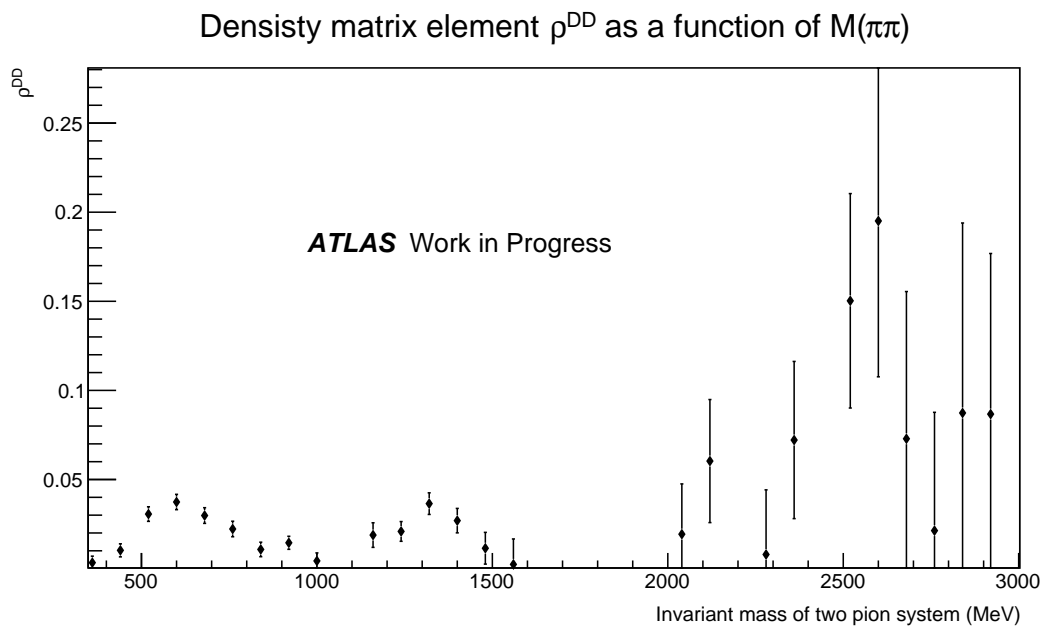


Figure 34: The DD density matrix element as a function of the invariant mass.

Four Pion Analysis

The process $pp \rightarrow p + \pi^+ \pi^- \pi^+ \pi^- + p$ has also been studied. The biggest difference is that the track criteria of $d_0 < 1.5\text{mm}$ and $z_0 \times \sin(\theta) < 1.5\text{mm}$ are changed to $d_0 < 5\text{mm}$ and $z_0 \times \sin(\theta) < 5\text{mm}$. This is done to avoid removing the physics process $\mathbb{P}\mathbb{P} \rightarrow K\bar{K} \rightarrow \pi^+ \pi^- \pi^+ \pi^-$, that otherwise might get cut due to the long lifetime of the neutral kaon.

The background analysis is done using the same approach as the two pion analysis.

Background Analysis

Scaling Method 2 is used to find the background normalization factors. They can be seen in Table 14.

Arm	Scaling Factor	Error	χ^2/ndf
ELAST18	3.24	± 0.04	1.26
ELAST15	3.32	± 0.04	1.11
SYST17	3.53	± 0.04	1.38
SYST18	3.58	± 0.04	1.25

Table 14: The background scaling factors determined using Scaling Method 2 for events with four pions.

The signal region is varied to see, how the cross section is affected as seen on Figure 35. The uncertainties on the total momentum distribution is determined in the same manner as for two pions, and it is found to be $\sigma_{p_x,4\pi} \approx 1.25\sigma_{p_x,2\pi}$ and $\sigma_{p_y,4\pi} \approx 1.25\sigma_{p_y,2\pi}$.

The maximum cross section is seen to be at $n = 14$ with a value of $3.904\mu\text{b}$. The cross section falls for higher values of n , to a minimum at $n = 28$ with a value of $3.272\mu\text{b}$. The value $n = 6$ is chosen for the cross section and the difference between the signal region of $n = 29$ and $n = 14$ is chosen as a $2\sigma_{\text{BG},4\pi}$ systematic uncertainty from the background subtraction.

$$\sigma_{\text{BG},4\pi} = 0.316\mu\text{b}$$

The background template for the four pion mass spectrum is made from events with missing momentum, and it can be seen on Figure 36. No systematic uncertainty from the mass spectrum background shape has been determined for the four pion mass spectrum.

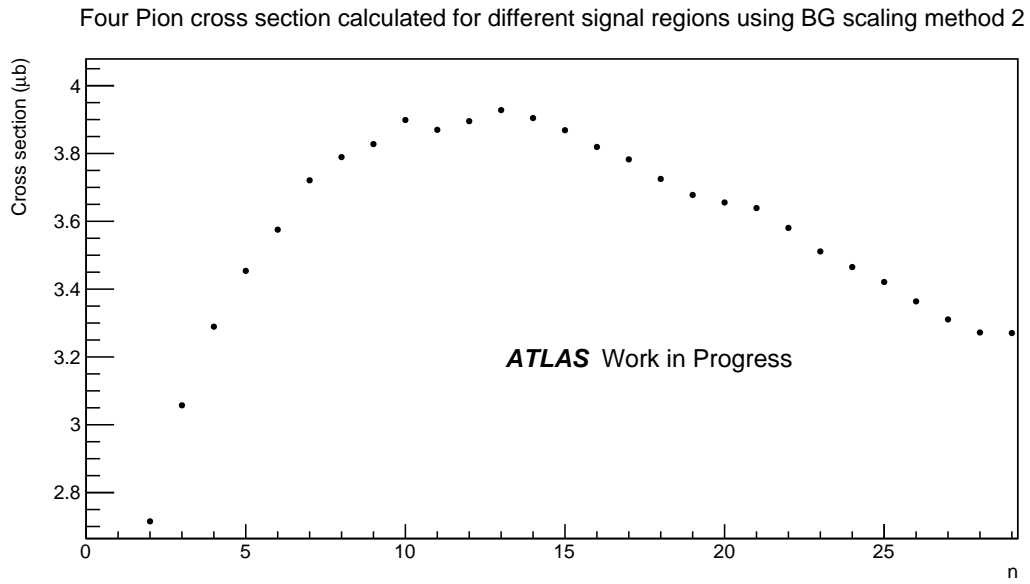


Figure 35: Similar to Figure 26 but now with four pions. A maximum is seen at a signal region of $n = 14$.

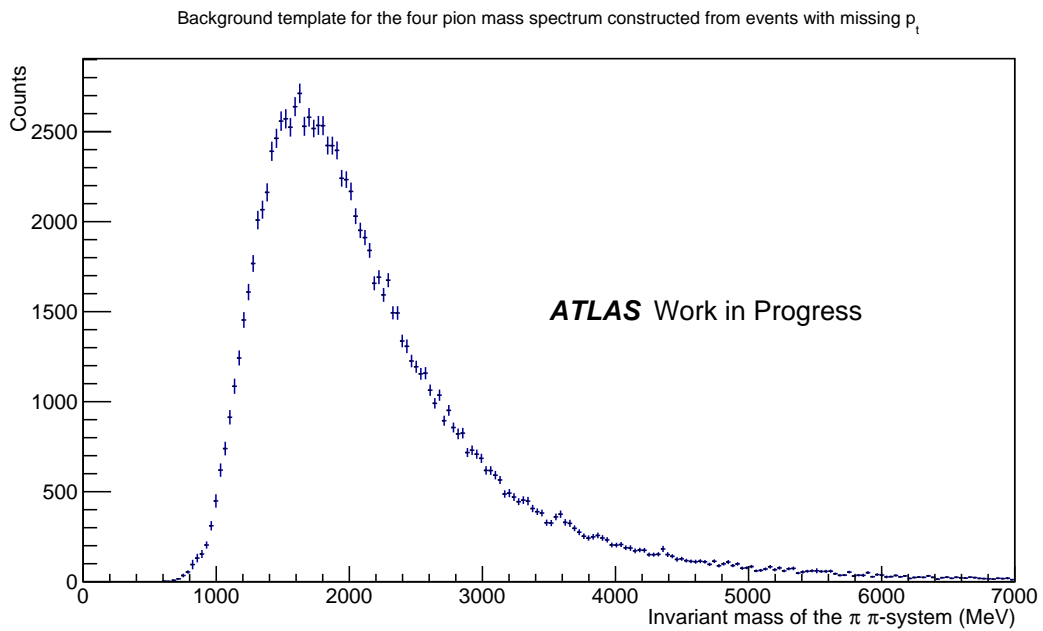


Figure 36: The mass spectrum of events with missing momentum. The overall background template has been scaled to match the amount of background events extrapolated using the same sign background template.

Acceptance and Efficiencies

In this chapter the different efficiencies and acceptances that have been determined for the diffractive runs, which this thesis is based on, are presented. Since the process being studied is $pp \rightarrow p + \pi^+ \pi^- + p$, the most important efficiencies are the pion detection efficiency in the Inner Detector, and the proton detection efficiency in the ALFA detector.

The ALFA efficiencies are identical for the two and four pion analysis. Some of the Inner Detector efficiencies are expected to be different.

ALFA Acceptance

The ATLAS Inner Detector spans $-2.5 < \eta < 2.5$, and can only detect pions that have $p_t > 100\text{MeV}$. Therefore a fiducial volume is chosen for the pions, since it is relatively easy to extend this kinematical region to the full phase space. It is, however, important to account for the proton acceptance in ALFA. In essence the fraction of central exclusive $pp \rightarrow p + \pi\pi + p$ with two pions in the fiducial volume, where both protons hit ALFA in two pots, needs to be determined.

A simple kinematical region cannot be given for the protons due to the complex magnet configurations, and because the protons can hit the beam screen, beam pipe etc. To account for the proton acceptance a fast simulation of ALFA is used. This simulation has been developed by Alexander Lind, and a detailed description can be found in his thesis[37]. In short, a parametrization of the protons position as it moves down the beam pipe was developed using a single particle gun simulation, and the TWISS files, which contains all the magnet information for the runs. This parametrization depends on the protons momentum, energy loss and position at the interaction point. A detector simulation was implemented, which tracks if the proton hits the LHC beam screen or if it hits the beam pipe. If the proton hits ALFA a Gaussian smear is applied to account for the detector resolution. The simulation does not include potential proton interactions with detector material. Using this framework, the acceptance was then calculated using PYTHIA8 [46]. Central diffractive events, where all pions were in the pion fiducial volume, were generated, and the protons were transported to the ALFA stations. It was checked, whether or not the protons hit the detector. The acceptance is then calculated as:

$$A = \frac{N_{\text{ALFA}}}{N}, \quad |\eta_\pi| < 2.5, \quad p_{t,\pi} > 100\text{MeV} \quad (36)$$

The PYTHIA8 simulation of central diffraction lacks the low mass central diffraction resonances and therefore the developers have put in a 1GeV invariant mass cutoff for the central product. PYTHIA can however be modified to simulate the low mass region. Assuming that the proton acceptance is mainly affected by kinematics, there should not be any problem.

Beam Spot and Beam Divergence

The simulation needs to account for the vertex and beam spread, which can be found from the emittance. The emittances were measured during the data collection with wire scans. They were found to be:

$$\epsilon_{xA} = 3.6 \pm 0.4 \mu\text{m} \cdot \text{rad}$$

$$\epsilon_{yA} = 3.5 \pm 0.4 \mu\text{m} \cdot \text{rad}$$

$$\epsilon_{xB} = 3.9 \pm 0.4 \mu\text{m} \cdot \text{rad}$$

$$\epsilon_{yB} = 3.4 \pm 0.3 \mu\text{m} \cdot \text{rad}$$

The transverse momentum spread of the beam can then be calculated from the emittance.

$$\sigma_{A_{p_x}} = \sqrt{\frac{\epsilon_{xA}}{\gamma\beta^*}} \cdot E_A$$

The vertex spread is also calculated.

$$\sigma_{\text{vertex}} = \frac{\sqrt{\beta^*/\gamma}}{\sqrt{1/\epsilon^A + 1/\epsilon^B}}$$

The vertex spread can be seen in Table 15

	Vertex Spread [mm]	Error [mm]
σ_x	0.156	± 0.006
σ_y	0.150	± 0.005

Table 15: The vertex spread calculated from the beam emittance.

The beam spread can be seen in Table 16.

	Beam Spread [GeV]	Error [GeV]
σ_{Ax}	0.0156	± 0.0009
σ_{Ay}	0.0154	± 0.0009
σ_{Bx}	0.0163	± 0.0008
σ_{By}	0.0152	± 0.0007

Table 16: The momentum spread in x and y for the two beams

Model Dependence

The acceptance depends on what model is used for the Pomeron flux. The parameter ϵ has a large effect when you allow any final state, however it has a small effect on the acceptance of $pp \rightarrow p + \pi\pi + p$. Instead the parameter α' , the Pomeron flux trajectory, is important. Between the minimum value in PYTHIA of $\alpha' = 0.1\text{GeV}^{-2}$ and the maximum $\alpha' = 0.4\text{GeV}^{-2}$, the acceptance varies with around 6%. Different parametrizations of the Pomeron flux also exist, however they do not result in significantly different acceptances. The Donnachie-Landshof model with an $\alpha' = 0.126 \pm 0.013(\text{stat.}) \pm 0.012(\text{syst.})\text{GeV}^{-2}$ has been used. This value was found by the H1-collaboration[28], and seems to be in good agreement with this data, since the measured central diffractive t-spectrum has discriminating power on the α' parameter. The value used for the intercept is $\epsilon = 0.085$. The MBR model has also been tried for comparison to Donnachie-Landshof.

In order to facilitate the systematic variations required when determining the acceptance for the cross section, the average acceptance of all events from the Monte Carlo are used. Since the Monte Carlo physics distributions do not directly correspond to data, a wrong acceptance may potentially be obtained by averaging over all MC events rather than doing acceptance correction bin by bin. However, in this case these two approaches give the same result, which can be checked by comparing the overall MC average acceptance with the overall acceptance obtained when applying the bin to bin acceptance to the invariant mass distribution of the pions i.e. $\sum_{n=\text{bins}} \frac{M_n \cdot A_n}{M_n}$.

The average acceptance can be seen in Table 17. The uncertainty from α' is found by doing a simulation of $\pm 1\sigma$ from the H1 measurement. It is important to note that the uncertainties between the arms from α' are fully correlated. The systematic uncertainty from the beam spot and divergence was estimated by varying the measured values with $\pm 1\sigma$. The effect on the acceptance turns out to be below the statistical uncertainty of 0.05% and has thus been neglected.

<i>ARM</i>	Acceptance %	(stat.)%	α' %
ELAST 18	23.30	± 0.05	± 0.26
ELAST 15	22.19	± 0.05	± 0.06
SYST 17	19.41	± 0.05	± 0.13
SYST 18	19.33	± 0.05	± 0.32

Table 17: The acceptance of the protons in central exclusive $\pi\pi$ events, where both pions are in the fiducial volume defined by $|\eta_\pi| < 2.5$ and $p_{t,\pi} > 100\text{MeV}$. The model used is Donnachie-Landshof with $\alpha' = 0.126\text{GeV}^{-2}$

The acceptance has also been found using the MBR model for comparison. The values can be seen in Table 18. A systematic uncertainty could have been chosen by taking the difference between these two models. Instead the cross section is calculated using both and the reader can decide, which to use.

<i>ARM</i>	Acceptance %	(stat.)%
ELAST 18	22.83	± 0.05
ELAST 15	21.62	± 0.05
SYST 17	20.78	± 0.05
SYST 18	20.75	± 0.05

Table 18: The acceptance of the protons in central exclusive $\pi\pi$ events, where both pions are in the fiducial volume defined by $|\eta_\pi| < 2.5$ and $p_{t,\pi} > 100\text{MeV}$. The model used is MBR with $\alpha' = 0.126\text{GeV}^{-2}$

The four pion acceptance is also found using Donnachie-Landshoff, however the systematic variations from α' is assumed to be the same as in the two pion case. The values can be seen in Table 19.

<i>ARM</i>	Acceptance %	(stat.)%	α' %
ELAST 18	22.4	± 0.2	± 0.26
ELAST 15	21.4	± 0.2	± 0.06
SYST 17	20.6	± 0.2	± 0.13
SYST 18	22.2	± 0.2	± 0.32

Table 19: The acceptance of the protons in central exclusive $\pi\pi\pi\pi$ events, where all pions are in the fiducial volume defined by $|\eta_\pi| < 2.5$ and $p_{t,\pi} > 100\text{MeV}$. The model used is Donnachie-Landshof with $\alpha' = 0.126\text{GeV}^{-2}$

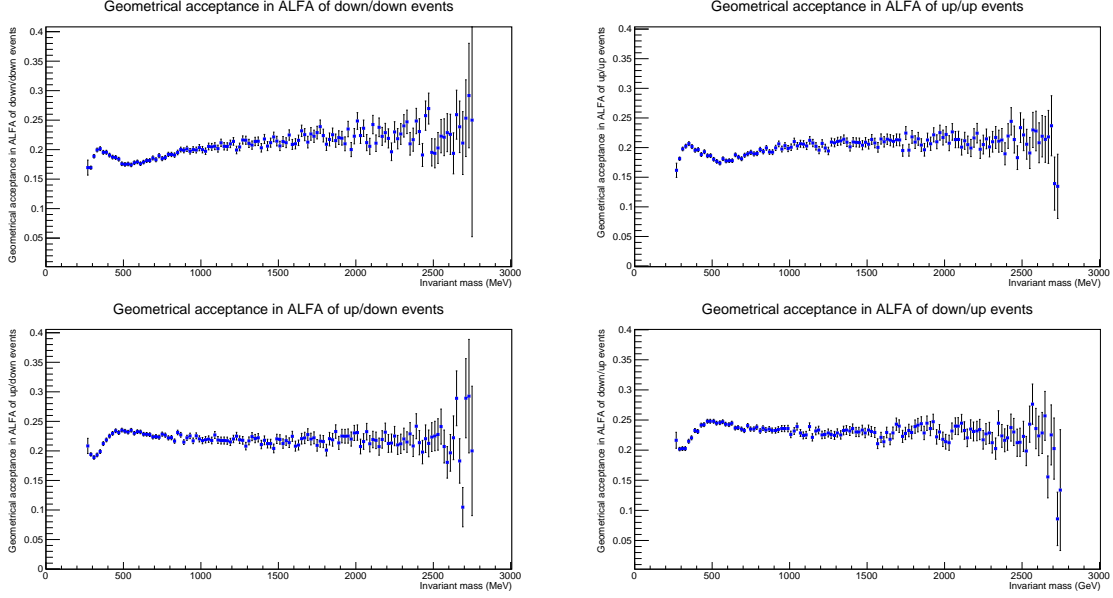


Figure 37: The proton acceptance for $pp \rightarrow p + \pi\pi + p$ events with pions in the fiducial volume $|\eta_\pi| < 2.5$, $p_{t,\pi} > 100\text{MeV}$. This is applied bin to bin to the two pion mass spectrum.

Mass Dependence

In Figure 37 the ALFA acceptance is shown as a function of the invariant mass of the central system. This is used to correct the dipion mass spectrum. The dependence was initially expected to be flat, but it is seen to fall at low invariant mass for the arms corresponding to ELAST15 and ELAST18, whereas it increase for SYST17 and SYST18. This is an effect of the fiducial volume of the pions. The acceptance of the full four particle system has also been found, and can be seen on Figure 38.

Next, in Figure 39, the four pion acceptance is shown, which is seen to be flat. Therefore the four pion mass spectrum is scaled with an overall scaling factor rather than corrected bin to bin.

t-Spectrum

The acceptance as a function of the proton t can be seen on Figure 40. Here the other proton is required to hit ALFA, and the pions are required to be in the fiducial volume. The acceptance of protons in the different detectors are shown, and they have been separated into the four different event classifications of central diffraction.

L1 Trigger Efficiencies

The four ALFA L1 triggers called L1_ELAST15, L1_ELAST18, L1_SYST17 and L1_SYST18, are used in this analysis. In front of each of the 8 Roman pots is a trigger tile, and each of these triggers are a combination of one trigger tile firing on each side. The exact trigger configurations are:

$$\text{L1_ELAST15} = (\text{POT}_1|\text{POT}_3)\&(\text{POT}_6|\text{POT}_8) \quad (37)$$

$$\text{L1_ELAST18} = (\text{POT}_2|\text{POT}_4)\&(\text{POT}_5|\text{POT}_7) \quad (38)$$

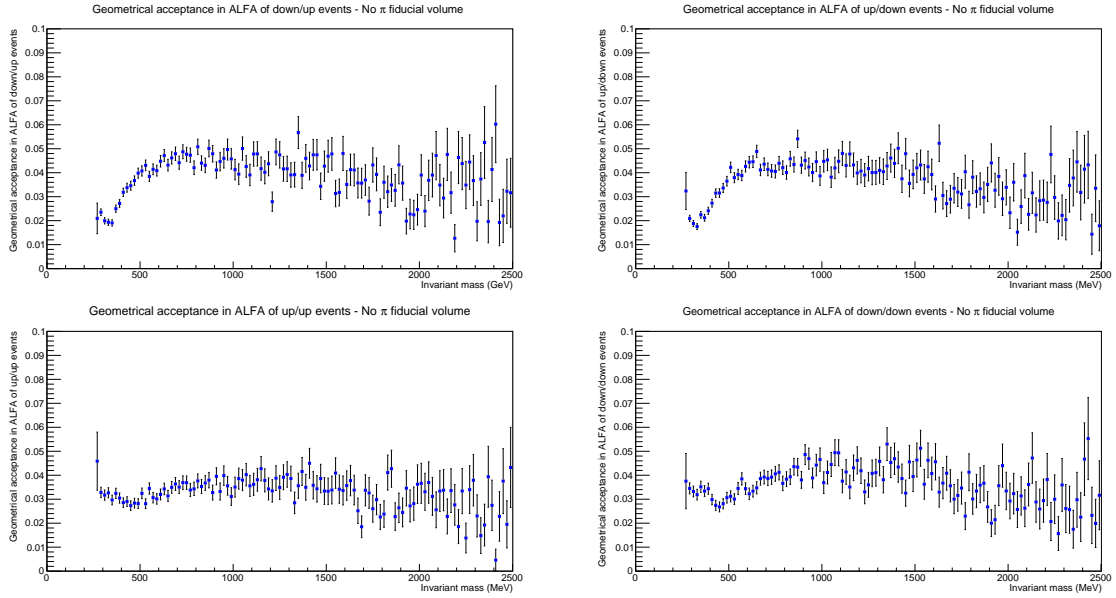


Figure 38: The acceptance of the entire particle system $pp \rightarrow p + \pi\pi + p$ as a function of invariant mass of the central dipion system. The low invariant mass acceptance drops sharply for the events with protons on opposite side of y .

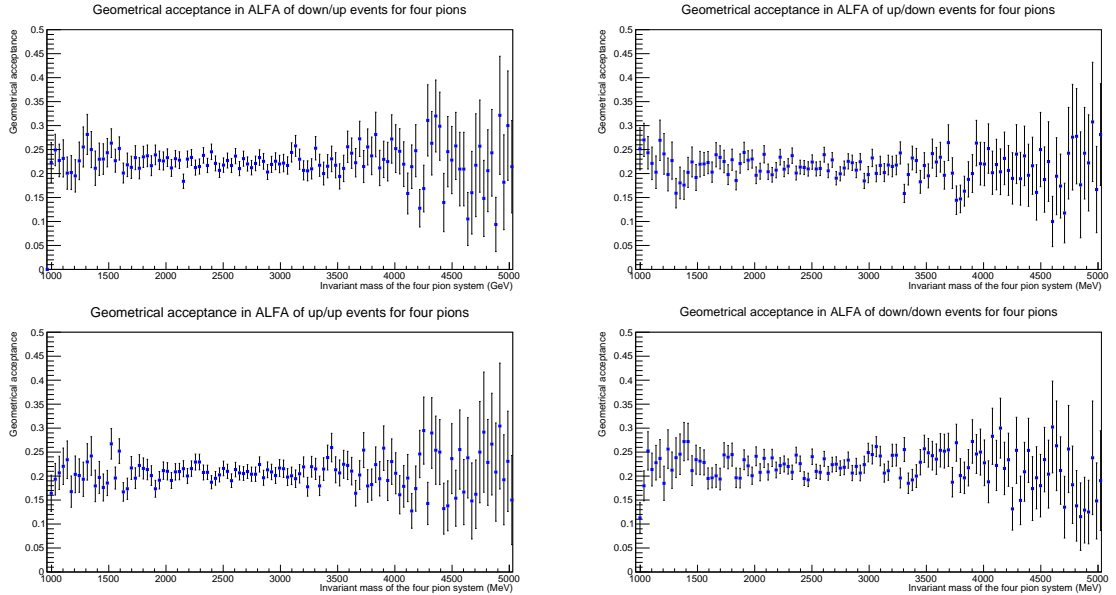


Figure 39: The proton acceptance for $pp \rightarrow p + 4\pi + p$ as a function of invariant mass of the central four pion system. This is seen to be more or less flat.

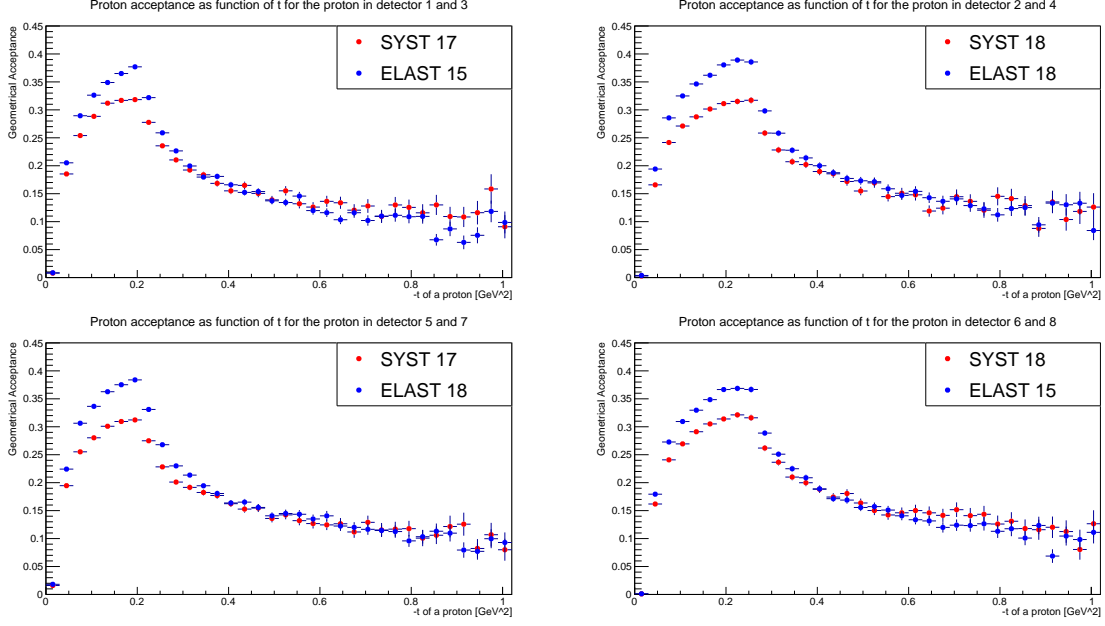


Figure 40: The proton acceptance for $pp \rightarrow p + \pi\pi + p$ events with pions in the fiducial volume $|\eta_\pi| < 2.5$, $p_{t,\pi} > 100\text{MeV}$, and the second proton hitting an ALFA station. There is a slightly different acceptance in the same pots depending on, what detector the other proton hit. This is an effect of the pion fiducial volume.

$$\text{L1_SYST17} = (\text{POT}_1|\text{POT}_3)\&(\text{POT}_5|\text{POT}_7) \quad (39)$$

$$\text{L1_SYST18} = (\text{POT}_2|\text{POT}_4)\&(\text{POT}_6|\text{POT}_8) \quad (40)$$

The trigger efficiencies for these have been determined using the ALFA calibration stream. In this stream, all ALFA information is output without a trigger saving it. The efficiency is found by going through events, and then performing a series of cuts to check, if a elastic event was in the detector. One track in each of the pots in a correct trigger configuration is required. Each of these reconstructed tracks must use at least 5 U-layers and 5 V-layers. Furthermore at least 3 U-layers and 3 V-layers cannot have more than 3 fiber hits. Finally a back to back cut is implemented. If the event passes all of these criteria, it is checked if the L1 trigger fired. If it did not fire, it is concluded that it is due to poor efficiency.

$$\epsilon_{\text{L1}} = \frac{N(\text{L1}\&\text{Cuts})}{N(\text{Cuts})}$$

Since elastic events are used here, the trigger efficiency is not found for L1_SYST17 and L1_SYST18. However since these triggers are just a different logic combination of the trigger pads used in L1_ELAST15 and L1_ELAST18, they are found by taking the average of these efficiencies. The loss from the L1 triggers is negligible. The determined efficiencies can be seen in Table 20.

Trigger Item	Efficiency %	Error%
ELAST 15	99.87	± 0.04
ELAST 18	99.88	± 0.04
SYST 17/SYST 18	99.88	± 0.03

Table 20: The trigger efficiency of the ALFA L1 trigger configurations. The trigger efficiency for L1_SYST17 and L1_SYST18 are taken to be the same.

HLT Efficiency

The high level trigger used in this analysis, is `HLT_mb_sptrk_vetombts2in_L1ALFA_CEP`. It uses a L1 input from the `L1_ELAST15`, `L1_ELAST18`, `L1_SYST17` and `L1_SYST18` triggers. Then a series of L2 Algorithms are run. First, the L2 Algorithm `T2MbtsFex`[27] is run. This determines, whether there is signal in the MBTS using an algorithm, which requires several MBTS tiles to be above a certain threshold. Then it vetoes if the inner MBTS tiles ($2.76 < |\eta| < 3.86$) show signal. Then the `L2MbSpFex` algorithm runs, which checks for clusters in Pixel and SCT, and it is decided whether or not the Event Filter algorithm should be run. The Event Filter algorithms, `EFMbTrkFex` and `EFMbTrkHypo`, reconstructs the event, which is saved, if there is at least one track with $p_t > 0.2\text{GeV}$ and $z_0 < 400\text{mm}$ [31].

The HLT efficiency is found by using the two no algorithm High Level Triggers named `HLT_noalg_L1ALFA_SYS` and `HLT_noalg_L1ALFA_Phys`. They take the L1 input from respectively `SYST17`, `SYST18` and `ELAST15`, `ELAST18` and then save the event without any further criteria. They cannot be used for the full analysis, since they are heavily prescaled. The analysis cuts are applied to the events saved by the no algorithm triggers. If the event passes all these, but the trigger `HLT_mb_sptrk_vetombts2in_L1ALFA_CEP` did not fire, it is concluded that it is due to HLT inefficiency, since events that pass all the analysis cuts are considered signal. The efficiency is then calculated as:

$$\epsilon_{\text{HLT_CEP}} = \frac{N(\text{HLT_CEP}\&\text{Cuts}\&\text{HLT_NoAlg})}{N(\text{HLT_NoAlg}\&\text{Cuts})}$$

Any inefficiency from the HLT will be associated with noise in the MBTS causing a signal event to be lost, that we have two tracks below $p_t < 0.2\text{GeV}$ or that there is some timing issue causing the event to not be saved. Outside of the HLT, no veto on MBTS activity is performed in the analysis. If a strict momentum cut is applied, it will minimize the probability that there are particles in the MBTS. The momentum cut is not a perfect discriminator between background and signal. For comparison the HLT efficiency is also found with two different offline MBTS vetoes.

The L1 trigger `L1_MBTS_1`, which vetoes if one of the MBTS trigger tiles is hit, has been tested. This trigger will veto if there is noise in the MBTS, so if this trigger is applied as an offline cut, the true HLT efficiency will not be determined, since the loss from MBTS noise will not be included.

Next the trigger `L1_MBTS_2` is tested, which vetoes if two tiles are activated. This trigger should not be affected by MBTS noise, however it does not veto every event with particles in the MBTS, since a particle do not necessarily hit two MBTS tiles.

Momentum cut	No MBTS Veto [%]	L1_MBTS_1 Veto [%]	L1_MBTS_2 Veto [%]
1σ	98.15 ± 0.32	99.64 ± 0.14	99.43 ± 0.18
2σ	96.86 ± 0.29	99.33 ± 0.14	99.03 ± 0.16
3σ	94.46 ± 0.34	98.98 ± 0.16	98.44 ± 0.19

Table 21: The high level trigger efficiency of `HLT_mb_sptrk_vetombts2in_L1ALFA_CEP` found using different methods.

As can be seen from Table 21, when applying no offline MBTS veto, the HLT efficiency falls as the momentum cut is made more lenient. This is, of course, expected since there is a much higher rate of background events in the 3σ sample and the chance that a particle in a

background event hits the MBTS is much higher. The value obtained with the L1_MBTS_1 veto is significantly higher, since it is certain that there are no particles in the MBTS. It is unexpected that the efficiency changes as the momentum cut is varied. This implies that there is a worse HLT efficiency for background than signal, when disregarding the MBTS veto. Since the HLT criteria from Inner Detector is extremely loose, it is not clear why this should be the case. Finally, efficiencies determined when vetoing on the MBTS_2 trigger is in between, which is expected. In the end the HLT efficiency is quite good.

The HLT efficiency determined using a veto on the MBTS_2 trigger, while applying a 2σ momentum cut has been chosen as the final value, since it provides a reasonable middle ground between accounting for MBTS noise, and the unknown dependence on missing momentum. A conservative 0.5% uncertainty was chosen, which seems to account for most of the reasonable possibilities.

$$\epsilon_{\text{HLT_CEP}} = 99.03 \pm 0.50\%$$

There may be some slight dependence on the HLT efficiency as a function of pion p_t , but the effects cannot be determined due to the very limited statistics of the "no algorithm" HLTs. There were 52 events that passed all cuts but where the HLT failed to fire. No statistically significant p_t or $M(\pi\pi)$ trend were seen among these events. Any p_t effects are most likely negligible, since the overall efficiency is so high.

The HLT efficiency is probably slightly higher in the four pion case, but it is guessed to be the same, since there is not enough statistics to calculate it.

Loss from L1 Veto

Events where two L1 ALFA triggers fire at the same time, are vetoed. This is done for a number of technical reasons. Firstly it avoids any ambiguity in the choice of what ALFA detectors correspond to a central diffractive pion vertex. If two ALFA triggers fire, there are at least two detector combinations, that can correspond to a central diffractive event observed in ATLAS. Secondly, it heavily simplifies finding the ALFA track reconstruction efficiency, since it removes almost all events, which triggered due to a proton shower, made by a proton hitting a collimator. However this veto will also cause a loss of true central diffractive events.

A central diffractive event will leave a track in four of the detectors, and it will activate at least two of trigger pads, one on each side of the interaction point. If this event happens simultaneously with a beam particle hitting one of the empty ALFA detectors, then two of the L1 ALFA triggers will fire. This veto would then cause a loss of the event. To account for this, the rate at which random particles hit ALFA have been found. This should be independent of whether a central diffractive event took place. This have been done by using the bunch group trigger L1_ALFA_BGT_BGRP10. This trigger saves an event for some random bunch group crossing, and it does not depend on whether any physics took place. If there is activity in ALFA in one of these random bunches, it is most likely due to a beam halo particle, since the rate of physics events that hit ALFA is extremely small. However since an elastic or single diffractive event could also cause a loss of the event, it should not be a problem, even if physics took place. The statistical error from this method is negligible. No rigorous method for determining a systematic uncertainty has been found. The efficiency seems to be quite stable, when changing the cuts slightly, but a conservative uncertainty of 0.5% has been estimated. The efficiencies have been separated into four categories based on what signal configuration, the beam halo particle would have ruined. For example a

central diffractive event, which was triggered by L1_ELAST15, would be ruined if one of the trigger pads not used was hit. In this case that would be the pads corresponding to POT₂|POT₄|POT₅|POT₇. The determined values can be seen in Table 22.

Trigger Item	Event survives veto %	Error%
ELAST 15	98.26	± 0.5
ELAST 18	98.29	± 0.5
SYST 17	98.03	± 0.5
SYST 18	97.74	± 0.5

Table 22: Signal events are thrown away due to the L1 trigger veto. The chance that a signal event of a given arm survives the veto is shown here. Because the arms have different rates of beam halo activity, they also have different efficiencies.

If the beam halo particle hits the same pot as the signal particle, there is a chance that the event is lost. This is included in the ALFA track reconstruction efficiency and the four track event veto efficiency.

Loss from Pile-up

The cut criteria of the analysis will remove events, where there are more than one pp interaction. When a signal event happens together with an inelastic event, the central diffractive event will almost always be lost. This is because the majority of collision are non-diffractive, which almost always either leave tracks in the Inner Detector or the MBTS. Since the cuts include the strict requirement of only two tracks (or four tracks) in Inner Detector, and nothing at all in the MBTS, then the event will be lost. Double diffractive and single diffractive will also often leave tracks in the MBTS. In principle there may be some double counting here with L1 veto loss, since a diffractive event can also hit the ALFA pots, but this effect is neglected, since the ALFA acceptance is low. In conclusion, all central diffractive events, which happen simultaneously with an inelastic collision, are expected to be lost. This results in an overall efficiency of:

$$\epsilon_{\text{pile-up}} = P(0) = e^{-\mu} \quad (41)$$

Here μ is the pile-up. $P(0)$ is then the probability that no collisions occur at a bunch crossing. When a central exclusive pion event within acceptance occurs, the probability that there are no other collisions, will be this. The pile-up is slightly different for the three runs. Since it is found from the inelastic cross section times the luminosity, the uncertainty is dominated by the error on the instantaneous luminosity and the inelastic cross section. A conservative estimate is around 5%. This uncertainty is strongly correlated with the luminosity. A too large luminosity will result in a measured cross section that is too low. It also results in a pile-up estimate, which is too large. If the pile-up is overestimated then the loss of events due to pile-up will also be overestimated, thus increasing the measured cross section. This has not been accounted for, so the error on the pile-up may be overestimated. The determined values can be seen in Table 23.

Run	$\langle\mu\rangle$	Error	$\epsilon_{\text{pile-up}}$ %	Error %
282026	0.086	± 0.005	91.8	± 0.4
282420	0.111	± 0.005	89.5	± 0.5
282455	0.099	± 0.005	90.6	± 0.4

Table 23: There is a loss of signal due to inelastic collisions, which happens simultaneously with signal events. $\epsilon_{\text{pile-up}}$ is the fraction of signal events, where there are additional collisions.

ALFA Track Reconstruction Efficiency

The method used here was developed in reference [45]. When the ALFA detector is hit by a proton the particle is always detected. However, there is a significant chance that no track is reconstructed, if there is too much noise generated in the detector. This happens quite often, since there is optical cross-talk and electrical cross-talk. It can also happen due to multiple particles hitting the detector at once. There will also be no reconstructed tracks if a signal proton converts to a particle shower when hitting a pot. This can also happen if a beam halo particle hits the collimator and converts to a shower covering a signal proton. If this happens, there will be no way to know if there actually were a signal proton, since we cannot reconstruct its track. Ideally this efficiency should be determined using full detector Monte Carlo, however no such simulation exists for ALFA.

The track reconstruction efficiency is determined by looking at central diffraction events that pass the same cuts as in the main analysis, but where some of the ALFA tracks were not reconstructed. When an ALFA track is not reconstructed, the proton position in the transverse plane is not measured. Therefore the proton momentum cannot be reconstructed, and this means that it is not possible to perform a cut on the total system momentum. The main technique for separating background and signal is therefore lost.

To check if a proton actually passed through the detector, it is required that at least 5 U-layer and 5 V-layer fibers are hit. The layer efficiency is around 90%, so the chance that a proton passes through the detector, but does not show a signal in at least 10 fibers is negligible. Because activity is required in both layers, a proton will not be confused with a noisy PMT, since the PMTs are all hooked up to either only U-layers or V-layers. A track is required to use more than 5 U- and V-layers, and it should be reconstructed $90\mu\text{m}$ from the edge. Three different track topologies are considered. The first is called $N_{4/4}$, and here a track is reconstructed in all four pots. Second are the events, where a track is reconstructed in 3 of 4 pots $N_{3/4}$. Finally is the topology, where the tracks are reconstructed in two pots on the same side $N_{SS2/4}$.

Only these topologies are considered, since the local angle $\theta_x = \frac{x_{\text{outer}} - x_{\text{inner}}}{245\text{m} - 237\text{m}}$ can be calculated, which makes a back to back cut possible. While this cut is not perfect, it still allows us to remove some background. There will still be background inside the back to back cut, but this has been deemed negligible. The veto on multiple L1 triggers firing at once, heavily limits the total amount of shower events. The rest of the track topologies $N_{2/4}$, $N_{1/4}$ and $N_{0/4}$ can be extrapolated with probability theory.

Probability Theory for Track Reconstruction Efficiency

The topologies $N_{2/4}$, $N_{1/4}$ and $N_{0/4}$ can be calculated, if it is assumed that the track reconstruction on the C-side is uncorrelated with the track reconstruction on the A-side. This is a very safe assumption. The probabilities that a track is reconstructed in station i and j is written as p_{ij} , and the amount of events with tracks in stations i, j, k , but no track in station l , is written as $N_{ijk\bar{l}}$. This means:

$$p_{12} \cdot p_{34} \cdot N_{\text{Total}} = N_{1234} \quad (42)$$

$$p_{12} \cdot p_{3\bar{4}} \cdot N_{\text{Total}} = N_{123\bar{4}} \quad (43)$$

$$p_{1\bar{2}} \cdot p_{34} \cdot N_{\text{Total}} = N_{\bar{1}234} \quad (44)$$

$$p_{\bar{1}\bar{2}} \cdot p_{34} \cdot N_{\text{Total}} = N_{\bar{1}\bar{2}34} \quad (45)$$

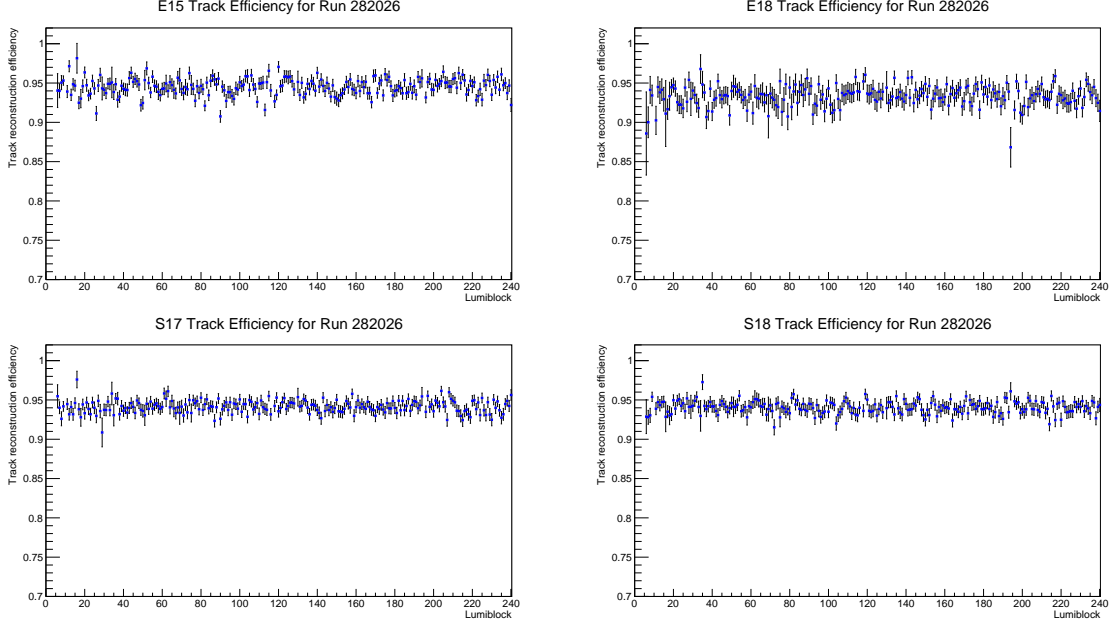


Figure 41: The ALFA track reconstruction efficiency as a function of lumiblock in run 282026. The efficiency is stable during time indicating a stable beam.

etc.. From this the remaining topologies can be found. For instance:

$$N_{1\bar{2}3\bar{4}} = p_{1\bar{2}} \cdot p_{3\bar{4}} \cdot N_{\text{Total}} = \frac{N_{1\bar{2}3\bar{4}}}{p_{3\bar{4}} \cdot N_{\text{Total}}} \cdot \frac{N_{123\bar{4}}}{p_{1\bar{2}} \cdot N_{\text{Total}}} N_{\text{Total}} = \frac{N_{1\bar{2}3\bar{4}} \cdot N_{123\bar{4}}}{N_{1234}} \quad (46)$$

$$N_{1\bar{2}3\bar{4}} = p_{1\bar{2}} \cdot p_{3\bar{4}} \cdot N_{\text{Total}} = \frac{N_{1\bar{2}3\bar{4}}}{p_{3\bar{4}} \cdot N_{\text{Total}}} \cdot \frac{N_{123\bar{4}}}{p_{1\bar{2}} \cdot N_{\text{Total}}} N_{\text{Total}} = \frac{N_{1\bar{2}3\bar{4}} \cdot N_{123\bar{4}}}{N_{1234}} \quad (47)$$

The track reconstruction efficiency is then calculated for each of the four arms, and the values can be seen in Table 24.

$$\epsilon_{\text{Reco}} = \frac{N_{4/4}}{N_{4/4} + N_{3/4} + N_{2/4} + N_{1/4} + N_{0/4}} \quad (48)$$

Trigger Item	ϵ_{Reco} %	stat. error %
ELAST 18	93.56	± 0.04
ELAST 15	94.51	± 0.04
SYST 17	93.99	± 0.03
SYST 18	94.13	± 0.03

Table 24: The ALFA track reconstruction efficiency for protons.

Systematic Uncertainty on Track Efficiency

The ALFA track reconstruction efficiency has in previous analysis been difficult to determine due to varying track reconstruction efficiency for background and signal. In this analysis, when determining the ALFA track reconstruction efficiency, no background subtraction has been made. However a veto if multiple L1 triggers fire is implemented. This removes a lot of events where a proton hits the collimator and creates a proton showers. In the previous ALFA analysis, such a veto was not an option.

The track efficiency has also been checked as a function of lumiblock. Since a beam halo particle can hit a collimator and cause a shower, a high level of beam halo particles will make the measured track reconstruction efficiency worse due to the lack of background subtraction. As seen on Figure 41 the track reconstruction efficiency is very stable. In previous analysis, where the detectors were much closer to the beam, the track efficiency has fallen as a function of lumiblocks, since beam halo accumulates over the course of the run. This means that there is a relatively stable beam during these runs.

It is however seen in the previous analysis that by doing systematic variations, the track reconstruction efficiency varied by about 2%. These checks has not been made in this thesis, so the uncertainty of 2%, which was obtained from previous ALFA analysis, is used.

Ghost Tracks and Track Matching

As can be seen on Figure 42, it is quite likely that multiple tracks will occur in a single pot, even when a single protons passes through the pot. This is due to detector noise in the pot. A proton will generally cause 10 fiber hits in the U-layer and 10 fiber hits in the V-layer. If there is then random detector noise in 3 of the V-layer fibers, a second ghost track will be made using the 3 noisy V-layer fibers and the 10 U-layer fibers, which were hit by the real proton. This track can have a completely different coordinate and therefore the reconstructed momentum using this track will be different as well. The majority of these ghost tracks can be removed by requiring that more than 5 U-layers and more than 5 V-layers are used for the track reconstruction. In the events, where there are two or three tracks in one detector, the chance that there are multiple tracks, which meets the ALFA tracking criteria is $\approx 4\%$. Since the amount of events with two and three tracks is already much lower than single tracks this is a small contribution to the total rate of events. When selecting the track that was reconstructed using the most U and V plates, then it is only in 0.77% of the three and two tracks events, where there is ambiguity in the choice of the best track. Since this is such a small fraction, the tracks are chosen based on hits in the U- and V-layers.

When multiple protons pass through the detector, other selection criteria are however needed. If two protons pass through the detector, then four tracks are reconstructed. All of these tracks will use close to 10 fibers in both layers. Two of these will correspond to actual protons, and two will correspond to ghost tracks. The majority of the time both protons will pass through both the inner and outer detectors generating four tracks in both. This gives us 16 different momentum configurations. No method to choose between these combinations without introducing bias has been found.

One approach would be to count every track combination as a separate event. A weight of $1/N_{\text{comb}}$ could be assigned to each of these events, where N_{comb} is the total amount of tracks combinations. This way every track is considered equally, and no bias from choosing ghost tracks that happens to look like signal, is introduced. However this will of course introduce some combinatoric background, which might not be found in any background subtraction scheme.

The option chosen in this analysis is to veto events, where there are four tracks that all match the tracking criteria. Events like these are expected to be a result of two protons passing through the detector. The total loss of signal by introducing this veto, should then correspond to the chance that a single proton hits the detector simultaneously with a central diffraction event. In the same manner as for the L1 veto efficiency, a bunch group trigger is

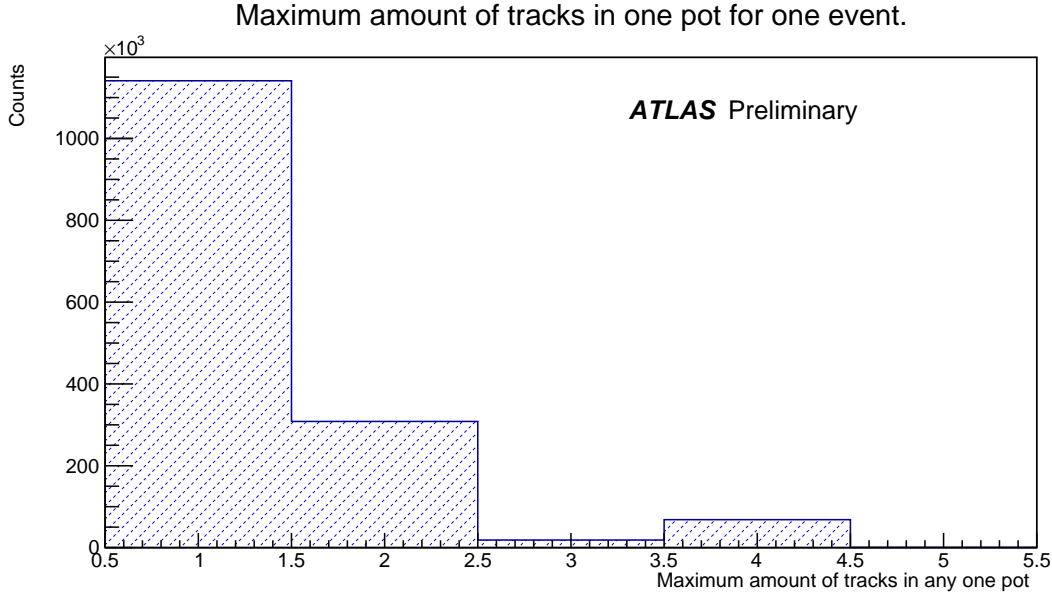


Figure 42: The maximum amount of tracks in any single pot during an event is shown. For example if one pot has two tracks, and the others have one, then it is counted as "2", since this is the maximum amount of tracks in any of the pots.

used to find the chance that a halo proton passes through a detector pair in a given event.

The efficiency is not the same as the L1 veto efficiency, since it is now required that the proton makes a single track in both detectors with more than 5 U- and V-plates, and that there is no activity in any of the other detectors. This is done to separate single protons from showers, which would not cause multi-track events. It also avoids introducing double counting from the L1 trigger veto. It is worth noting that there is still a bias from doing this. The track reconstruction efficiency is expected to be lower for an event, where there is multiple protons passing through the detector. When finding the track reconstruction efficiency, it is not known why a track failed to reconstruct. Therefore events that failed to reconstruct, because exactly two protons passed though the detector, cannot be excluded. This means that double counting occurs by compensating for a two proton veto in the analysis, but not doing so in the track reconstruction efficiency. The effect from this is expected to be small.

The efficiencies can be seen in Table 25. The statistical uncertainties are insignificant.

Trigger Item	$\epsilon_{4\text{track}}$ %	Error%
ELAST 15	99.3	± 0.01
ELAST 18	99.4	± 0.01
SYST 17	99.2	± 0.01
SYST 18	99.5	± 0.01

Table 25: The fraction of signal events that survive the cut on events with four ALFA tracks in one pot.

Uncertainty from the ALFA Four Track Veto

A conservative estimate of the systematic uncertainty on the cross section from the four track veto is found here. Since a momentum cut cannot be performed on the multi-track events,

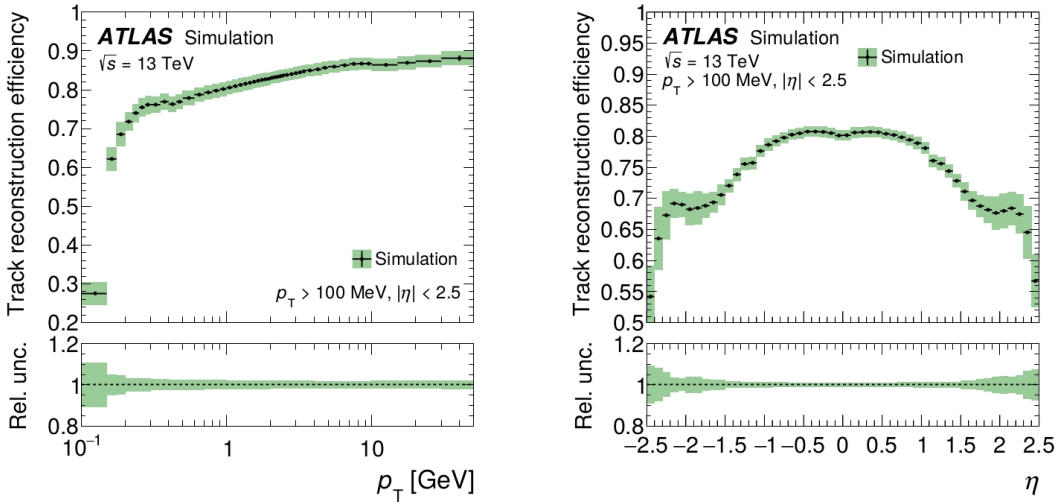


Figure 43: The Inner Detector track reconstruction efficiency for single tracks as a function of η and p_t . These results are from an ATLAS MinBias paper [12]. The efficiency was applied on an event by event basis based on η and p_t of the measured pions.

it is not known, how the ALFA four track veto affects background compared to signal. If it does not discriminate between the two, then the total fraction of events that is removed by the four track veto, is equal to the fraction of signal events removed by the veto. The four track veto retains 97.6% of the events that pass every other cut. Another option is to assume that every event, where there are four ALFA tracks that all pass tracking criteria in one pot, is background. If this is the case, then the four track veto gives us no loss of signal. The difference in the cross section between these two options is taken to be 2σ , and a uncertainty is obtained:

$$\sigma_{4\text{track}} = 0.23\mu\text{b} \quad (49)$$

For the final results, the efficiencies found for the four track veto is used.

ATLAS Inner Detector Efficiency

The Inner Detector efficiency is highly dependent on the p_t of the particles. Therefore it is important to know the exact efficiency for particles as a function of p_t and η . The Inner Detector efficiency values determined for another ATLAS Min-Bias study[12] is used for this study. The main difference between the two analyses is the pile-up, which in this analysis is $\mu = 0.1$, whereas it was $\mu = 0.005$ in the Min-Bias analysis. An Inner Detector efficiency for these particular runs should be found using MC, however, no full detector MC sample has been made for these runs at this point. The efficiency is found in the ATLAS paper by doing full detector simulation of MinBias events, and then counting how many charged particle was generated, and then checking if they had a corresponding reconstructed track.

In this analysis, the efficiency is applied on an event by event basis as a weight. This method is necessary since every event has a different weight, which is based on what the p_t and η of each of the particles in Inner Detector were.

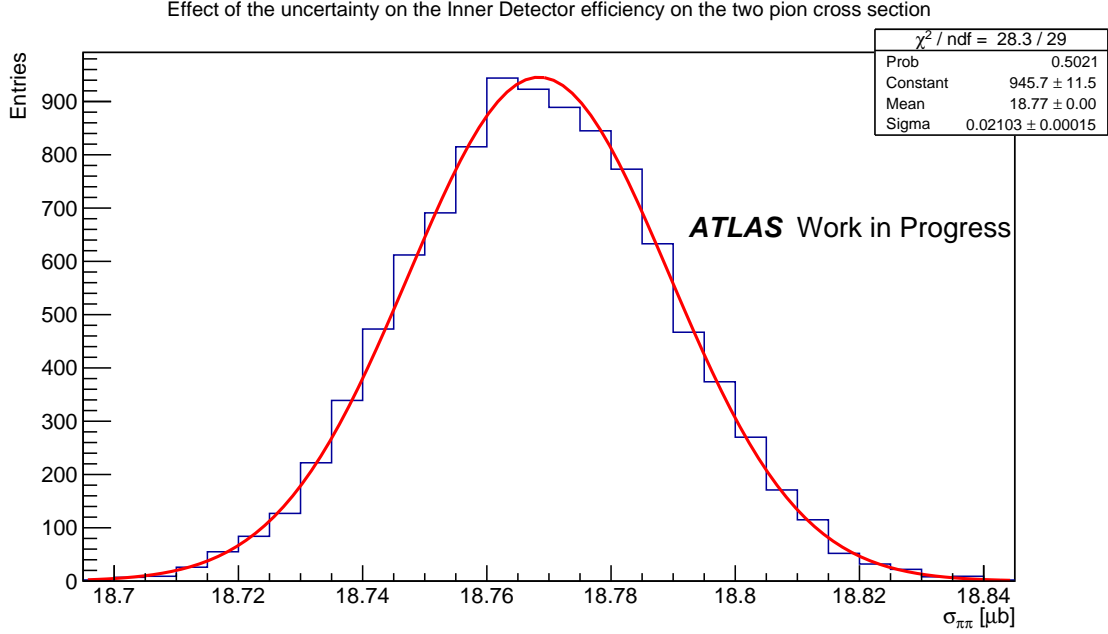


Figure 44: The uncertainty on the two pion cross section from the uncertainties of the Inner Detector efficiencies, extracted with a bootstrapping method.

Uncertainty from the Inner Detector Track Efficiency - $\pi\pi$

The overall uncertainty from Inner Detector on the cross section cannot be easily propagated since the different η/p_t regions have different uncertainties. Therefore a bootstrapping method is used. The approach is to build a random Inner Detector by generating a new efficiency for each specific p_t - η bin from a normal distribution. The mean is the reported Inner Detector efficiency and the standard deviation is the uncertainty. This is done for all the different efficiency bins. All the central diffractive events are then weighted based on the efficiency of this generated Inner Detector, and a cross section is calculated. This is then done 10000 times.

As can be seen from Figure 44, the uncertainty is

$$\sigma_{\text{InDet}} = 0.021\mu\text{b} \quad (50)$$

Uncertainty from the Inner Detector Track Efficiency - $\pi\pi\pi\pi$

For the four pion analysis, slightly different tracking criteria was used. Despite this, the same efficiencies from the ATLAS paper[12] were used. It has not been attempted to account for the uncertainty from this.

The exact same bootstrapping procedure used in the two pion case, is used here as well to determine the uncertainty on the cross section. As can be seen from Figure 45, the uncertainty is:

$$\sigma_{\text{InDet}} = 0.021\mu\text{b} \quad (51)$$

It is a coincidence that this value is the same as the uncertainty on the dipion cross section.

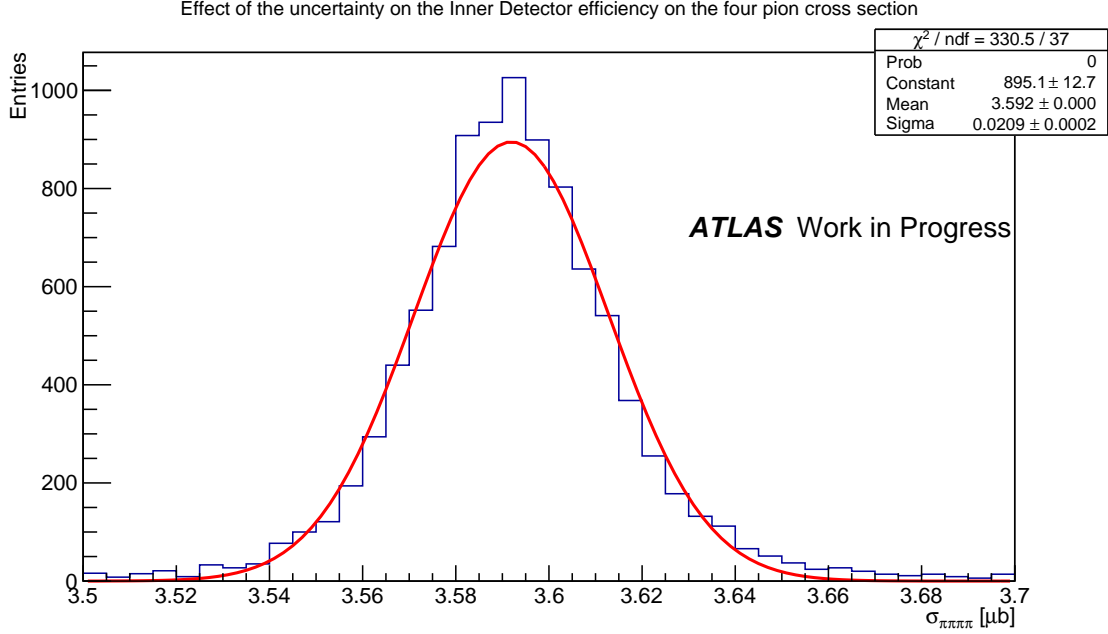


Figure 45: The uncertainty on the four pion cross section from the uncertainties of the Inner Detector efficiencies, extracted with a bootstrapping method.

Inner Detector Vertex Reconstruction

The approach used to calculate the vertex efficiency in the Inner Detector MinBias analysis is a data driven counting approach. First the tracking cut on z_0 is removed. Then the total amount of events where there are two tracks but no reconstructed vertex are counted. This approach cannot be used for the $\pi\pi$ analysis, since here the vertex efficiency is different for background and signal. This can be seen on Figure 46, which shows the mass spectrum of events with a missing vertex. Due to the long lifetime of neutral kaons, they are associated with events with no reconstructed vertex. Since the channel $\mathbb{P}\mathbb{P} \rightarrow K^0 \rightarrow \pi\pi$ is forbidden due to CP conservation, they generally appear only in background. Furthermore as seen from Figure 46, there is a huge peak at the $\pi\pi$ threshold. This originates from photons converting to e^+e^- , another background, which has worse vertex efficiency than signal.

The approach used to find the vertex efficiency is by counting the total amount of events with two reconstructed tracks and with balanced momentum within 2σ . The momentum is reconstructed using the beam spot position for all events, regardless of whether a vertex was reconstructed. The vertex efficiency is then the ratio of events with a vertex to the total event count:

$$\epsilon_{\text{Vertex}} = \frac{N_{\text{Vertex}}}{N} = 90.22 \pm 0.01\% \quad (52)$$

A problem with this approach is multiple scattering of signal pions. If this happens, the total system will be less likely to have balanced momentum within 2σ . The event will also be less likely to have a reconstructed vertex from Inner Detector. This would make the true vertex efficiency slightly worse. However since there is also some background in the 2σ signal region, which have lower vertex efficiency, this would make the measured vertex efficiency slightly lower. These two effects might cancel each other.

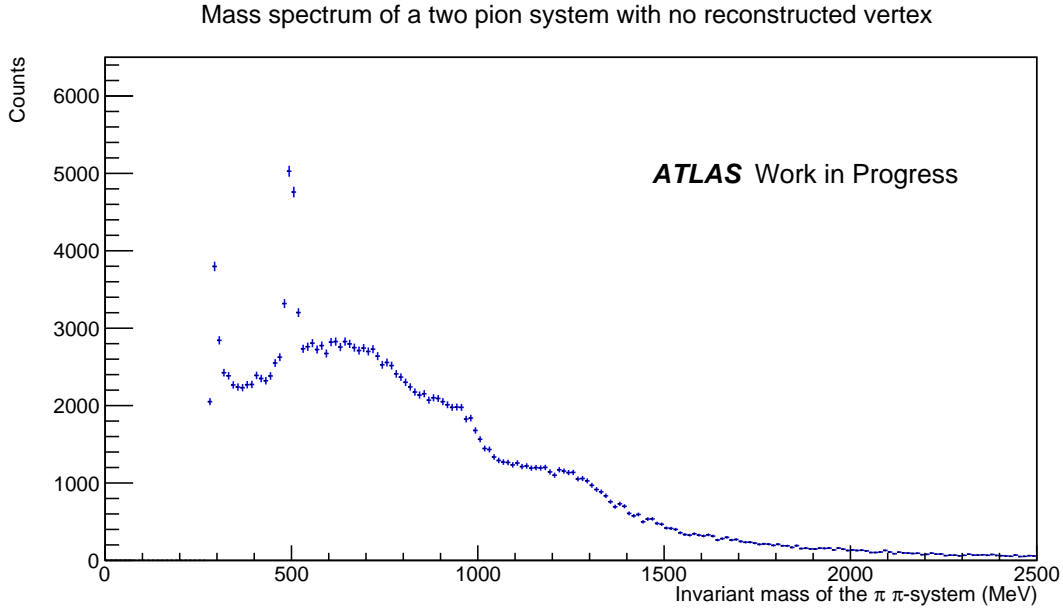


Figure 46: The mass spectrum of the two pion system with only events that have no reconstructed vertex. As can be seen there is a large peak at the neutral kaon mass and at the pion threshold.

The approach to find the systematic uncertainty on the cross section from the vertex efficiency, is to do the analysis without requiring any vertex and then comparing the results. Doing the analysis with no primary vertex worsens the momentum resolution of the protons slightly and it increases the background to signal ratio, however it is an option.

For the four pion analysis no special treatment of the vertex efficiency is required, since the vertex efficiency is expected to be the same for signal and background. The total amount of four track events with no tracking restrictions on z_0 is counted. When taking the ratio of the total events, and the events with a vertex, the efficiency is obtained:

$$\epsilon_{\text{Vertex},4\pi} = 99.11 \pm 0.02\% \quad (53)$$

For the four pion vertex efficiency only the statistical uncertainty is used, since no systematic effects are expected.

Uncertainty from the Vertex Efficiency

The analysis can be done without requiring a vertex. This does increase the background to signal ratio. The proton momentum is reconstructed using the beam spot every time, and no ATLAS vertex information is used in order to avoid introducing any bias. When using Scaling Method 2 to normalize the background template, the scaling factors seen in Table 26 are obtained.

Arm	Scaling Factor	Error	χ^2/ndf
ELAST18	5.48	± 0.04	1.57
ELAST15	5.44	± 0.04	1.37
SYST17	5.37	± 0.03	4.14
SYST18	5.33	± 0.03	3.56

Table 26: The background scaling factors determined using Scaling Method 2, when no vertex requirement is imposed.

When using a 5σ cut, the calculated cross section is:

$$\sigma_{\pi\pi, \text{NoV}} = 18.85\mu\text{b}$$

The difference between this and the obtained cross section, when requiring a vertex, is found.

$$\Delta\sigma_V = \sigma_{\pi\pi, V} - \sigma_{\pi\pi, \text{NoV}} = 0.10\mu\text{b}$$

This is put as the uncertainty on the cross section from the vertex efficiency.

Results

Both the central exclusive dipion and four pion production results are presented here. The analysis procedure are identical for the two results, however there is a much larger uncertainty both statistically and systematically on the four pion result. The increase in systematic uncertainty is due to a much higher rate of background.

Central Exclusive $\pi\pi$ Production Cross Section

The central exclusive $\pi\pi$ production cross section is found by counting.

$$\sigma_{pp \rightarrow p + \pi\pi + p} = \frac{N_{\text{sig}} - a \cdot B_{\text{sig}}}{L \cdot A \cdot \epsilon_{\text{InDet}} \cdot \epsilon_{\text{Reco}} \cdot \epsilon_{\text{Vertex}} \cdot \epsilon_{\text{L1}} \cdot \epsilon_{\text{HLT}} \cdot \epsilon_{\text{VetoL1}} \cdot \epsilon_{\text{pile-up}} \cdot \epsilon_{\text{4track}}} \quad (54)$$

Here N_{sig} is the the amount of events in the momentum signal region with opposite charge, and B_{sig} is the amount of same sign charge events in the signal region. a is the background scaling factor, A is the acceptance and L is the integrated luminosity. This is calculated for the arms separately due to the varying efficiencies, and then summed up. Using the Donnachie-Landshoff model with an $\alpha' = 0.126\text{GeV}^{-2}$, a cross section for the pion fiducial volume of $p_t > 100$ and $-2.5 < \eta < 2.5$ is obtained:

$$\sigma_{pp \rightarrow p + \pi\pi + p}^{\text{fid1}} = 18.754 \pm 0.048(\text{stat.}) \pm 0.770(\text{syst.})\mu\text{b}, \quad |\eta_\pi| < 2.5, \quad p_{t,\pi} > 100\text{MeV} \quad (55)$$

Systematics for the $\pi\pi$ cross section	Unc. [μb]
L1 Trigger Veto	0.049
Vertex Efficiency	0.10
Background Subtraction	0.265
ALFA Track Reco Efficiency	0.205
Inner Detector Efficiency	0.021
Four Track Veto	0.23
L1 Trigger Efficiency	0.004
HLT Efficiency	0.093
Proton acceptance from α'	0.207
Wrong PID of K^+K^-	0.2
Pile-Up	0.084
Luminosity	0.563

Table 27: The systematic uncertainties to the $\pi\pi$ cross section

The most optimistic uncertainty is the proton acceptance, since it is model dependent. The result obtained using the Donnachie-Landshoff and MBR with different values of α' can be seen in Table 28.

$\alpha'[\text{GeV}^{-2}]$	Donnachie-Landshoff	MBR
0.126	$18.75 \pm 0.77\mu\text{b}$	$18.15 \pm 0.74\mu\text{b}$
0.2	$19.85 \pm 0.82\mu\text{b}$	$18.99 \pm 0.78\mu\text{b}$
0.3	$22.29 \pm 0.92\mu\text{b}$	$20.84 \pm 0.86\mu\text{b}$
0.4	$25.45 \pm 1.05\mu\text{b}$	$23.68 \pm 0.97\mu\text{b}$

Table 28: $\sigma_{pp \rightarrow p+\pi\pi+p}^{\text{fid1}}$, when using an acceptance determined with different models.

When defining a fiducial volume for the protons based on $-t$ of $t_A, t_B > 0.03\text{GeV}^2$, the acceptance is much less model dependent.

$$\sigma_{pp \rightarrow p+\pi\pi+p}^{\text{fid2}} = 12.433 \pm 0.032(\text{stat.}) \pm 0.510(\text{syst.})\mu\text{b}, \quad |\eta_\pi| < 2.5, \quad p_{t,\pi} > 100\text{MeV}, \quad t_A, t_B > 0.03\text{GeV}^2 \quad (56)$$

For this fiducial volume the different models are more consistent as seen in Table 29.

$\alpha'[\text{GeV}^{-2}]$	Donnachie-Landshoff	MBR
0.126	$12.43 \pm 0.51\mu\text{b}$	$12.40 \pm 0.51\mu\text{b}$
0.2	$11.99 \pm 0.49\mu\text{b}$	$11.87 \pm 0.49\mu\text{b}$
0.3	$11.98 \pm 0.49\mu\text{b}$	$11.69 \pm 0.48\mu\text{b}$
0.4	$12.15 \pm 0.50\mu\text{b}$	$11.95 \pm 0.49\mu\text{b}$

Table 29: $\sigma_{pp \rightarrow p+\pi\pi+p}^{\text{fid2}}$, when using an acceptance determined with different models.

Of course if the reader wishes to correct with respect to their own theoretical model it can be done using Alexander Linds ALFA simulation[37]. The cross section without any acceptance correction is:

$$\sigma_{pp \rightarrow p+\pi\pi+p}^{\text{visible}} = 3.877 \pm 0.011(\text{stat.}) \pm 0.146(\text{syst.})\mu\text{b} \quad (57)$$

For comparison with other results the total cross section can be corrected to the full phase space using the Donnachie-Landshoff model.

$$\sigma_{pp \rightarrow p+\pi\pi+p}^{\text{full}} = 109.8 \pm 0.3(\text{stat.}) \pm 4.3(\text{syst.})\mu\text{b} \quad (58)$$

No extra uncertainty from the model dependence on this correction has been added. The previous result has just been scaled up.

Central Exclusive $\pi\pi$ Production Mass Spectrum

The differential cross section as a function of the dipion invariant mass can be seen on Figure 47.

The $f_2(1275)$ and $f_0(980)$ mesons are clearly visible in the spectrum. The $f_0(500)$ is dominating in the low mass region. The fit model, described in the section on resonance fitting, has been used to extract the widths and masses. Here the bare Breit-Wigners with no interference terms have been drawn to illustrate the different resonances widths and masses. When summing everything and including interference terms, the overall fit result is obtained. The mass spectrums predicted by MC can be seen in the appendix.

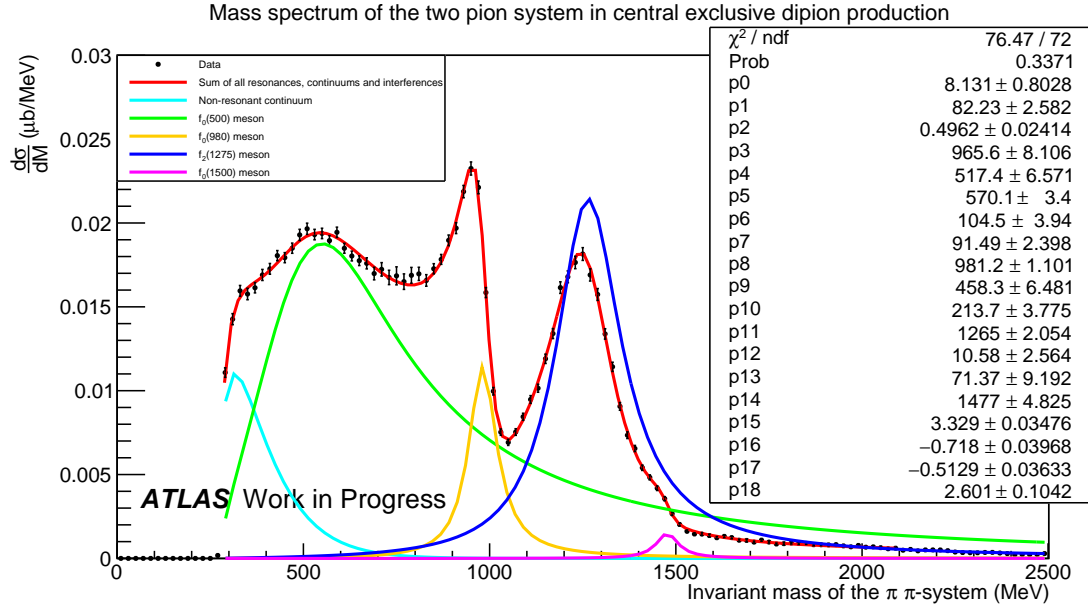


Figure 47: The differential cross section as a function of the dipion invariant mass. The total fit is shown in the red color. Bare Breit-Wigners with no interference effects has been drawn separately for the different resonances to illustrate their widths and masses.

Reggeon Mass and Widths

From the invariant mass fit the mesons widths and masses can be extracted. In Table 30 the values and uncertainties are shown as obtained from the fit. The cross section for each of the channels is difficult to determine, since the interference effects are so strong. Integrating under the single Breit Wigner is not a good approach as it does not correspond to anything physical. The used approach, is to integrate under the mass intervals, which seem to be dominated by a specific resonance. Specifically for the $f_0(980)$ cross section the mass interval 900 MeV to 1100 MeV has been integrated under. Next for the $f_2(1275)$ the interval from 1100 to 1300 MeV has been used. Finally for the $f_0(1500)$ it seems only possible to integrate under the bare Breit-Wigner.

Meson	Mass [MeV]	Width [MeV]	Relative Phase	Cross Section [μb]
$f_0(500)$	570 ± 3	517 ± 7	3.33 ± 0.03	-
$f_0(980)$	981 ± 1	91 ± 2	-0.72 ± 0.04	2.87 ± 0.15
$f_2(1275)$	1265 ± 2	214 ± 4	-0.52 ± 0.04	3.74 ± 0.19
$f_0(1500)$	1477 ± 5	71 ± 9	2.60 ± 0.10	0.16 ± 0.02

Table 30: The meson parameters extracted from the fit of the mass spectrum.

The width of the $f_2(1275)$ is much larger than the reported PDG value of around 186MeV, and the mass is also shifted slightly. This could be because there is a contribution from the $f_0(1370)$ meson. It is expected to decay in the $\pi\pi$ channel, but it is not visible since it is completely overlapping with the $f_2(1275)$. The parameters of the $f_0(500)$ meson is clearly quite dependent on how the non-resonant continuum is modeled.

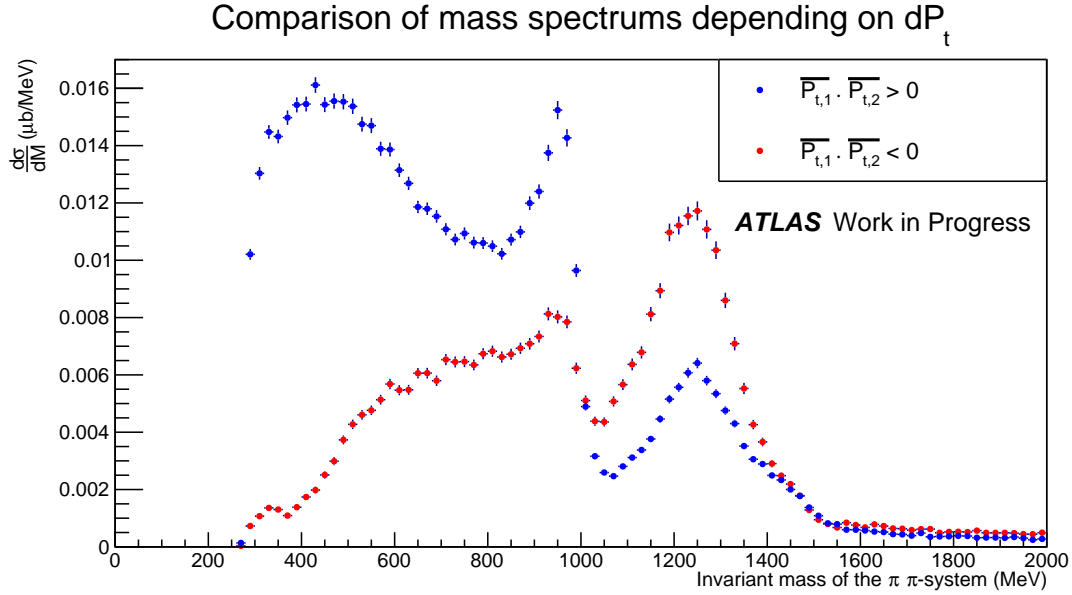


Figure 48: For $|\eta_\pi| < 2.5$, $p_{t,\pi} > 100\text{MeV}$. The differential cross section as a function of the two pion invariant mass. Here it is separated into two categories depending on the difference in outgoing transverse momentum of the protons. From an experimental setup the red spectrum corresponds to trigger items ELAST15 and ELAST18, whereas the blue spectrum correspond to SYST17 and SYST18.

Outgoing Transverse Proton Momentum and the Mass Spectrum

The difference between the outgoing protons transverse momentum affects the mass spectrum. When separating events into two classes depending on the outgoing transverse momentum of the protons, $P_{t,1}$ and $P_{t,2}$, different distributions are obtained. It is seen that when looking at events, where both protons are in the opposite side of the y -axis in the transverse plane, $\overline{P_{t,1}} \cdot \overline{P_{t,2}} < 0$, and on the same side of the y -axis in the transverse plane, $\overline{P_{t,1}} \cdot \overline{P_{t,2}} > 0$, different distributions are obtained. This is not attributable to detector efficiencies or kinematical acceptance. Similar effects have been seen before in both the AFS at the ISR and in the WA91 experiment[17][15], which also have completely different kinematics and acceptances. The effect can be seen on Figure 48. When the protons hit the detectors on opposite sides, $\overline{P_{t,1}} \cdot \overline{P_{t,2}} < 0$, there is a low contribution from the $f_0(980)$ meson, whereas the contribution from the $f_2(1275)$ meson is amplified. The opposite is the case for the protons with $\overline{P_{t,1}} \cdot \overline{P_{t,2}} > 0$.

It is predicted from MC that there is a drop in the cross section for $\overline{P_{t,1}} \cdot \overline{P_{t,2}} < 0$ below $m_{\pi\pi} < 550\text{MeV}$, however not to the extent, which is seen in data. It appears that the $f_0(500)$ meson is not contributing in the $\overline{P_{t,1}} \cdot \overline{P_{t,2}} < 0$ spectrum. To check whether this have something do to with the pion fiducial volume, the spectrum has been corrected with respect to the full phase space, which can be seen on Figure 49. The same effect is still seen. The MC mass spectrums can be seen in the appendix.

t-Spectrum

The differential cross section can also be plotted as a function of the proton $-t$, where

$$-t \approx_{s \rightarrow \infty} p_x^2 + p_y^2.$$

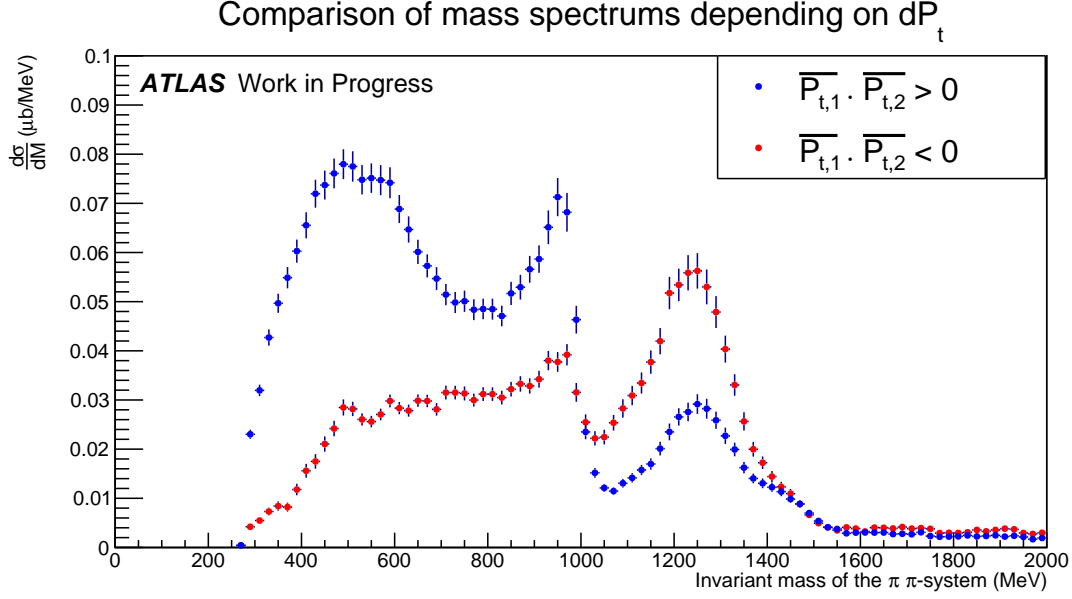


Figure 49: For comparison the mass spectrum of the pions has been corrected to the full phase space. No major difference in the spectrum shape is seen.

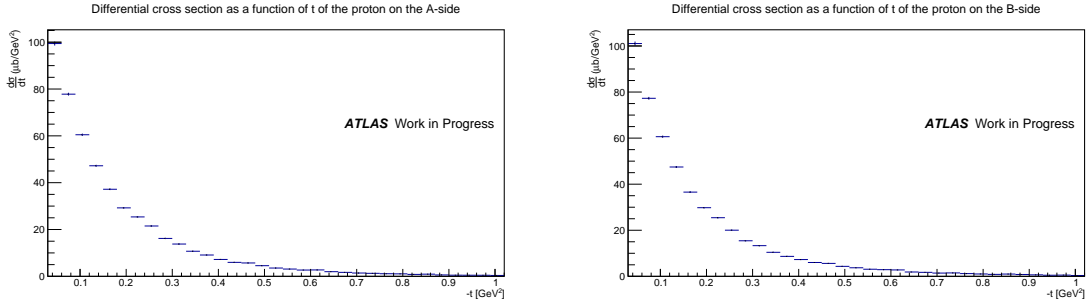


Figure 50: For $|\eta_\pi| < 2.5$, $p_{t,\pi} > 100\text{MeV}$. Differential cross section of $-t$ in terms of the A side proton and B side proton in central exclusive $\pi\pi$ production. We have a minimum of $-t = 0.03\text{GeV}^2$. For each of the respective distributions, an integration over the other protons t has been performed.

The other protons $-t$ is integrated over. Here only the values of $t > 0.03\text{GeV}^2$ are plotted. The cross section is plotted for both the A-side proton and the B-side proton on Figure 50, which look completely identical.

It turns out that the different central diffractive arms (the difference in the outgoing proton transverse momentum), has quite different t -distributions, as seen on Figure 51. There are far fewer protons exchanging low t in the events with outgoing protons hitting detectors in the opposite hemisphere. This is in agreement with the mass spectrum, where fewer low invariant mass events were seen for $\overline{P_{t,1}} \cdot \overline{P_{t,2}} < 0$. Similarly to the mass spectrum this effect is not seen in MC and is not a kinematical acceptance issue. The t -exchange of proton 1 is highly correlated with the outgoing direction of proton 2. The difference in the t -spectrum could either be due to this correlation not being incorporated in the MC used to calculate the acceptance, or it could be that the t -spectrum is different. It is proposed that this is a resonance effect, since it is not seen in the four pion interaction.

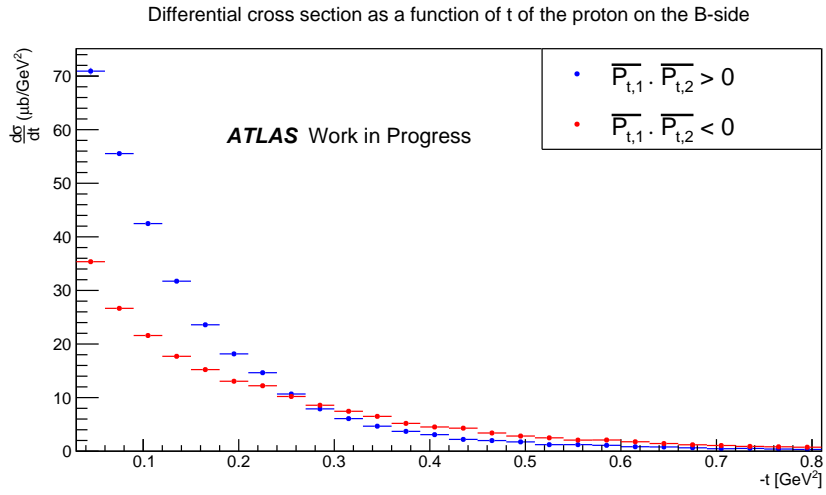
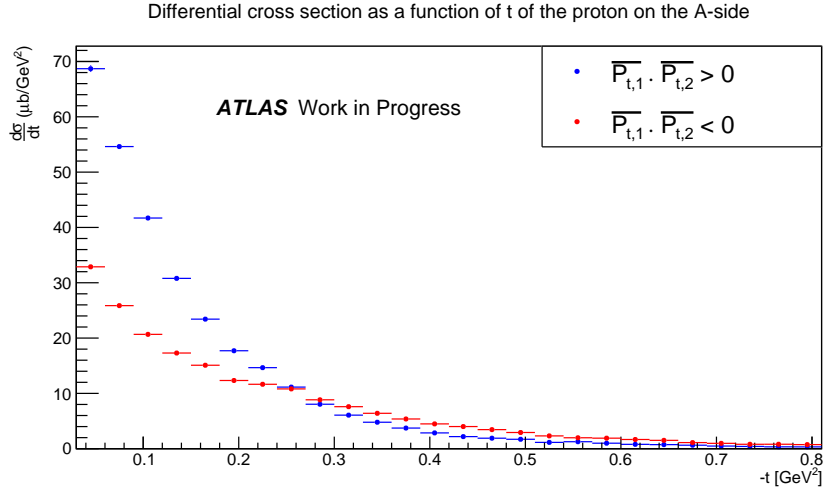


Figure 51: For $|\eta_\pi| < 2.5$, $p_{t,\pi} > 100\text{MeV}$. Differential cross section of $-t$ for each of the respective protons in central exclusive $\pi\pi$ production. There is a clear difference in the proton t depending on the other protons outgoing momentum. This does not appear to be an acceptance effect, since it is not seen in MC.

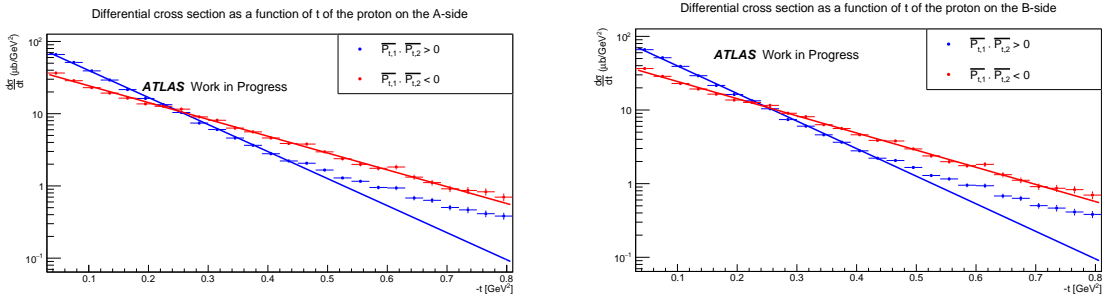


Figure 52: For $|\eta_\pi| < 2.5$, $p_{t,\pi} > 100\text{MeV}$. Differential cross section of $-t$ in terms of the A side proton and B side proton in central exclusive $\pi\pi$ production. We have a minimum of $-t = 0.03\text{GeV}^2$. When fitting an exponential, it appears the slope change for same side protons around 0.45GeV^2 . Beyond that the two distributions have the same t slope.

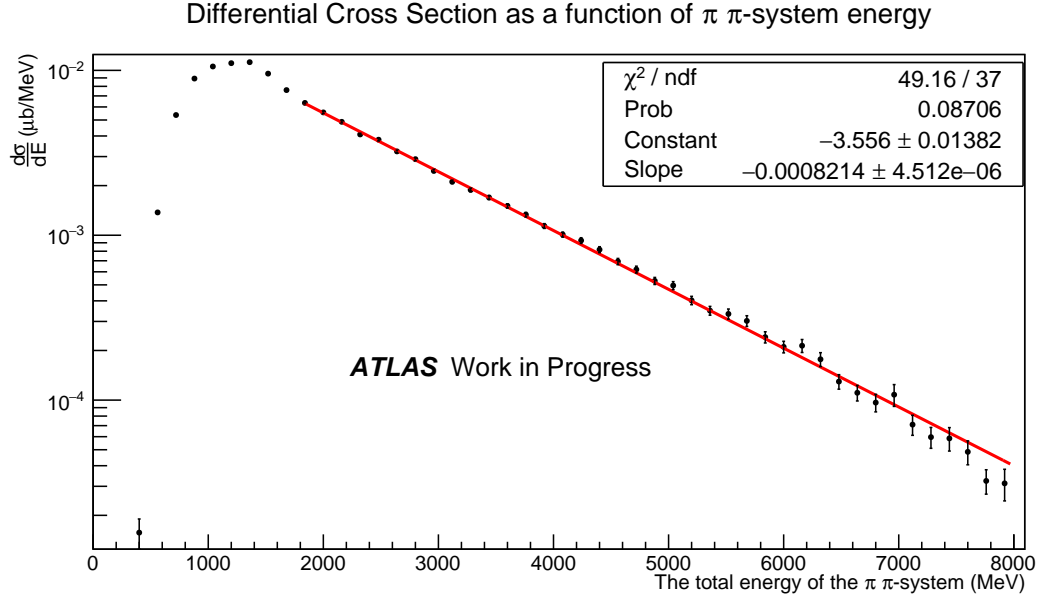


Figure 53: For $|\eta_\pi| < 2.5$, $p_{t,\pi} > 100\text{MeV}$. Differential cross section of total energy of the two pion system. An exponential has been fitted to the region, where the pion fiducial volume has minimal effect.

Energy Spectrum

The differential cross section as a function of the pion energy is plotted on a log scale on Figure 53. An exponential fit matches well for the high pion energy. The pomeron flux parameters could possibly be extracted from this slope. A quick comparison with Monte Carlo seems to indicate that the energy dependence favors low α' and low ϵ in the Donnachie-Landshof Model.

Extraction of α'

The t -spectrum of protons in central exclusive dipion production is sensitive to the Pomeron flux parameter α' in the Donnachie-Landshof model. α' can be measured by doing bin to bin comparisons between the raw t -spectrum in data and the t -spectrum from Monte Carlo samples generated with PYTHIA8, which has been run through the detector simulation. A measurement like this could be highly model dependent, and none of the central diffractive models are perfect. As seen in the previous section the t -spectrums of the different arms have vastly different slopes, which is not predicted by the Donnachie-Landshof model. This should also be checked with MBR. These different slopes correspond to different values of α' . Therefore the bin to bin comparison have been done separately for the same side arms and the opposite side arms.

In Figure 54, it can be seen that the events with $\overline{P}_{t,1} \cdot \overline{P}_{t,2} < 0$ corresponds to a very low α' , whereas $\overline{P}_{t,1} \cdot \overline{P}_{t,2} > 0$ corresponds to a much higher α' , which looks to be consistent with the Donnachie-Landshof measurement of $\alpha' = 0.25\text{GeV}^{-2}$. It is however also clear that the MC model doesn't describe data very well, so any parameters extracted using this approach will almost certainly not correspond to the α' , which is a fundamental parameter of diffraction. When combining the arms an α' of around 0.15GeV^{-2} is obtained. This could perhaps also be tried for 4π , where the different arms look identical.

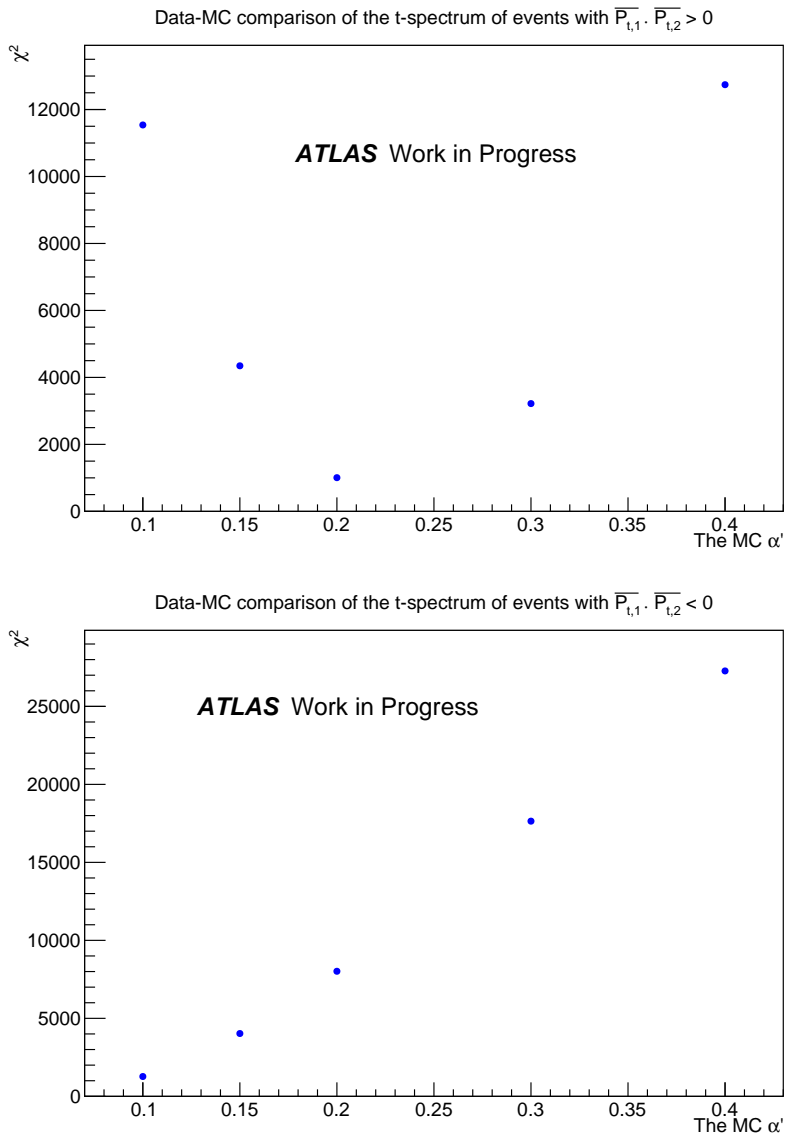


Figure 54: The χ^2 when comparing the t-spectrum of MC with data as a function of the MC parameter α' . The upper diagram shows the extracted α' for events with protons on the same side of the transverse plane, and below are events with protons on the opposite side of the transverse plane.

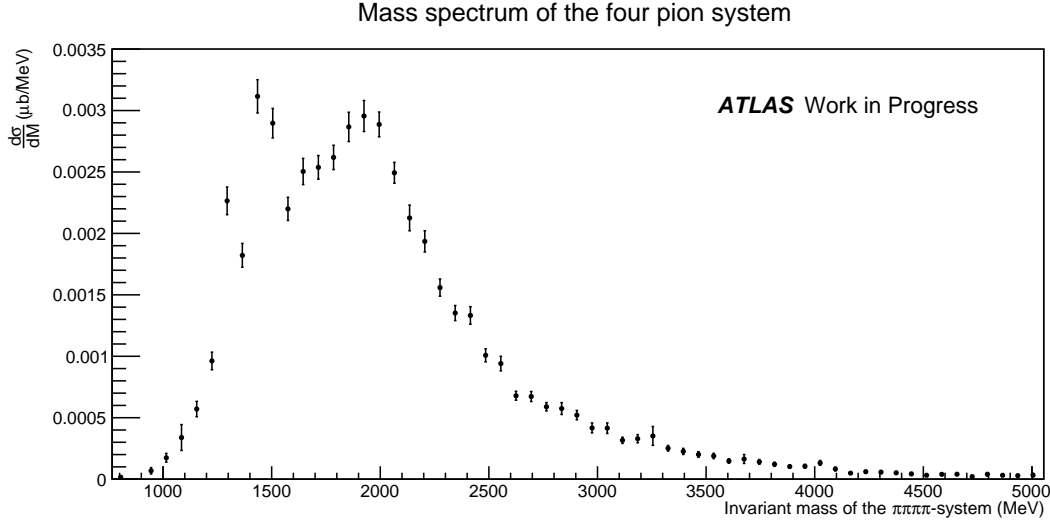


Figure 55: The differential $pp \rightarrow p + 4\pi + p$ cross section as a function of invariant mass.

Central Exclusive $\pi\pi\pi\pi$ Production Cross Section

For the process $pp \rightarrow p + \pi\pi\pi\pi + p$, the obtained cross section is:

$$\sigma_{pp \rightarrow p+4\pi+p}^{\text{fid1}} = 3.575 \pm 0.065(\text{stat.}) \pm 0.338(\text{syst.})\mu\text{b}, \quad |\eta_\pi| < 2.5, \quad p_{t,\pi} > 100\text{MeV} \quad (59)$$

The largest systematic uncertainty is by far from background subtraction.

Systematics for the 4π cross section	Unc. [μb]
L1 Trigger Veto	0.009
Vertex Efficiency	0.0007
Background Subtraction	0.316
ALFA Track Reco Efficiency	0.038
Inner Detector Efficiency	0.021
Four Track Veto	0.044
L1 Trigger Efficiency	0.0006
HLT Efficiency	0.018
Proton acceptance from α'	0.052
Pile-Up	0.016
Luminosity	0.083

Table 31: The systematic uncertainties to the $\pi\pi\pi\pi$ cross section

Central Exclusive $\pi\pi\pi\pi$ Production Mass Spectrum

The differential cross section of the four pion mass spectrum is shown in Figure 55. A resonance at around 1500 MeV corresponding to the $f_0(1500)$ meson is seen. Furthermore a second resonance around 1280 MeV is also seen. This could be the $f_1(1285)$ meson. This can only be produced via either $\gamma\mathbb{P} \rightarrow f_1(1285)$ or $\mathbb{R}\mathbb{P} \rightarrow f_1(1285)$, which are both suppressed. The mass spectrum shows no dependence on the difference in outgoing proton momentum.

Dalitz plot of central exclusive four pion production

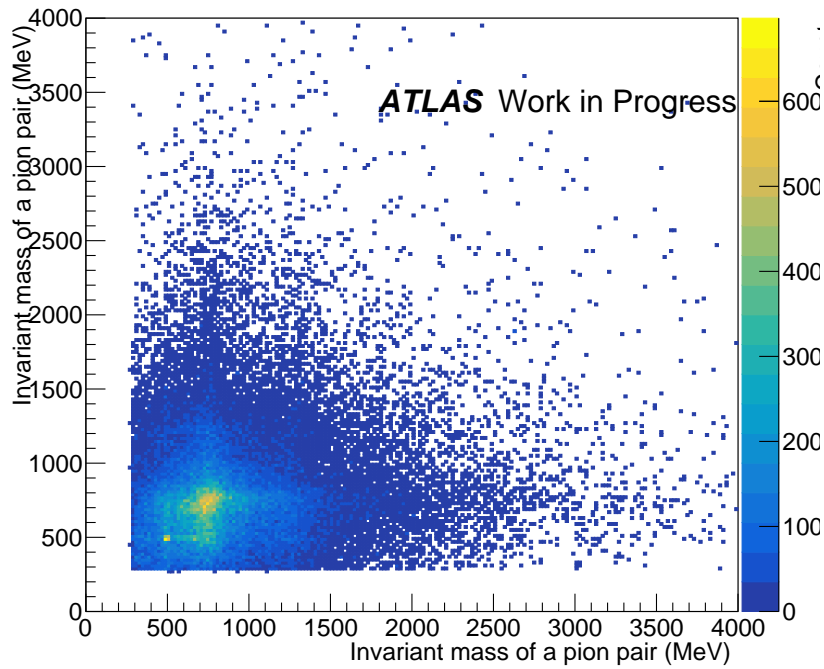


Figure 56: A Dalitz plot including combinatorial background of the four pion process. The sharp peak at around (500MeV,500MeV) shows the $K\bar{K}$ -channel and the wider peak at (770MeV,770MeV) shows the $\rho\rho$ -channel

Dalitz Plot

A Dalitz plot of the four pion system has been made by taking each of the pion pairs and plotting the invariant mass. Since there are four pions, there are four different pion pairs, which means there is combinatoric background. As seen on Figure 56, there is a large contribution to $\mathbb{P}\mathbb{P} \rightarrow \pi\pi\pi\pi$ via the $\rho\rho$ channel and the $K\bar{K}$ channel. No tracking criteria on z_0 and d_0 has been used here in order to capture the $K\bar{K}$ resonance.

Discussion

In this chapter the results are compared to previous measurements, and the implications of the differences are explained. Finally some ideas for future studies are presented.

Comparison with ISR

The ISR has measured the central exclusive dipion production cross section at $\sqrt{s} = 62\text{GeV}$ [17]. The cross section was measured to be

$$\sigma_{pp \rightarrow p+\pi\pi+p}^{\text{ISR},62\text{GeV}} = 79 \pm 15\mu\text{b} \quad (60)$$

The cross section changes with the beam energy, but it is not known at what rate. The total cross section at 62 GeV is around 40mb and at 13TeV it is around 100mb . If we assume central diffraction scale with the total cross section, we would predict a ISR cross section of around $45\mu\text{b}$. The measured scaling factor between the two results is $a = 1.4 \pm 0.3$.

The mass spectrum measured with the AFS at ISR can be seen on Figure 57. The spectrum is quite different from the $\sqrt{s} = 13\text{TeV}$ spectrum. At $\sqrt{s} = 62\text{GeV}$, there is still quite a bit of reggeon exchanges. This means that the ρ meson is still dominating. The $f_0(980)$ and the $f_2(1275)$ resonances are quite weak. The resonances that are amplified at $\sqrt{s} = 13\text{TeV}$ may have a gluonic substructure, since Double Pomeron Exchange dominates at high energies, and the Pomeron is expected to couple strongly to gluonic mesons.

The approach for the partial wave analysis used in this thesis, is the same approach used by the ISR group. As can be seen on Figure 58, the dip around 1300MeV for the SD matrix is the same as in this analysis (Figure 33). The SS density matrix does however look quite different.

Comparison with WA91

The dependence on the mass spectrum of the proton outgoing transverse momentum was first seen at the fixed target experiment WA91 [15]. This looks extremely similar to what we see today, although a bit less pronounced. The plots can be seen on Figure 59. Since this was a fixed target beam of 450GeV, corresponding to $\sqrt{s} = 28\text{GeV}$, then the ρ meson is still prominent. As can be seen the ρ meson appears stronger, when there is a large difference in outgoing momenta, but disappears completely, when the difference in transverse momentum is low. It was proposed based on this data that the difference in outgoing transverse proton momenta acts as a $q\bar{q}$ discriminator[16], since the ρ meson is a well established $q\bar{q}$ state.

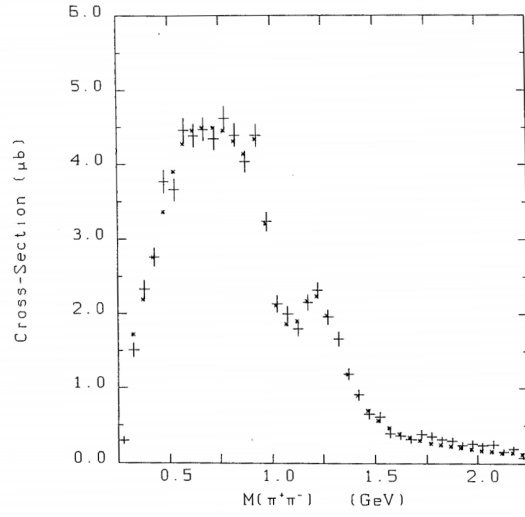


Figure 57: The ISR mass spectrum.[17]

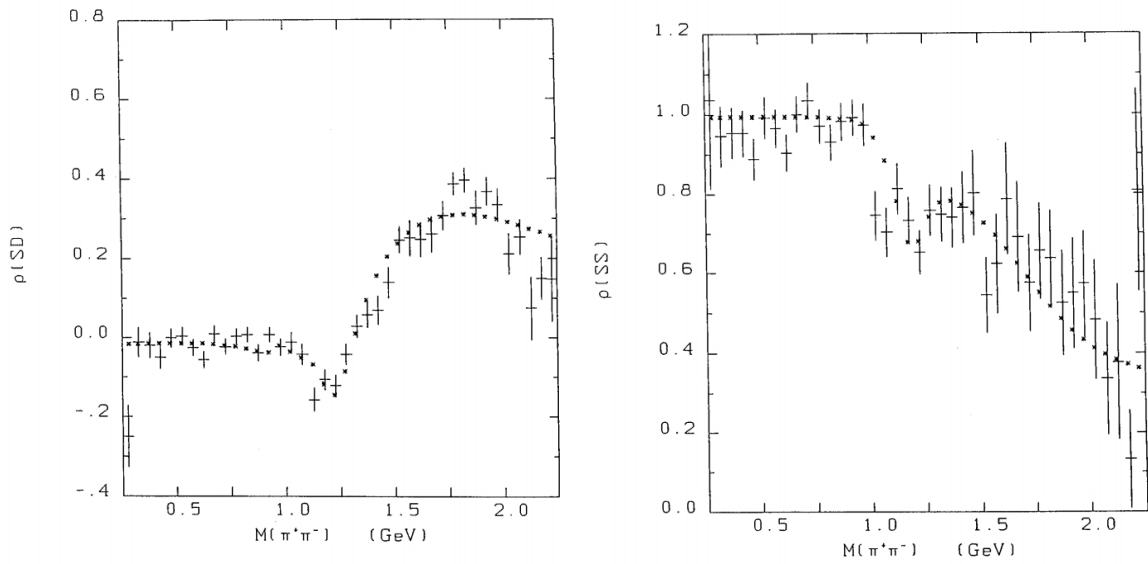


Figure 58: The ISR density matrices.[17]

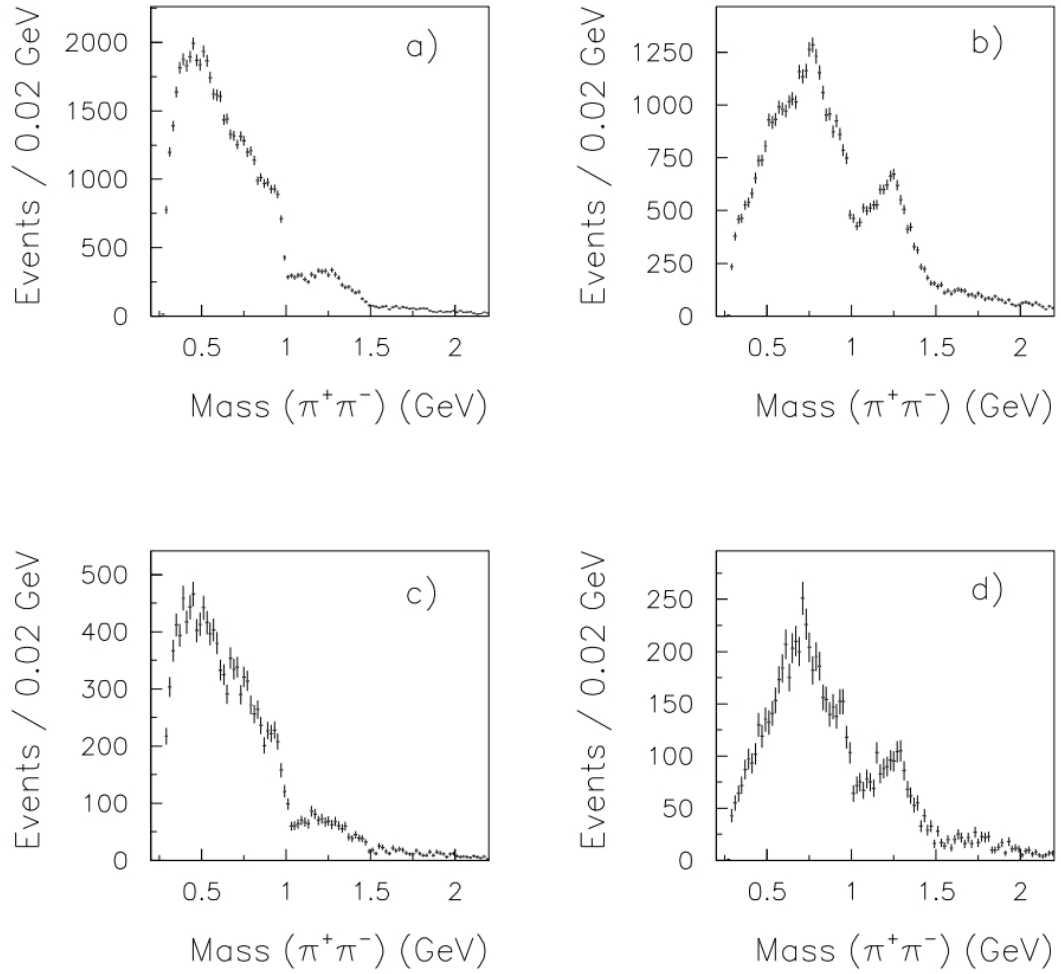


Figure 59: The WA91 mass spectrum dependence on transverse outgoing momentum. Here figure A and C corresponds to same side outgoing protons, whereas B and D refers to opposite side outgoing protons. [15]

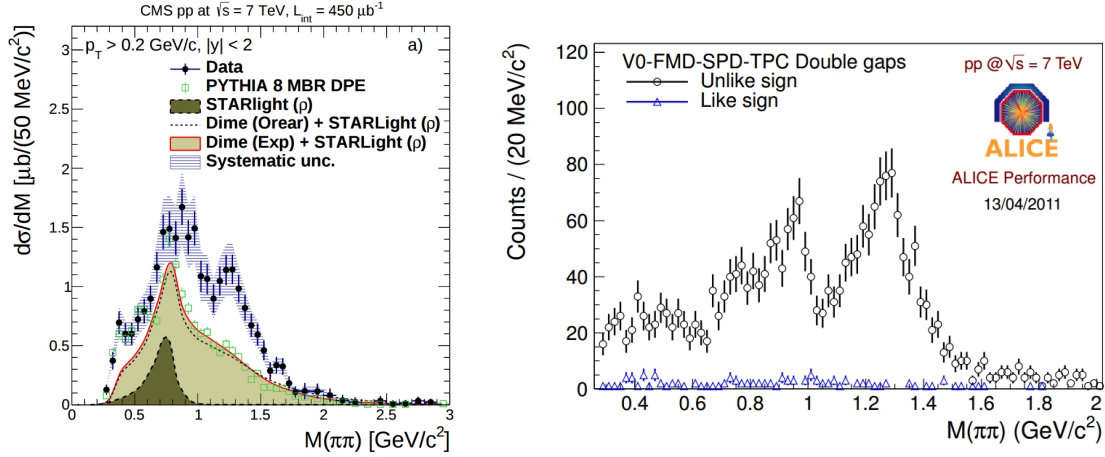


Figure 60: The CMS[11] dipion mass spectrum can be seen on the left. The ALICE[9] mass spectrum can be seen on the right.

Comparison with CMS and ALICE

ALICE and CMS have only published central exclusive and semi-inclusive dipion production. This is due to a lack of tagging of the forward protons. It is therefore not certain whether or not the proton dissociated, so the measured cross section includes both. In the CMS paper[11], they had a center of mass energy of $\sqrt{s} = 7\text{TeV}$. Their obtained result was:

$$\sigma_{pp \rightarrow p(p^*) + \pi\pi + p(p^*)}^{\text{CMS}} = 26.5 \pm 0.3(\text{stat.}) \pm 5.0(\text{syst.}) \pm 1.1(\text{lumi.}) \mu\text{b}, \quad |\eta_\pi| < 2.0, \quad p_{t,\pi} > 200\text{MeV} \quad (61)$$

A quick comparison shows that the survival factor for the protons would be around 50%. The mass spectrum can be seen to left on Figure 60. A large rate of ρ -mesons are seen, which should be produced via $\gamma\mathbb{P} \rightarrow \rho$. This is not in this data. However, it does look like some of the features from the background template constructed from four pion events (See Figure 29) are present in the CMS results.

The ALICE[9] analysis does not report a cross section. Since they can measure a large rapidity range with good efficiency for low p_t tracks, they can require only two tracks and nothing else, and still remove most of the background. Still it cannot be seen if the proton dissociated. On Figure 60 the ALICE spectrum can be seen to the right. Because of the requirement of $p_t > 300\text{MeV}$, they cannot see the low mass region.

Comparison with LEP Data

Just for fun, we can compare with the non-exclusive $\pi\pi$ mass spectrum. Data from LEP taken with the ALEPH detector can be seen on Figure 61. The process is simply a e^+e^- collision, where the final state is an arbitrary number of pions. Afterwards the invariant mass of two pions are plotted. The kaon and the ρ are dominating, and the exotic mesons, which are seen in central exclusive pion production, are barely visible.

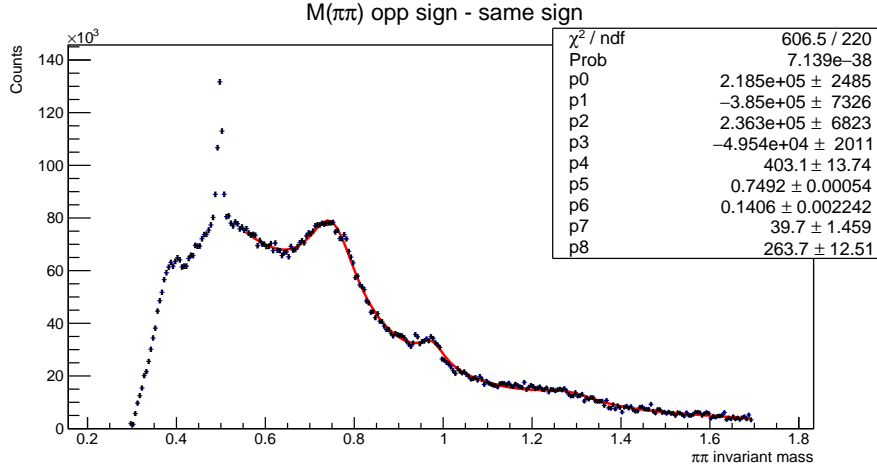


Figure 61: The LEP mass spectrum of pions produced in e^+e^- can be seen here. Courtesy of Peter Hansen.

Outlook

The main thing, which should be done, is a full ATLAS detector simulation to find the correct momentum resolution, tracking efficiencies and cross check the background subtraction method. Furthermore a method to distinguish between kaons and pions using $\frac{dE}{dx}$ in the Pixel Detector could be developed. This would enable a more precise measurement of the $\pi\pi$ cross section, while at the same time getting the cross section for central exclusive kaon production.

The six π cross section can also be determined using this data. A more detailed attempt at the partial wave analysis can be done, and using Monte Carlo for comparison would be quite helpful. The different resonances masses and widths could be extracted more precisely, using a more theoretically correct fitting approach.

A thorough measurement of α' and ϵ could possibly be performed. The second Pomeron flux parameter ϵ appears to change the branching ratios of the different pion productions. It seems that a high ϵ gives large $\pi\pi$ production and as you lower ϵ you get less $\pi\pi$ and more $\pi\pi\pi\pi$. It might be possible to fit ϵ if the different processes were compared.

The author also speculates if it is possible to calculate the acceptance by simply assuming that the t-spectrum can be modeled exponentially. Regarding the acceptance it would be quite nice to try different Monte Carlo generators other than PYTHIA, such as DimeMC and GenEx.

A track matching algorithm should be implemented to deal with multiple tracks in a single ALFA detector as discussed in the ghost track section. This would lower the systematic uncertainty on the measured cross section. However it does not seem to be crucial.

Finally two more runs were taken in the period of the 15th to 18th of October, which can be included. It would be particularly useful for measuring the cross section of central exclusive production of four pions, six pion and two kaons. These processes are limited by statistics. The two pion analysis would not gain much from increased statistics.

Conclusion

Central diffraction at high center of mass energies can be studied at the LHC. Double Pomeron Exchange is expected to dominate in this energy region, and it is therefore a good sector in which to study Pomeron physics. The analysis in this thesis is based on a series of low pile-up special optics runs with $\sqrt{s} = 13\text{TeV}$ and $\beta^* = 90\text{m}$, which were taken in October 2015.

The aim was to study the specific central diffractive process called central exclusive pion production. Here slightly scattered protons can be measured with the forward detector, ALFA, and centrally produced pions can be measured with the ATLAS Inner Detector. A technique to separate background and signal was developed, using the concepts of momentum and charge conservation. A series of detector efficiencies were determined using mainly data driven methods. The proton geometrical acceptance was calculated with PYTHIA8 using the Donnachie-Landshoff model with an $\alpha' = 0.126\text{GeV}^{-2}$. The result obtained for the cross section of the central exclusive dipion production $pp \rightarrow p + \pi^+ \pi^- + p$ was:

$$\sigma_{pp \rightarrow p + \pi^+ \pi^- + p} = 18.754 \pm 0.048(\text{stat.}) \pm 0.770(\text{syst.}) \mu\text{b}, \quad |\eta_\pi| < 2.5, \quad p_{t,\pi} > 100\text{MeV} \quad (62)$$

The mass spectrum are dominated by spin 0 and 2 meson states, of which many are glueball or tetraquark candidates. The mass spectrum has been fitted in an attempt to extract the different meson properties. A simple partial wave analysis has been performed.

An interesting dependence on the difference in the transverse momentum of the two outgoing protons was observed for the $pp \rightarrow p + \pi^+ \pi^- + p$ process. A similar effect has been seen before at the Omega spectrometer and the ISR, albeit less clearly than in the present study, where it was concluded that vertex factorization was broken in central exclusive dipion production, and it was speculated that it had something to do with the resonances.

It was also observed that the t-spectrum for a single proton looks different depending on the direction of the other protons transverse momentum. An attempt to extract the Pomeron flux parameter α' yields two different results depending on the difference in the transverse momentum of the outgoing protons.

The cross section for the central exclusive four pion production $pp \rightarrow p + \pi^+ \pi^- \pi^+ \pi^- + p$ has also been measured:

$$\sigma_{pp \rightarrow p + 4\pi + p} = 3.575 \pm 0.065(\text{stat.}) \pm 0.338(\text{syst.}) \mu\text{b}, \quad |\eta_\pi| < 2.5, \quad p_{t,\pi} > 100\text{MeV} \quad (63)$$

Here the mass spectrum shows two exotic meson states.

Bibliography

- [1] P.V.Landshoff A.Donnachie. Elastic scattering and diffraction dissociation. *Nuclear Physics B, Volume 244, Issue 2*, 1984.
- [2] Michael Albrow. Double pomeron exchange: from the isr to the lhc. *AIP Conf.Proc.1350:119-123,2011*, 2010.
- [3] V. V. Anisovich. Systematization of tensor mesons and the determination of the 2^{++} glueball. *JETPLett.80:715-720*, 2004.
- [4] <https://cds.cern.ch/record/1095924>.
- [5] <https://cds.cern.ch/record/1505342?ln=en>.
- [6] P. Aurenche. The standard model of particle physics. *ENSLAPP-A-659/97*, 1997.
- [7] <http://cds.cern.ch/record/1260465>.
- [8] <http://home.cern/about/accelerators>.
- [9] ALICE Collaboration. Central meson production in alice. *International Journal of Modern Physics A, Vol 29, 1446015*, 2014.
- [10] ATLAS Collaboration. Measurement of the total cross section from elastic scattering in pp collisions at $\sqrt{s} = 7$ tev with the atlas detector. *Nuclear Physics, Section B, pp. 486-548*, 2014.
- [11] CMS Collaboration. Exclusive and semi-exclusive pi+pi- production in proton-proton collisions at sqrt(s) = 7 tev. *CERN-EP-2016-261*, 2017.
- [12] The ATLAS Collaboration. Charged-particle distributions at low transverse momentum in $\sqrt{s} = 13$ tev pp interactions measured with the atlas detector at the lhc. *Eur. Phys. J. C 76 502*, 2016.
- [13] WA102 Collaboration. A partial wave analysis of the centrally produced k^+k^- and $k_s^0k_s^0$ systems in pp interactions at 450 gev/c and new information on the spin of the $f_0(1710)$. *Phys. Lett. B 453 305*, 1999.
- [14] WA102 Collaboration. A partial wave analysis of the centrally produced $\pi^+\pi^-$ system in pp interactions at 450 gev/c. *Phys. Lett. B 453 325-32*, 1999.
- [15] WA91 Collaboration. Observation of vertex factorisation breaking in central pp interactions. *Phys. Lett. B 388 853-858*, 1996.
- [16] John Ellis and Dmitri Kharzeev. The glueball filter in central production and broken scale invariance. *CERN-TH/98-349*, 1998.

- [17] A. Breakstone et al. The reaction pomeron-pomeron \rightarrow π^+ π^- and an unusual production mechanism for the $f_2(1270)$. *Zeit. Phys. C* 48, 569, 1990.
- [18] Barone et al. *High Energy Particle Diffraction*. Springer-Verlag, 2002.
- [19] Bruning et al. Lhc design report. *CERN Geneva*, 2004.
- [20] C. Amsler et al. Note on scalar mesons below 2 gev. <http://pdg.lbl.gov/2015/reviews/rpp2015-rev-scalar-mesons.pdf>, 2015.
- [21] D. Asner et al. Resonances. <http://pdg.lbl.gov/2013/reviews/rpp2013-rev-resonances.pdf>, 2013.
- [22] Deandrea et al. The s anti-s and k anti-k nature of $f_0(980)$ d(s) decays. *Phys. Lett. B* 502, 79, 2001.
- [23] Donnachie et al. *Pomeron Physics and QCD*. Cambridge monographs on particle physics, nuclear physics, and cosmology; v. 19, 2002.
- [24] G. Aad et al. The atlas experiment at the cern large hadron collider. *CERN Geneva*, 2010.
- [25] K.A. Olive et al. (particle data group). *Chin. Phys. C*, 38, 090001, 2015.
- [26] Lebedowicz et al. Central exclusive diffractive production of $\pi^+\pi^-$ continuum, scalar and tensor resonances in pp and $p\bar{p}$ scattering within tensor pomeron approach. *Phys. Rev. D* 93, 054015, 2016.
- [27] <https://twiki.cern.ch/twiki/bin/view/Atlas/MbtsTrigger>.
- [28] Benno List for the H1 Collaboration. Extraction of the pomeron trajectory from a global fit to exclusive ρ^0 meson photoproduction data. *Progress in High Energy Physics, Vol. 3*, 2009.
- [29] C. Gabaldon. Performance of the atlas trigger system. *JINST* 7 C01092, 2012.
- [30] Peter Hansen. Particle detectors and accelerators. Lecture notes.
- [31] https://atlas-rtt.cern.ch/prod/rtt/rel_1/cmake/build/x86_64-slc6-gcc49-opt/offline/TrigAnalysisTest/RD0toAOD_MC_pp_v6_bphysics_1000/RD0toAOD_MC_pp_v6_bphysics_1000_log.tail.txt.
- [32] <https://cds.cern.ch/record/1095926?ln=en>.
- [33] Sune Jakobsen. *Commissioning of the Absolute Luminosity For ATLAS detector at the LHC*. PhD dissertation, University of Copenhagen, Niels Bohr Institute, 2013.
- [34] Krzysztof Janas. Analysis of the track reconstruction algorithm in the alfa detector of the atlas experiment. Technical report, Technical report, 2014.
- [35] Eugene Levin. Everything about reggeons.part i:reggeons in "soft" interaction. *TAUP 2465 -97, DESY 97-213*, 1997.
- [36] <https://indico.cern.ch/event/618941/>.
- [37] Alexander Lind. A study of diffractive scattering with the atlas and alfa experiment. Master's project, University of Copenhagen, Niels Bohr Institute, 2017.

- [38] Morten Medici. Diffraction with alfa and atlas at $\sqrt{s} = 8$ tev. Master's project, University of Copenhagen, Niels Bohr Institute, 2013.
- [39] Sparsh Navin. Diffraction in pythia. *arXiv:1005.3894*, 2010.
- [40] Wolfgang Ochs. The status of glueballs. *J. Phys. G* 40 043001, 2013.
- [41] J.R. Pelaez. From controversy to precision on the sigma meson: a review on the status of the non-ordinary $f_0(500)$ resonance. *Physics Reports* 658 1, 2016.
- [42] V.A. Petrov. Nonlinear regge trajectories in theory and practice. *AIP Conf.Proc.1105:266-269*, 2009.
- [43] K. Goulianos R. Ciesielski. Mbr monte carlo simulation in pythia8. [*arXiv:1205.1446*], 2012.
- [44] http://www.clab.edc.uoc.gr/materials/pc/img/running_coupling1.gif.
- [45] Simon Stark. *Study of forward elastic pp scattering at $\sqrt{s} = 8$ TeV with the ALFA detector*. PhD dissertation, University of Copenhagen, Niels Bohr Institute, 2017.
- [46] S. Mrenna T. Sjostrand and P. Skands. Pythia 8.1. *JHEP05 (2006) 026, Comput. Phys. Comm. 178 (2008) 852*.
- [47] Wei-Min Wang, Zhi-Gang; Yang. Analysis the $f_0(980)$ and $a_0(980)$ mesons as four-quark states with the qcd sum rules. *The European Physical Journal C, Volume 42, Issue 1, pp.89-92*, 2005.

List of Figures

1	The seventeen elementary particles, which have been experimentally observed. It is expected that we have an eighteenth particle named the graviton which is the propagator of the gravitational force.	11
2	The strength of the coupling constant changes for the different forces as we change the energy.[44]	12
3	Here the mass squared of the mesons are plotted against their angular momentum, i.e. the real part of $\alpha(t)$. The mass squared is equivalent to the s-channel, and we can then extend the trajectory into the t-channel. [42] . . .	15
4	[37] The figure shows the elastic and the different diffractive topologies in rapidity space and ϕ space. The cross sections are $\sigma_{el} > \sigma_{sd} > \sigma_{dd} > \sigma_{cd}$. . .	16
5	Central exclusive production of two pions [26]. One is produced via continuum, another via a meson resonance. The possible exchange objects are Pomerons, Reggeons and Photons. Pomerons dominate at high \sqrt{s}	17
6	The CERN accelerator complex. Picture from [7]	22
7	Cross section of the ATLAS detector[5], and the different detector signatures of different particles. Here a pion would look the most like the proton and electron tracks, however pions produced in central diffraction will not reach outside the Inner Detector, because the track curls too much due to the low p_t .	25
8	The ATLAS detector. [4]	25
9	The ATLAS Inner Detector. [32]	25
10	The ALFA detector setup in relation to the ATLAS interaction point.	29
11	Proton hits in one of the ALFA stations is shown here. The shape of the detector is outlined by proton hits taken from data. The detectors are around 6mm away from the beam, but they can be moved closer.	30
12	Track reconstruction in the ALFA detector. A track is reconstructed independently in the U-layer and V-layer by checking overlapping fibers. The proton is concluded to be in the area where all the fibers overlap.[10]	30
13	A diagram of a two proton event, which generates ghost tracks with completely different coordinates. The first proton hit is indicated as the red dot. It generates fiber activity in a specific V-layer fiber and U-layer fiber, marked with the red star. The second proton is the blue dot, which activates two fibers as well. Since four fibers are showing signal, two ghost tracks marked as yellow dots are constructed from the combinatorics.	31
14	A picture of an ALFA Roman Pot.	32
15	The experimental signature of a signal event with the ALFA trigger ELAST15. The black line represent the incoming protons, the red lines represent the two outgoing protons, and finally the red cones represent the central system. Figure from [38]	34

16	A cutflow of run 282455. The cut on the primary vertex barely does anything. Since the tracking criteria includes cuts on both $ d_0 $ and $ z_0 \times \sin(\theta) $, then almost all tracks that pass these criteria will have a vertex.	35
17	A first degree polynomial is fitted to each detector. The detector is then rotated until the slope is zero.	36
18	The x-coordinate of the proton hits are recorded. Since elastic events are symmetrical in the azimuthal angle, the elastic events will be Gaussian distributed around the beam center in x. The detectors are then aligned so the beam is centered in $x = 0$	37
19	The relative y-alignment is made by finding the intercept of the plot of the inner detector y-coordinate as a function of the difference between the inner and outer detector y-coordinate.	38
20	The reconstructed proton kinematics. The gap in the center of the p_y distribution is due to the detector acceptance. The y-momentum is not symmetric around zero due to the crossing angle. The tail in the p_x distribution are from particles with energy loss.	39
21	The total x-momentum of the four different arms.	40
22	The total y-momentum of the four different arms.	41
23	The background template is scaled using a χ^2 fit of the template in both the p_x and p_y projection simultaneously.	43
24	The signal region is depicted with the red ellipsis. The events outside the red ellipsis are used to scale the background templates.	43
25	The background as represented in terms of standard deviations from $(p_x, p_y) = (0,0)$	44
26	The cross section calculated with different choices of signal region. For the value $n = 30$, a signal region of $n = \sqrt{\frac{p_x^2}{\sigma_x^2} + \frac{p_y^2}{\sigma_y^2}} < 30$ has been chosen.	48
27	The dipion mass spectrum with and without a momentum cut. As can be seen the ρ - and K/\bar{K} -resonance is largely removed.	49
28	The mass spectrum of events with missing momentum. The overall background template has been scaled to match the amount of background events extrapolated using the same sign background template.	50
29	The mass spectrum from two pions in a four pion event. The overall background template has been scaled to match the amount of background events extrapolated using the same sign background template.	51
30	The local angle in x plotted versus the inner detector coordinate in x. On the left hand side there is background, and the right hand side is predominantly signal. An ellipsis is fitted to signal, and a 3σ contour is drawn in.	52
31	Here the angular distribution of the pions are shown for different invariant masses.	53
32	The S-wave density matrix element as a function of the invariant mass.	53
33	The SD density matrix element as a function of the invariant mass.	54
34	The DD density matrix element as a function of the invariant mass.	54
35	Similar to Figure 26 but now with four pions. A maximum is seen at a signal region of $n = 14$	56
36	The mass spectrum of events with missing momentum. The overall background template has been scaled to match the amount of background events extrapolated using the same sign background template.	56

37	The proton acceptance for $pp \rightarrow p + \pi\pi + p$ events with pions in the fiducial volume $ \eta_\pi < 2.5$, $p_{t,\pi} > 100\text{MeV}$. This is applied bin to bin to the two pion mass spectrum.	60
38	The acceptance of the entire particle system $pp \rightarrow p + \pi\pi + p$ as a function of invariant mass of the central dipion system. The low invariant mass acceptance drops sharply for the events with protons on opposite side of y.	61
39	The proton acceptance for $pp \rightarrow p + 4\pi + p$ as a function of invariant mass of the central four pion system. This is seen to be more or less flat.	61
40	The proton acceptance for $pp \rightarrow p + \pi\pi + p$ events with pions in the fiducial volume $ \eta_\pi < 2.5$, $p_{t,\pi} > 100\text{MeV}$, and the second proton hitting an ALFA station. There is a slightly different acceptance in the same pots depending on, what detector the other proton hit. This is an effect of the pion fiducial volume.	62
41	The ALFA track reconstruction efficiency as a function of lumiblock in run 282026. The efficiency is stable during time indicating a stable beam.	67
42	The maximum amount of tracks in any single pot during an event is shown. For example if one pot has two tracks, and the others have one, then it is counted as "2", since this is the maximum amount of tracks in any of the pots.	69
43	The Inner Detector track reconstruction efficiency for single tracks as a function of η and p_t . These results are from an ATLAS MinBias paper [12]. The efficiency was applied on an event by event basis based on η and p_t of the measured pions.	70
44	The uncertainty on the two pion cross section from the uncertainties of the Inner Detector efficiencies, extracted with a bootstrapping method.	71
45	The uncertainty on the four pion cross section from the uncertainties of the Inner Detector efficiencies, extracted with a bootstrapping method.	72
46	The mass spectrum of the two pion system with only events that have no reconstructed vertex. As can be seen there is a large peak at the neutral kaon mass and at the pion threshold.	73
47	The differential cross section as a function of the dipion invariant mass. The total fit is shown in the red color. Bare Breit-Wigners with no interference effects has been drawn separately for the different resonances to illustrate their widths and masses.	77
48	For $ \eta_\pi < 2.5$, $p_{t,\pi} > 100\text{MeV}$. The differential cross section as a function of the two pion invariant mass. Here it is separated into two categories depending on the difference in outgoing transverse momentum of the protons. From an experimental setup the red spectrum corresponds to trigger items ELAST15 and ELAST18, whereas the blue spectrum correspond to SYST17 and SYST18.	78
49	For comparison the mass spectrum of the pions has been corrected to the full phase space. No major difference in the spectrum shape is seen.	79
50	For $ \eta_\pi < 2.5$, $p_{t,\pi} > 100\text{MeV}$. Differential cross section of $-t$ in terms of the A side proton and B side proton in central exclusive $\pi\pi$ production. We have a minimum of $-t = 0.03\text{GeV}^2$. For each of the respective distributions, an integration over the other protons t has been performed.	79
51	For $ \eta_\pi < 2.5$, $p_{t,\pi} > 100\text{MeV}$. Differential cross section of $-t$ for each of the respective protons in central exclusive $\pi\pi$ production. There is a clear difference in the proton t depending on the other protons outgoing momentum. This does not appear to be an acceptance effect, since it is not seen in MC.	80

52	For $ \eta_\pi < 2.5$, $p_{t,\pi} > 100\text{MeV}$. Differential cross section of $-t$ in terms of the A side proton and B side proton in central exclusive $\pi\pi$ production. We have a minimum of $-t = 0.03\text{GeV}^2$. When fitting an exponential, it appears the slope change for same side protons around 0.45GeV^2 . Beyond that the two distributions have the same t slope.	80
53	For $ \eta_\pi < 2.5$, $p_{t,\pi} > 100\text{MeV}$. Differential cross section of total energy of the two pion system. An exponential has been fitted to the region, where the pion fiducial volume has minimal effect.	81
54	The χ^2 when comparing the t -spectrum of MC with data as a function of the MC parameter α' . The upper diagram shows the extracted α' for events with protons on the same side of the transverse plane, and below are events with protons on the opposite side of the transverse plane.	82
55	The differential $pp \rightarrow p + 4\pi + p$ cross section as a function of invariant mass.	83
56	A Dalitz plot including combinatorial background of the four pion process. The sharp peak at around (500MeV,500MeV) shows the $K\bar{K}$ -channel and the wider peak at (770MeV,770MeV) shows the $\rho\rho$ -channel	84
57	The ISR mass spectrum.[17]	86
58	The ISR density matrices.[17]	86
59	The WA91 mass spectrum dependence on transverse outgoing momentum. Here figure A and C corresponds to same side outgoing protons, whereas B and D refers to opposite side outgoing protons. [15]	87
60	The CMS[11] dipion mass spectrum can be seen on the left. The ALICE[9] mass spectrum can be seen on the right.	88
61	The LEP mass spectrum of pions produced in e^+e^- can be seen here. Courtesy of Peter Hansen.	89
62	Comparison between Data and Monte Carlo, which has been produced using the ALFA detector simulation. The MBR model is shown above, and the Donnachie-Landshoff model is shown below. Data before acceptance correction have been plotted as well.	102
63	The predicted Monte Carlo mass spectrums are plotted here. They have been produced using the ALFA detector simulation. The MBR model is shown above, and the Donnachie-Landshof model is shown below.	103
64	The data mass spectrum without any acceptance corrections.	103

List of Tables

1	The current world average for the scalar meson parameters. Taken from the Particle Data Group[25].	18
2	Cut flow for two pion events with the same sign charge (SS) and opposite sign charge (OS).	35
3	Cut flow for four pion events with non zero total charge (SS) and zero total charge (OS).	35
4	The momentum resolution of the full $p + \pi\pi + p$ -system.	40
5	The scaling factors for the background template, when fitting the template to the data with missing momentum beyond 5σ	45
6	Scaling factors for the background template, when fitting the template to the data with missing momentum beyond 7.5σ	45
7	Scaling factors for the background template, when fitting the template to data with missing momentum beyond 10σ	45
8	Scaling factors for the background template, when fitting the background template and a Gaussian distribution simultaneously to the full data sample in momentum space.	45
9	Scaling factors for the background template, when normalizing the template to data with missing momentum beyond 5σ	46
10	Scaling factors for the background template, when normalizing the template to data with missing momentum beyond 7.5σ	46
11	Scaling factors for the background template, when normalizing the template to data with missing momentum beyond 10σ	46
12	The cross section using different background subtraction schemes. The method for calculating the cross section is found in a later section.	47
13	The background to signal ratio in different regions of momentum space.	47
14	The background scaling factors determined using Scaling Method 2 for events with four pions.	55
15	The vertex spread calculated from the beam emittance.	58
16	The momentum spread in x and y for the two beams	58
17	The acceptance of the protons in central exclusive $\pi\pi$ events, where both pions are in the fiducial volume defined by $ \eta_\pi < 2.5$ and $p_{t,\pi} > 100\text{MeV}$. The model used is Donnachie-Landshof with $\alpha' = 0.126\text{GeV}^{-2}$	59
18	The acceptance of the protons in central exclusive $\pi\pi$ events, where both pions are in the fiducial volume defined by $ \eta_\pi < 2.5$ and $p_{t,\pi} > 100\text{MeV}$. The model used is MBR with $\alpha' = 0.126\text{GeV}^{-2}$	59
19	The acceptance of the protons in central exclusive $\pi\pi\pi\pi$ events, where all pions are in the fiducial volume defined by $ \eta_\pi < 2.5$ and $p_{t,\pi} > 100\text{MeV}$. The model used is Donnachie-Landshof with $\alpha' = 0.126\text{GeV}^{-2}$	59
20	The trigger efficiency of the ALFA L1 trigger configurations. The trigger efficiency for L1_SYST17 and L1_SYST18 are taken to be the same.	62

21	The high level trigger efficiency of HLT_mb_sptrk_vetombts2in_L1ALFA_CEP found using different methods.	63
22	Signal events are thrown away due to the L1 trigger veto. The chance that a signal event of a given arm survives the veto is shown here. Because the arms have different rates of beam halo activity, they also have different efficiencies.	65
23	There is a loss of signal due to inelastic collisions, which happens simultaneously with signal events. $\epsilon_{\text{pile-up}}$ is the fraction of signal events, where there are additional collisions.	65
24	The ALFA track reconstruction efficiency for protons.	67
25	The fraction of signal events that survive the cut on events with four ALFA tracks in one pot.	69
26	The background scaling factors determined using Scaling Method 2, when no vertex requirement is imposed.	73
27	The systematic uncertainties to the $\pi\pi$ cross section	75
28	$\sigma_{pp \rightarrow p+\pi\pi+p}^{\text{fid1}}$, when using an acceptance determined with different models. . .	76
29	$\sigma_{pp \rightarrow p+\pi\pi+p}^{\text{fid2}}$, when using an acceptance determined with different models. . .	76
30	The meson parameters extracted from the fit of the mass spectrum.	77
31	The systematic uncertainties to the $\pi\pi\pi\pi$ cross section	83
32	The ALFA alignment values for Run 282455	100
33	The ALFA alignment values for Run 282026	100
34	The ALFA alignment values for Run 282420	101

Appendix

Alignment

The total coordinate transformation for upper detectors is of the form:

$$x_{\text{upper}} = \delta x + \cos(\theta)x_{\text{raw}} - \sin(\theta)y_{\text{raw}} \quad (64)$$

$$y_{\text{upper}} = \delta y + \cos(\theta)y_{\text{raw}} + \sin(\theta)x_{\text{raw}} \quad (65)$$

and for lower detectors:

$$x_{\text{lower}} = \delta x + \cos(\theta)x_{\text{raw}} + \sin(\theta)y_{\text{raw}} \quad (66)$$

$$y_{\text{lower}} = \delta y - \cos(\theta)y_{\text{raw}} + \sin(\theta)x_{\text{raw}} \quad (67)$$

These values include a coordinate transformation from the ALFA coordinate system to beam coordinate system.

Run 282455	δx [mm]	δy [mm]	$\cos(\theta)$	$\sin(\theta)$
Pot 1	-1.284842165	141.1334166	0.9999864233	0.00521087833
Pot 2	0.02918135656	-141.3635596	0.999999388	-0.001106381337
Pot 3	-1.177610209	141.815385	0.9999934208	0.003627436007
Pot 4	-0.6653518369	-141.8980099	0.9999988381	-0.001524422245
Pot 5	0.1409970848	141.5125663	0.9999976989	-0.002145263202
Pot 6	-0.5172005921	-142.0214935	0.9999968379	-0.002514807971
Pot 7	0.5620722837	140.8679851	0.9999838505	-0.005683193075
Pot 8	0.03422498503	-141.458095	0.9999967583	0.002546233049

Table 32: The ALFA alignment values for Run 282455

Run 282026	δx [mm]	δy [mm]	$\cos(\theta)$	$\sin(\theta)$
Pot 1	-1.437247049	141.1453471	0.9999842816	0.005606829659
Pot 2	-0.3974345233	-141.371488	0.9999913935	-0.004148845557
Pot 3	-1.932844876	141.8163191	0.9999572698	0.009244377931
Pot 4	-0.4670088408	-141.8990837	0.9999999843	0.000177018877
Pot 5	-0.9909982471	141.5086893	0.9999812622	0.006121705821
Pot 6	-0.8020019283	-142.0001896	0.9999908245	-0.004283792794
Pot 7	-1.028390208	140.8566715	0.9999812507	0.006123574262
Pot 8	-1.339727191	-141.4768544	0.9999717712	-0.007513774903

Table 33: The ALFA alignment values for Run 282026

Run 282420	$\delta x[\text{mm}]$	$\delta y[\text{mm}]$	$\cos(\theta)$	$\sin(\theta)$
Pot 1	-2.239478776	141.1294283	0.9999248851	0.01225659836
Pot 2	-0.4779564395	-141.3687413	0.9999890206	-0.004686000912
Pot 3	-1.283302551	141.814708	0.999991433	0.004139305555
Pot 4	-0.6611954656	-141.8982792	0.9999992452	-0.001228642201
Pot 5	-0.7875406166	141.5101227	0.9999888012	0.00473259424
Pot 6	-0.3380831811	-142.0222393	0.9999995697	-0.0009276468211
Pot 7	-2.063694949	140.8531437	0.9999005907	0.01409995655
Pot 8	-0.7414967631	-141.4390002	0.9999948857	-0.00319820465

Table 34: The ALFA alignment values for Run 282420

Comparison of the Mass Spectrum between Data and Monte Carlo

The dipion mass spectrums in both the PYTHIA8 MBR and Donnachie-Landshoff model do not look like data. However the developers do not claim that they look like data, since there are no incorporated resonances, so there is not really anything interesting to be concluded from this comparison. As can be seen from the Figure 62, it appears that the Donnachie-Landshoff model fits this data better. Both models here use $\alpha' = 0.126$ and $\epsilon = 0.085$. The MC cross sections have been scaled to match data.

The Mass Spectrum dependence on dP_t in Monte Carlo

The PYTHIA8 Donnachie Landshoff and MBR mass spectrum has been produced using the detector simulation. They can be seen on Figure 63. The predicted rates for the different arms are different to data. For comparison the non-acceptance corrected mass spectrum can be seen on Figure 64.

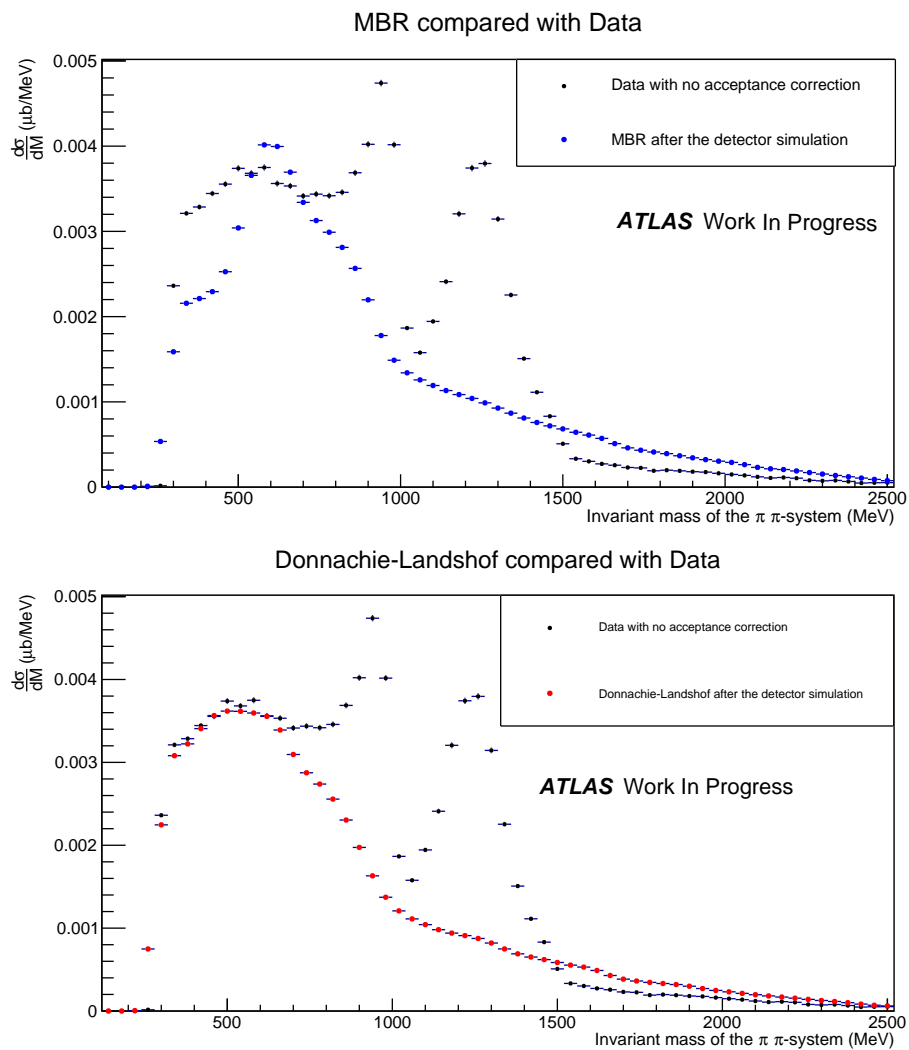


Figure 62: Comparison between Data and Monte Carlo, which has been produced using the ALFA detector simulation. The MBR model is shown above, and the Donnachie-Landshof model is shown below. Data before acceptance correction have been plotted as well.

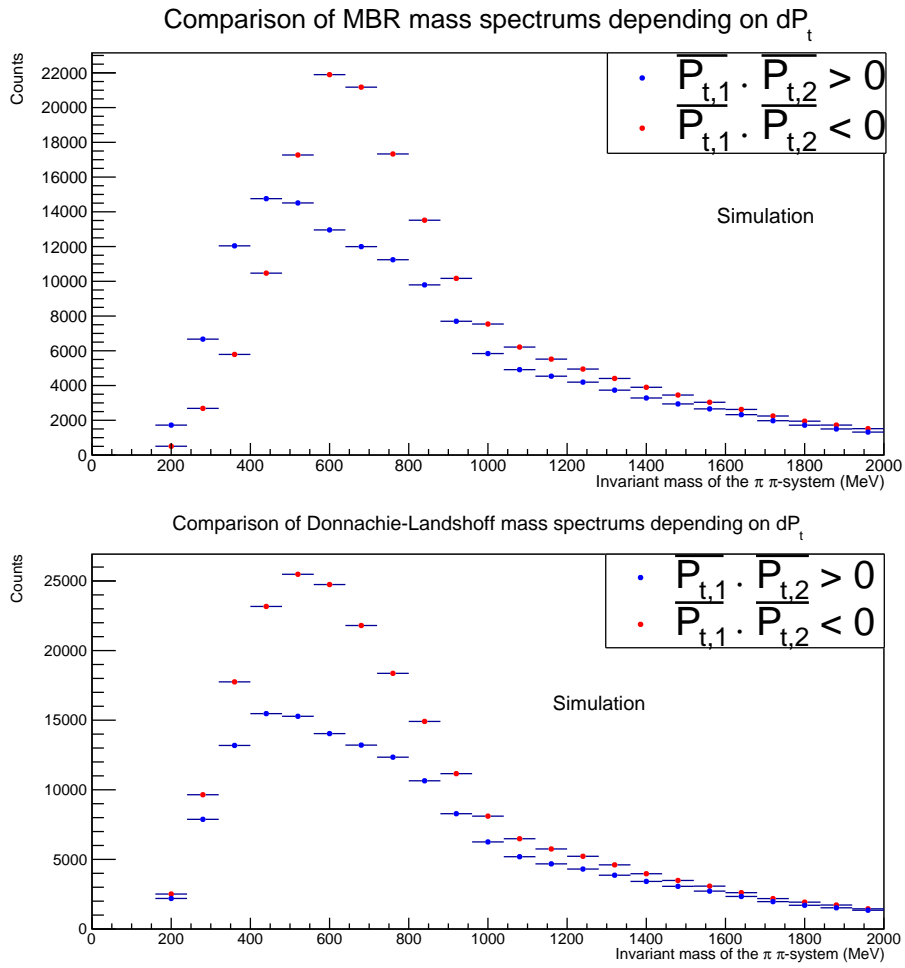


Figure 63: The predicted Monte Carlo mass spectrums are plotted here. They have been produced using the ALFA detector simulation. The MBR model is shown above, and the Donnachie-Landshof model is shown below.

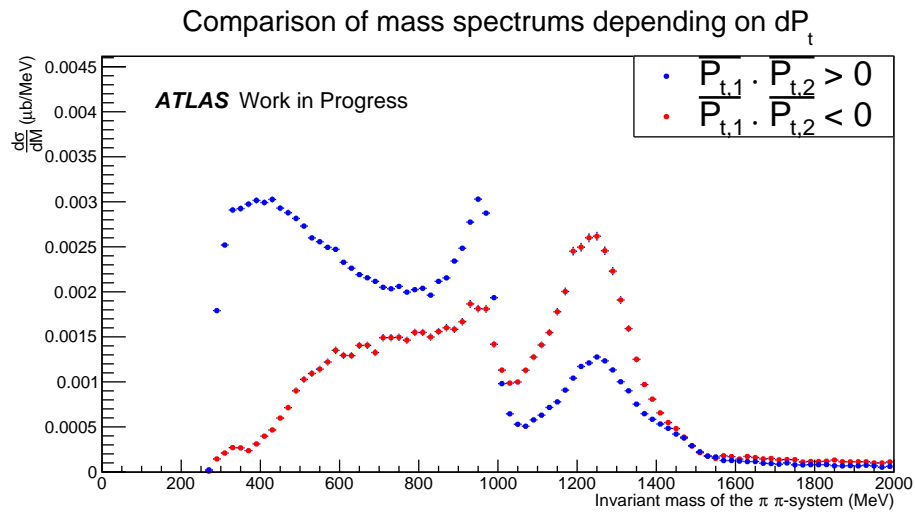


Figure 64: The data mass spectrum without any acceptance corrections.